Design and Fabrication of Nanomaterials for Efficient Solar to Chemical Energy Conversion

Submitted by Govinder Singh Pawar to the University of Exeter
as a thesis for the degree of
Doctor of Philosophy in Renewable Energy
In March 2019

This thesis is available for Library use on the understanding that it is copyright material and that no quotation from the thesis may be published without proper acknowledgement.

I certify that all material in this thesis which is not my own work has been identified and that no material has previously been submitted and approved for the award of a degree by this or any other University.

Abstract

Solar energy is a large, exploitable, renewable resource where it can supply the earth with enough energy in one hour, equivalent to the mankind’s total energy consumption in a year. Nanomaterials, for semiconductor material, used as a photocatalyst to convert sunlight into chemical fuel (hydrogen) via photoelectrochemical water splitting process, has been considered as the Holy Grail to a carbon free hydrogen economy. Conversion of sunlight into hydrogen is a promising, clean and sustainable way of generating hydrogen.

In this research project we have designed, synthesised, characterised and tested new materials for which can generate hydrogen from water using solar energy. Due to the lack of suitable p-type semiconductor materials, this work has focused on synthesising and developing new, stable, visible light active photocathodes for solar hydrogen generation.

In pursuit of this stable photocathode, we have synthesised stable visible light active $LaFeO_3$ which has shown some promise as a future candidate p-type photocathode. This was produced by cheap, novel and scalable spray pyrolysis technique which has resulted in current densities of 0.16 mA cm^{-2} at 0.26 V vs RHE and shown stability over 21 hours. Subsequently, this led to hydrogen generation of 0.18 μmol cm^{-2}. Furthermore, $LaFeO_3$-Ag and $LaFeO_3$-Ni were fabricated by spin coating silver and nickel nanoparticles on to the spray pyrolysed $LaFeO_3$, to enhance photocurrent density for enhance hydrogen generation via solar water splitting. This led to over double the amount of hydrogen being produced. Similarly, $TaFeO_4$ was fabricated by sol-gel method which yielded 0.091 μmol g^{-1} of hydrogen. Future work is required

on $TaFeO_4$ to fabricate electrode form of the material so its band structure many be determined. This may be done by microwave assisted annealing.

Acknowledgement

Firstly, I would like to thank my supervisor Dr Asif Tahir for providing support and guidance throughout my PhD and his continued patience and knowledge.

Secondly, I would like to thank my solar group colleague for suggestions and discussions to do with my work.

I am very grateful to EPSRC (EP/R512801) for providing funding to support me financially during the course of my PhD.

I would also like to thank my family for providing motivational support and encouragement to complete my PhD.

Last but not least, I would like to thank all my closest friends which I have made in Cornwall, who have been with me through the good and bad times. Without them my PhD experience would not have been the same.

Table of Contents

1.3 Renewable Energy

Chapter 5: Experimental Procedure………………………………………109

Appendix

List of Figures

List of Abbreviations

AACVD – aerosol assisted chemical vapour deposition

AP – artificial photosynthesis

ALD – atomic layer deposition

CA – chronoamperometry

EDX – energy dispersive x-ray spectroscopy

EIS – electrochemical impedance spectroscopy

FDTD – finite difference time domain

FTO – fluorine doped tin oxide

GC – gas chromatography

IPCE – incident photon to current conversion efficiency

LSV – linear sweep voltammetry

MOFs – metal organic frameworks

NHE – normal hydrogen electrode

NP – natural photosynthesis

PEC – photoelectrochemical

PLD – pulse laser deposition

SEM – scanning electron microscope

SP – spray pyrolysis

SPR – surface plasmon resonance

STH – solar to hydrogen

UV-Vis – ultraviolet – visible light spectroscopy

XRD – x-ray diffraction

Chapter 1: Introduction

The motivation for this PhD research project is outlined in this chapter. The focus of this project is to harvest solar energy by splitting water by the photoelectrochemical (PEC) process to generate hydrogen. Hydrogen is a desired product because it can be used as a chemical feedstock for many processes. Furthermore, hydrogen has more than double the energy density of fossil fuels meaning we could get more energy out of the same volume hydrogen compared to fossil fuel. Solar generated hydrogen is considered as the “Holy Grail” as the future energy carrier but due to the lack of suitable materials its production is hindered.

The fundamental challenges for large scale solar water splitting for hydrogen production are: (i) instability of materials, (ii) lack of efficient visible light active material and (iii) lack of photocathodes. Majority of materials suffer from stability issues where after a short amount of time (typically few minutes) the photoelectrode films begin to visibly degrade in the electrolyte solution. A minimum of 10% STH efficiency is required for practical applications of solar water splitting technology. However, there is a lack of suitable materials which can achieve this. Not many photocathode materials have been investigated compared to photoanodes for water splitting applications. Therefore, there is a gap in which material investigation can be done to find a suitable p-type material.

1.1 Aims/ Objectives

The aim of the research project is to first design and develop a stable p-type semiconductor photocathode material for photoelectrochemical hydrogen generation. Second, to improve the photocathodes efficiency for enhanced hydrogen yield from PEC water splitting. To achieve these aims the PhD is divided into the following objectives;

1. Literature survey.
2. Development of synthesis method for control of morphology and nano-architecture.
3. Characterisation of the material to determine is phase, crystallinity, morphology and surface structure.
4. UV-Vis analysis for optical characterisation.
5. PEC performance analysis.
6. Electrochemical characterisation.
7. Hydrogen evolution performance testing.

P-type $LaFeO_3$ has been synthesised and its performance for the application of solar driven generation of hydrogen gas is investigated. $LaFeO_3$ is synthesised by sol-gel and spray pyrolysis to optimise the ideal fabrication condition of thin film $LaFeO_3$. Their photoactivity, stability, optical and electrical properties are studied and characterised using techniques such as XRD, SEM/ EDX and Raman spectroscopy.

$LaFeO_3$-Ag and $LaFeO_3$-Ni have also been synthesised by spray pyrolysis and spin coating to improve the performance of $LaFeO_3$. Furthermore, they are also studied in the same way as $LaFeO_3$.

$TaFeO_4$ photocatalytic powder is synthesised by sol-gel. It is characterised and tested to see if it is capable of performing solar water splitting for hydrogen evolution. Attempts were made to fabricate $TaFeO_4$ in an electrode form onto quartz FTO and conducting flexible carbon fibre material.

1.2 Traditional Sources of Energy

Currently we are meeting the majority of our energy demands (85%)[1] by using fossil fuels (coal, oil and natural gas) which has led to rapid global development. This rapid development has led to populations increasing subsequently leading to an increase in energy demand. It is estimated that by 2050 the global energy consumption is expected to double.[2] However, fossil fuel resources are finite and concentrated in certain areas around the world, thus securing a steady supply of fossil fuel energy is increasingly becoming a challenge. Furthermore, there are environmental and human health concerns related to greenhouse gas emissions from fossil fuel burning. Increase in greenhouse gas emissions has caused climate disasters globally where the melting of polar ice caps has led to rise in sea levels, climate changes where more places are facing extreme flooding, freezing condition and extreme heatwaves. Therefore, an alternative energy production is required to reduce greenhouse gas emissions.

1.3 Renewable Energy

Renewable energy such as wind, hydroelectric, geothermal, biomass and solar have been well investigated over the past few decades and have been implemented into the real world to begin the replacement of fossil fuels. Constant technological development of these renewable resources means that they are becoming more commercially viable and beginning to compete with fossil fuels.

Of these renewable energy resources, solar energy is considered as a primary carrier for a clean and sustainable energy. Solar energy may be directly converted into a chemical fuel which can be stored, transported and used when required. Solar driven water splitting is an application which can do just that; solar energy splits water into its constituent’s hydrogen and oxygen, where hydrogen is called solar fuel. The appeal of solar water splitting is that it requires a small potential (1.23 V), no CO_2 emissions and the abundance of natural resources (i.e. water and sunlight). However this application is limited due to lack of suitable material. A thorough understanding of the water splitting mechanism, techniques and materials used can help guide us to developing new materials and devices for efficient solar water splitting.

Thus, a comprehensive literature survey is conducted to understand how the mechanism of water splitting works, the materials and techniques used to make efficient semiconductor materials and to determine what materials are currently out there and to identify the gap in materials used for photocathodes.

Reference

(1) Barber, J. Photosynthetic Energy Conversion: Natural and Artificial. *Chem. Soc. Rev.* **2009**, *38* (1), 185–196.

(2) van de Krol, R.; Grätzel, M. *Photoelectrochemical Hydrogen Production*; Spriger Science & Business Media: New York, USA, 2011.

Chapter 2: Literature Review

The current global energy consumption is approximately 14 - 15 TW and is expected to double by 2050. At the present time about 85% of energy provided comes from the burning of fossil fuels.[1,2] The sun is by far the largest renewable source which provides the earth with 100,000 TW of energy annually. Therefore, the energy provided from one hour of sun light illumination is equivalent to mankind's total energy consumption for one year.[1] However due to the sporadic nature of solar energy, efficient storage devices need to be developed and employed in order to make solar energy a feasible energy source. Transportable and storable solar fuels (hydrogen) from renewable resources and efficient energy storage can only provide a sustainable pathway for true transformation to renewable energy to address the global challenge related to energy and environment.

There are a number of renewable energy resources such as wind, hydroelectric, biomass, tidal, solar energy and geothermal which have been investigated and in use to start replacing fossil fuels as an energy source. Extensive research and technological development is required to be commercially available globally and to completely replace fossil fuels in a cost effective manner with the current infrastructure.

Another renewable energy carrier which has excellent potential for replacing fossil fuels is hydrogen gas (H_2). Hydrogen has an energy density of 140 MJ kg^{-1}, far exceeding that of fossil fuels, with zero carbon emission and the only by-product from combustion is water.[3] However, hydrogen production from industrial processes consumes huge amount of fossil fuels resulting in equally large CO_2 production.[4] Furthermore, almost all hydrogen production is based on and generated from raw fossil materials and only 4% of hydrogen is produced by water electrolysis.[5,6] Therefore, hydrogen production from a renewable energy source, instead of fossil fuels (e.g. solar water splitting), has attracted a huge international interest for clean hydrogen gas generation. By developing semiconductor materials as a photocatalyst, it is possible to split water into in constituents (O_2 and H_2) via solar irradiation where the hydrogen gas is collected, stored and transported to be used at a later time. In this process no greenhouse gases are generated. However, sufficient suitable materials are needed to achieve the solar energy to hydrogen conversion efficiently.

2.1 Principle of Solar Water Splitting

The solar to chemical energy conversion exists naturally in plants as natural photosynthesis (NP), where oxygen and carbohydrates are produced from water and carbon dioxide using sun light. However, less than 1% efficiency is achieved.[1,7] Using this principle, artificial photosynthesis (AP) using man made materials can be employed to generate hydrogen from solar water splitting. Splitting water into its constituents (H_2 and O_2) in the presence of a semiconductor material, or photocatalyst, and sun light is a promising approach for converting and storing solar energy as a chemical energy and has been discussed thoroughly in literature.[8–13] The dissociation reaction (equation 1) is an uphill reaction with a positive change in the Gibbs free energy ($\Delta G^o = 237.13$ kJ mol^{-1}).

$$2H_2O \rightarrow 2H_2 + O_2 \qquad \textbf{(eq. 1)}$$

The half-cell reactions of oxygen and hydrogen gas generation from water are shown in the equations below:

$$\text{Oxidation: } H_2O + 2h^+ \rightarrow \tfrac{1}{2} O_2 + 2H^+ \qquad \textbf{(eq. 2)}$$

$$\text{Reduction: } 2H^+ + 2e^- \rightarrow H_2 \qquad \textbf{(eq. 3)}$$

Oxidation potential of O_2/ H_2O is 1.23 V vs. standard hydrogen electrode (SHE) and reduction potential of H^+/ H_2 is 0 V vs. SHE. Thermodynamically speaking water splitting is not a spontaneous process due to the largely positive Gibbs free energy under ambient conditions. Theoretically, a potential of 1.23 eV is required for the generation of hydrogen and oxygen by water splitting. However, taking into account energy losses caused by recombination of the photo-generated charges, resistance from electrical connections, resistance of electrodes and voltage loses at the contact points, a voltage of 1.8 eV is required for spontaneous water splitting.[14] Research in this field was first demonstrated by Fujishima and Honda by using a single crystal rutile titanium dioxide photoanode and a Pt counter electrode with a chemical bias.[15] The reaction is determined by three factors: (i) the solar irradiation needs to provide enough energy to excite the electron across the band gap (light harvesting process). (ii) The generated charges can effectively be generated and separated. (iii) The surface reaction with water to generate hydrogen. The overall efficiency is determined by the balance between the thermodynamics and kinetics of these processes.[7]

2.2 General Approaches for Water Splitting Methods

There are two methods for solar water splitting: (i) Photocatalytic water splitting and (ii) Photoelectrochemical (PEC) water splitting. Both of them are discussed below.

2.2.1 Photocatalytic Water Splitting

In this process photocatalytic powder is suspended in an electrolyte solution and is typically accompanied by stirring. The photochemical reaction occurs when the light energy is directly used to carry out the water splitting reaction on the catalytic powder.[6] The key steps in photocatalytic water splitting are as follows:[4] (i) photons are absorbed with energy higher than or equal to the semiconductors bandgap, generating electron-hole pairs; (ii) the photoexcited charges separate and migrate to the surface of the semiconductor without recombining; (iii) surface chemical reaction occur between the charges and electrolyte (e.g. H_2O) to generate H_2 and O_2 products by reduction and oxidation reactions respectively. The process will continue as long as irradiation of light continues. Figure 1 illustrates the basic principle of the overall water splitting vs SHE.

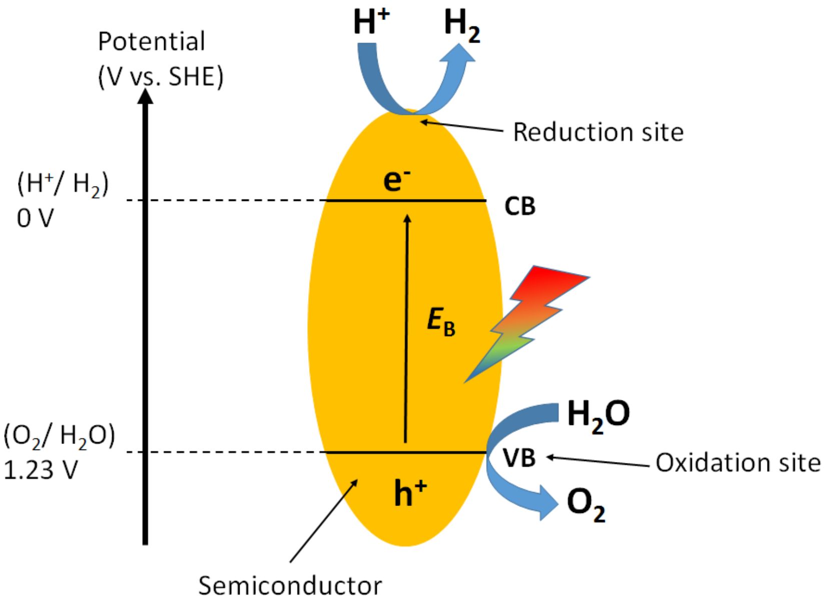

Figure 1: Schematic showing the overall water splitting on a semiconductor material. C.B., conduction band; V.B., valance band; E_g, band gap.

2.2.2 Photoelectrochemical (PEC) Water Splitting

Photoelectrochemical (PEC) water splitting reaction is defined as a particular case of photochemical reaction, where the photochemical reaction is accompanied by the flow of an electrical current through an external circuit within the system.[6] PEC water splitting is a well-established technique for the production of hydrogen.[15–17] Typically, the photocatalyst is deposited on to a substrate as a thin film to form either a photoanode or photocathode for carrying out the water splitting reaction. PEC water splitting works by converting solar energy into electrical energy using a semiconductor/ electrolyte interface. An issue with most semiconductors is the limited separation and transferability of photogenerated charge carriers. Thus in most cases, an external bias is applied to the semiconductor to assist the separation and migration of photoexcited electrons and holes.[18] The PEC cell converts water into its constituents hydrogen and oxygen using sunlight in a two electrode system; working electrode (where either p or n-type semiconductor is connected) and a counter electrode (typically platinum (Pt)), shown in figure 2. However, in most cases a reference electrode (typically Ag/ AgCl) is also employed to investigate the half reaction in the PEC cell. Upon illumination photons with energy equal to or greater than the bandgap (E_g) energy of the semiconductor generates holes that react with water molecules at the semiconductors surface generating oxygen by oxidation, whereas electrons generated travel through the substrate and are transported to the counter electrode by an external circuit where they reduce H^+ ions to hydrogen molecules. On the other hand, p-type semiconductor produces hydrogen and oxygen at the semiconductor electrode and counter electrode respectively.[14,16]

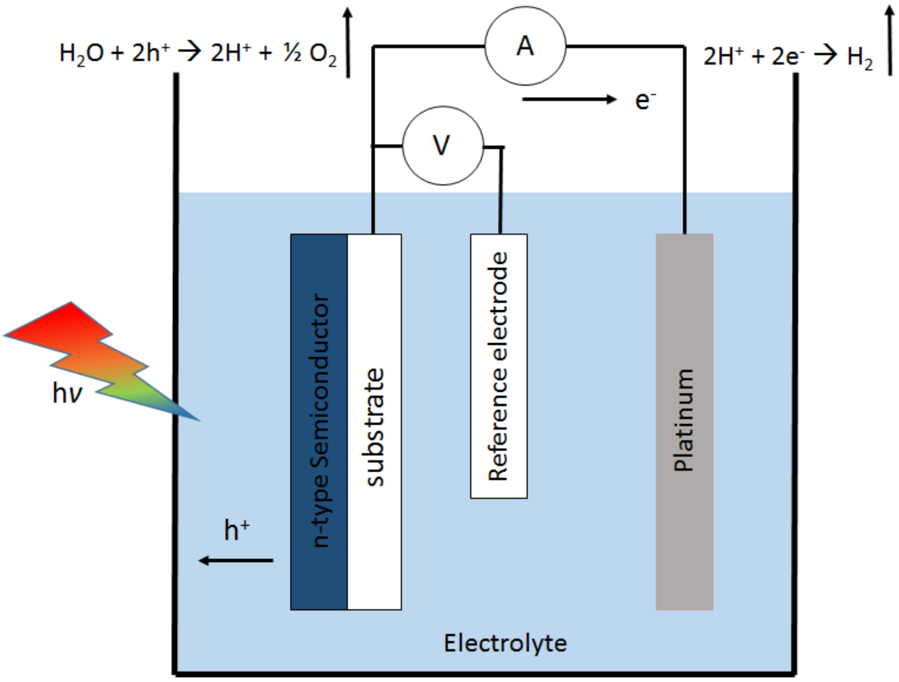

Figure 2: Diagram of a photoelectrochemical cell consisting of a photoanode semiconductor, reference electrode and platinum counter electrode.

2.2.2.1 Evaluating the Semiconductors Performance in a PEC Cell

To best evaluate the performance of any semiconductor electrode in a PEC cell, measuring its efficiency will provide a detailed description of its performance. There are a number of ways to evaluate the performance of a semiconductor electrode in literature[14,19–21] which are summarised below:

- **Solar-to-hydrogen conversion efficiency (STH)**: Also known as Benchmark efficiency, describes the overall efficiency of a PEC water splitting device exposed to AM 1.5 G illumination under unbiased conditions. STH efficiency is described as chemical energy produced divided by solar energy input. The chemical energy of hydrogen generated can be calculated from the rate of hydrogen generation (mmol H_2/s) multiplied by the change in Gibbs free energy per mole of hydrogen at room temperature (25°C). While the denominator of the STH equation is defined as the solar energy of input measured as a product of incident illumination power density (P_{total}, mW/cm^2) multiplied by the illuminated electrode area (cm^2).

$$STH = \left[\frac{\left(mmol\,\frac{H_2}{s}\right) x \left(237\,\frac{KJ}{mol}\right)}{P_{total}\left(\frac{mW}{cm^2}\right) x\ Area\ (cm^2)}\right]_{AM\ 1.5\ G} \qquad \textbf{(eq. 4)}$$

- **Applied bias photon-to-current efficiency (ABPE):** ABPE does not reflect the true solar-to-hydrogen efficiency conversion process due to an external bias being applied to measure this efficiency. Dependence on an external bias is not the only criteria to determine ABPE for water splitting process. Magnitude of photocurrent generated is an important factor towards generating higher efficiency in PEC process.

$$ABPE = \left[\frac{\left|j_{ph}\left(\frac{mA}{cm^2}\right)\right| x\ (1.23 - |V_b|)(V)\ x\ \eta_F}{P_{total}\left(\frac{mW}{cm^2}\right)}\right]_{AM\ 1.5\ G} \qquad \textbf{(eq. 5)}$$

Where j_{ph} is the photocurrent density obatained under an applied bias V_b.

- **Incident photon-to-current efficiency (IPCE)/ External quantum efficiency (EQE):** IPCE describes the photocurrent collected per incident photon flux as a function of illumination wavelength. IPCE/ EQE yields efficiency in terms of "electrons out per photons in". In terms of PEC water splitting, IPCE describes the maximum possible efficiency in which incoming light can produce hydrogen from water assuming all electrons are used for hydrogen evolution. IPCE is measured from a chronoamperometry (potentiostatic) measurement in a 3-electrode system vs. a monochromatic light at various wavelengths.

$$\text{IPCE}(\lambda) = \text{EQE}(\lambda) = \frac{\text{electrons/ cm}^2\text{/ s}}{\text{photons/cm}^2\text{/ s}} = \frac{\left| j_{ph} \left(\frac{mA}{cm^2}\right) \right| x\ 1239.8\ (V\ x\ nm)}{P_{mono} \left(\frac{mW}{cm^2}\right) x\ \lambda\ (nm)} \quad \textbf{(eq. 6)}$$

Where 1239.8 V x nm represents a multiplication of Planck’s constant) and the speed of light, P_{mono} is the calibrated and monochromated illumination power intensity in mW/ cm^2, and λ (nm) is the wavelength at which illumination power is measured.

- **Absorbed photon-to-current efficiency (APCE)/ Internal quantum efficiency (IQE):** APCE/ IQE describes the photocurrent collected for every photon absorbed. APCE is used to establish a relationship between maximum photon absorbed with minimum charge carrier movement within the semiconductor.

$$\text{APCE}(\lambda) = \text{IQE}(\lambda) = \frac{\left| j_{ph} \left(\frac{mA}{cm^2}\right) \right| x\ 1239.8\ (\text{V}\ x\ nm)}{P_{mono} \left(\frac{mW}{cm^2}\right) x\ \lambda\ (nm)\ x\ (1-10^{-A})} \quad \textbf{(eq. 7)}$$

Where absorbance (*A*) is the logarithmic ratio of the measured output of light intensity vs. the initial input light intensity determined by UV-Vis spectroscopy.

2.3 Physics of Semiconductor/ Electrolyte Contact

An important factor which needs to be discussed is the semiconductor/ electrolyte interface. As the water splitting reaction takes place at this interface it is important to know what mechanism occurs here and how it may affect the reaction.

The theory of semiconductor – electrolyte interface is well defined.[14,16] Upon placing the metal ferrite semiconductor in the electrolyte solution, an electric current initially flows across the junction until an electronic equilibrium is reached, where the Fermi energy of electrons in the metal ferrite solid (E_F) is equal to the redox potential of the electrolyte (E_{redox}). A space - charge layer forms due to the transfer of electric charge producing a region either side of the junction where the charge distribution differs from bulk material. On the electrolyte side of the junction Helmholtz double layer is formed followed by the Gouy – Chapman diffuse layer. On the semiconductor side of the junction the type of band bending depends on the Fermi level in the solid. The Fermi energy level depends on the electron and hole concentration i.e. on n- or p-type semiconductor. For a p-type semiconductor the Fermi energy level lies above the valance band, whereas the Fermi energy level of n-type semiconductor lies below the conduction band (figure 3). During the charge transfer process, a potential gradient across the interface is generated which leads to the bending of the energy bands either upwards (for n-type semiconductors) or downwards (for p-type semiconductors) (figure 4).

The flat band potential provides very useful information as it helps the location of the valance and conduction band edges of a semiconductor material. This is obtained by measuring the capacity of the semiconductor – electrolyte interface. This is obtained by measuring the capacity of the semiconductor – electrolyte interface. The semiconductor is put under a reverse bias, where a voltage is applied to increase the potential step across the interface, and the capacity is determined as a function of the applied potential. The space – charge capacity of the semiconductor material is in series with the Helmholtz layer. In the depletion area the Helmholtz layer capacity is greater than the semiconductor capacity, so the measured capacity is of the space – charge layer. This depends on the applied voltage according to Mott – Schottky.

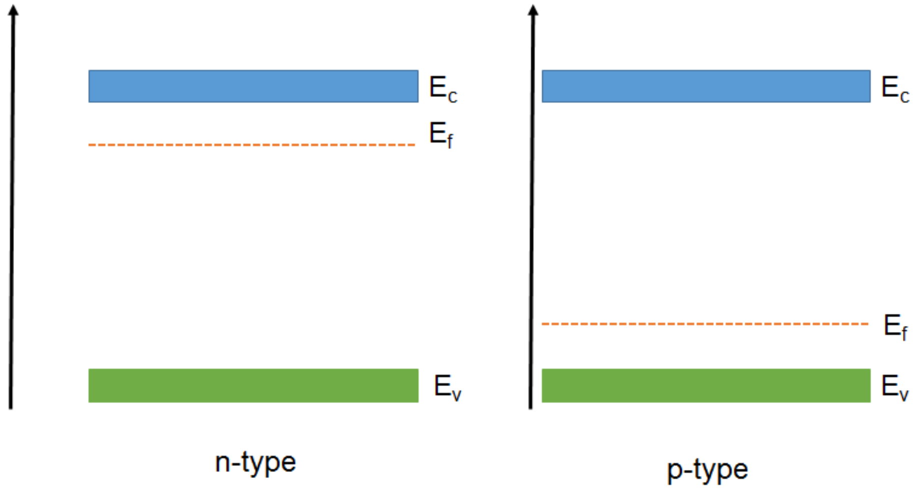

Figure 3: Diagram showing the fermi level of n-type and p-type semiconductor. E_c; conduction band, E_f; fermi level and E_v; valance band.

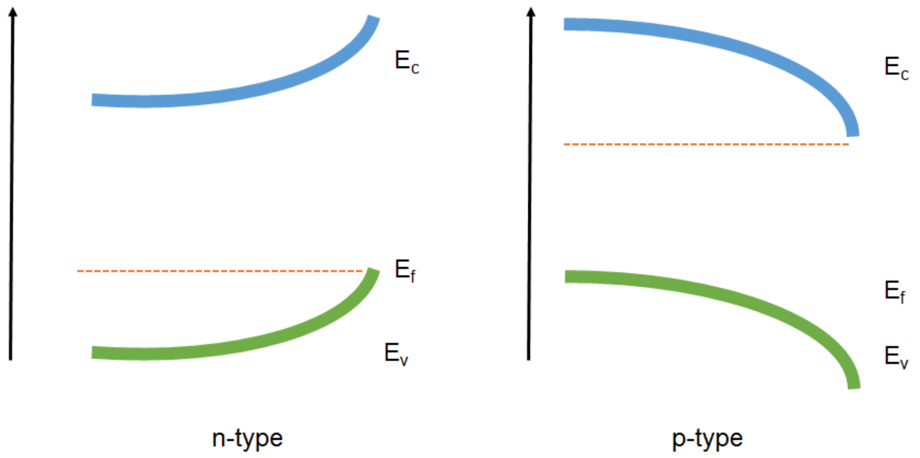

Figure 4: Diagram showing the band bending effect when a potential gradient is generated across the interface for n-type and p-type semiconductor. E_c; conduction band, E_f; fermi level and E_v; valance band.

Under illumination, a photovoltage is generated in the semiconductor from the separation of photogenerated electron – hole pairs in the band bending region. The charge separation occurs until the bands are flat, after which the charge separation cannot be increased by further illumination. Light leads to lowering of H^+/H_2 potential and the application of an external bias leads to an elevation of fermi energy level of cathode above the H^+/H_2 energy level, thus aiding electron transfer to H^+ ions in the electrolyte for hydrogen production. In Photoelectochemical (PEC) system the electrons generate hydrogen molecules either on Pt counter electrode in n-type semiconductor or on the semiconductor electrode in p-type semiconductor.[14]

2.4 Semiconductors for Solar Water Splitting

There are two types of semiconductor materials for solar water splitting: (i) p-type semiconductor and (ii) n-type semiconductor. A p-type semiconductor, also known as a photocathode, are used to reduce protons to hydrogen molecules (H_2) when a sufficient cathodic current is applied. Additionally, to successfully reduce protons to H_2, the conduction bands edge potential must be more negative that the hydrogen redox potential ($H^+/ H_2 = 0$ V). An n-type semiconductor, also known as a photoanode, are an oxygen evolving material, such that the electric field generated by band bending dives the holes to the surface to oxidise the water molecule to form oxygen (O_2). Additionally, to successfully oxidise water to O_2, the valance bands edge needs to be more positive than the oxygen redox potential ($H_2O/ O_2 = 1.23$ V).[22] Furthermore, both photocathodes and photoanodes need to be stable in an aqueous environment for solar water splitting reaction. Figure 5 shows the band edges of some typical photocathodes and photoanodes. The following sections below highlights the materials used for both photocathodes and photoanodes, for solar water splitting.

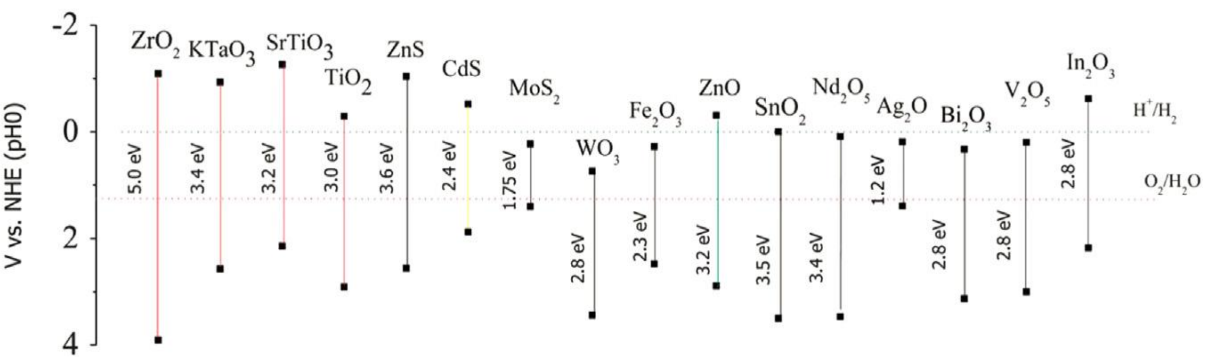

Figure 5: Diagram showing some typical semiconductor and the relationship between their band edges and redox potential of water splitting.[11]

2.4.1 Photocathodes for Solar Water Splitting

In this section, the literature will focus on the many different types of semiconductor materials as a photocathode. These will include: monometallic oxides, bimetallic oxides, III-V group materials, silicon, copper based chalcogenides and II-VI group materials.

2.4.1.1 Monometallic Oxides

2.4.1.1.1 CuO

Cupric oxide (CuO) is a p-type semiconductor material with an indirect band gap energy of 1.2 – 1.6 eV, which makes it an ideal candidate for visible light harvesting for solar water splitting for hydrogen evolution.[23–25] Additionally, CuO conduction band edge is in the appropriate position for doing the hydrogen evolution reaction,[26,27] and is non-toxic. CuO is theoretically capable of generating a photocurrent of 35 mA cm^{-2}.[28] Masudy-Panah *et al.*[29] have reported a current density of -2.5 mA cm^{-2}. This current is sufficient enough for generating hydrogen from solar water splitting, however by fabricating CuO composites further enhancements to the current density can be achieved for higher hydrogen yield.[30–32] Masudy-Panah *et al.* showed that a CuO/ Au-Pd composite could generate ~4 mA cm^{-2} current density yielding ~16 µmol of hydrogen gas (figure 6).[30] However, a major drawback of CuO is its stability due to photocorrosion during the water splitting reaction.

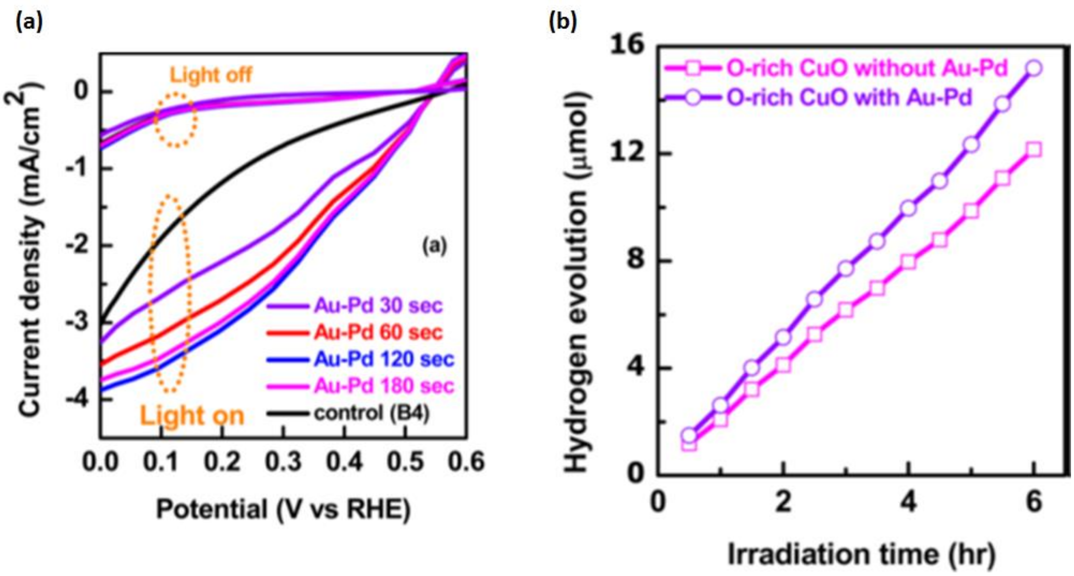

Figure 6: (a) Photocurrent density of CuO/ Au-Pd and **(b)** hydrogen evolution of CuO/ Au-Pd.[30]

2.4.1.1.2 Cu_2O

Cuprous oxide (Cu_2O) is another p-type copper based metal oxide which has received a huge international interest in research for solar water splitting application as a photocathode.[33–37] Cu_2O has a direct band gap of 1.9 – 2.2 eV, being able to absorb the visible light from the solar spectrum, and has a theoretical solar-to-fuel conversion efficiency of 18%.[38] Its conduction band is 0.7 eV more negative than the hydrogen evolution potential (vs NHE), making it a good candidate for hydrogen evolution, and its valance band is slightly more positive than the oxygen evolution potential.[38,39] Luo *et al.*[40] have demonstrated one of the highest photocurrent for Cu_2O reaching -10 mA cm^{-2}. This was achieved by altering the structure of Cu_2O from planar to a nanowire array. A major drawback of a planar structure is its diffusion length which is limited to around 200 nm, but in order to efficiently absorb sunlight, Cu_2O film thickness needs to be 1 μm thick.[39–41] Nanowire arrays however is able to solve this problem through its morphology control, combining efficient light harvesting along the full length of the wire with short radial diffusion distance.[40] A major setback for Cu_2O photocathode is its stability due to photocorrosion in aqueous environment, similar to CuO. However, there has been research into building protective passivating layers (ZnO:Al and TiO_2) by atomic layer deposition (ALD) to reduce recombination and improve stability.[41] Figure 7 shows a schematic representation. A high current of -7.6 mA cm^{-2} is achieved by this method.

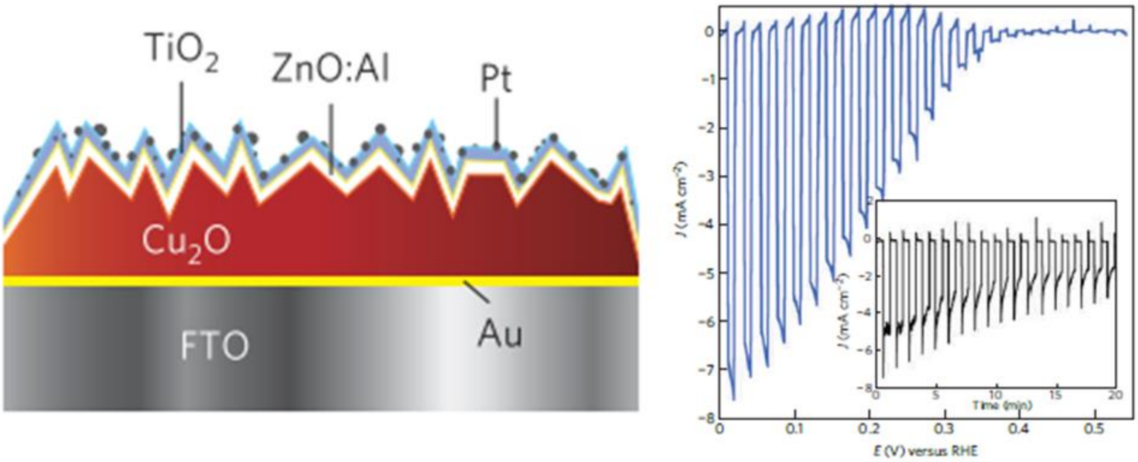

Figure 7: Schematic representation of Cu_2O photoelectrode with protective layers and its photocurrent.[41]

2.4.1.1.3 NiO

NiO is another p-type semiconductor with a wide bandgap between the ranges of 3.6 – 4.0 eV.[42,43] Due to its wide band gap NiO only has access to the UV part of the light spectrum. NiO thin films have shown to possess low resistance, high p-type concentration and high hole mobility.[44] NiO's valance band potential is positioned 0.54 V vs normal hydrogen electrode (NHE) at pH 7.[43,45] Due to the narrow wavelength range of excitation it limits its photocurrent where Mat-Teridi *et al.*[43] report a photocurrent density of ~-12 μA cm^{-2} (figure 8). However, sensitized NiO by visible light responsive substances (e.g. CdSe and bifunctional cyclometalated Ru(II)) have enhanced its current density performance.[46,47]

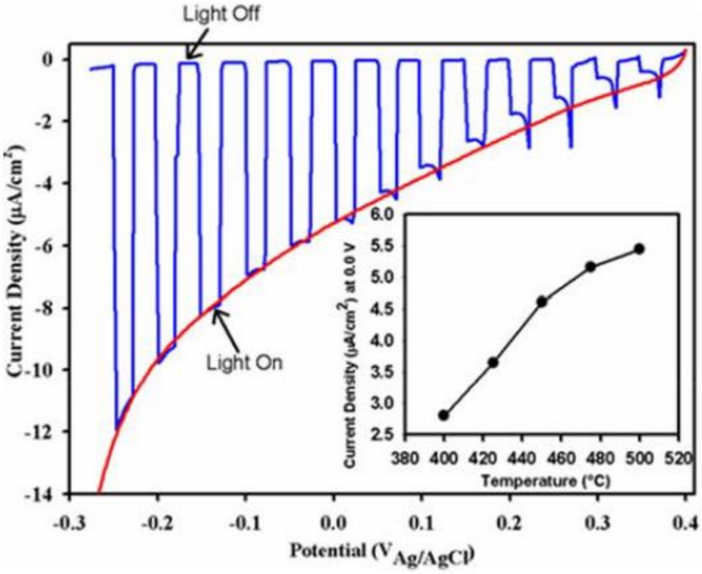

Figure 8: Diagram showing current density of NiO.

2.4.1.2 Bimetallic Oxides

2.4.1.2.1 $CaFe_2O_4$

$CaFe_2O_4$ was first discovered as a semiconductor material for water splitting by Matsumoto.[48] It is a p-type semiconductor with a bandgap of 1.9 eV with band edges suitably straddling the redox potential of water, where its conduction band potential sits ar -0.6 V and its valance band potential sits at 1.3 V vs NHE.[49] Diez-Garcia *et al.* showed photocurrent performance of

$CaFe_2O_4$ to reach -0.04 mA/ cm^2. The photo-response is relatively low due to poor charge separation and charge carrier mobility.[50] However, by doping $CaFe_2O_4$ with other catalysts (e.g. silver) a higher photocurrent response is achieved (figure 9).[51]

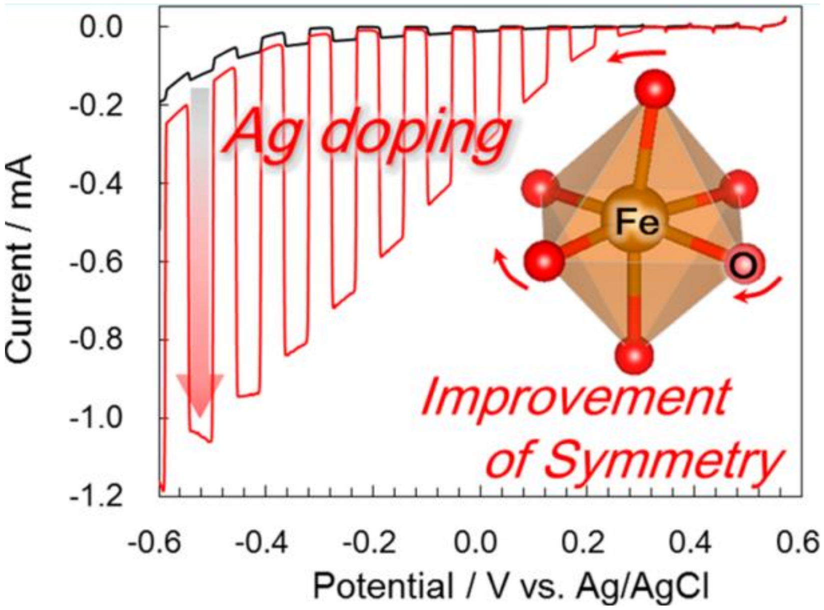

Figure 9: Graph showing *J*-*V* plot of the improved current density of plain $CaFe_2O_4$ (black line) by doping with silver (red line).[51]

2.4.1.2.2 $CuFeO_2$

$CuFeO_2$ has a ABO_2 delafossite structure (where A = monovalent ions e.g. Cu^+ and Ag^+; B = trivalent ions e.g. Al^{3+}, Ga^{3+}, Fe^{3+}, Mn^{3+}),[52,53] and has a band gap in the range of 1.5 – 1.6 eV which utilizes the entire range of visible light.[54] Additionally its conduction band potential is positioned at -0.7 V vs NHE, which is good for hydrogen reduction, and its valance band potential is at 0.8 V vs NHE.[55] Furthermore, $CuFeO_2$ is structurally stable in water and has relatively high photoactivity. Oh *et al.*[54] showed a photocurrent of 0.2 mA/

cm^2 at 0.6 V. Recent studies show that by using hybrid microwave annealing the activity of the $CuFeO_2$ electrode enhances, making it more attractive for water splitting application (figure 10).[56]

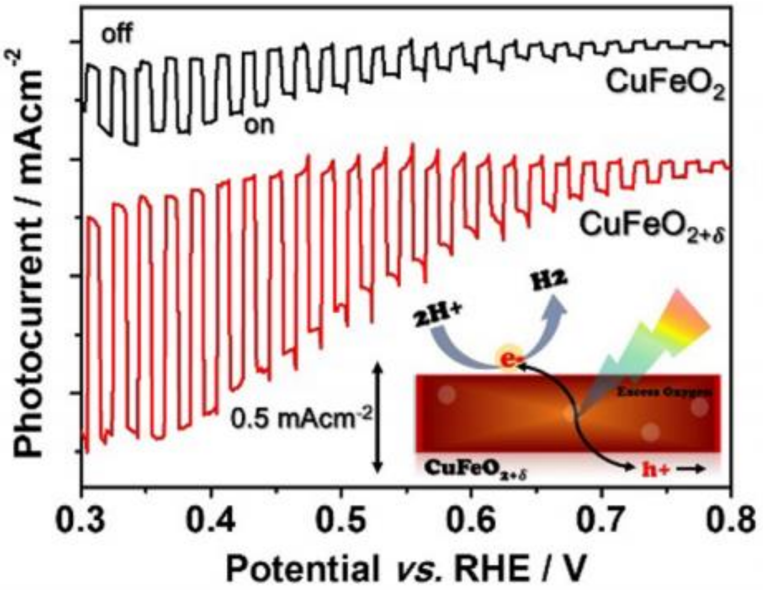

Figure 10: *J-V* plot of untreated $CuFeO_2$ (black line) and the post microwave treated $CuFeO_2$ (red line).[56]

2.4.1.2.3 $LaFeO_3$

$LaFeO_3$ is a p-type material with a perovskite structure (ABO_3) and has shown to be a promising material for solar water splitting for hydrogen evolution.[57,58] $LaFeO_3$ has a bandgap of 2.4 eV, allowing it to access the visible light region, has its conduction band -1.11 V above the reduction potential of hydrogen and has high stability in aqueous environment.[59] Wheeler *et al.*[58] fabricated $LaFeO_3$ photocathode by electrodeposition technique and yielded a current density of -0.1 mA cm^{-2}. However, its performance for water reduction was not impressive due to poor catalytic performance. Recent research shows that by doping the $LaFeO_3$ with metals having a 2+ oxidation state and similar radii to that of Fe^{3+} (e.g. Mg^{2+} and Zn^{2+}) it causes structural, electrical and magnetic changes to $LaFeO_3$.[60–62] This led to higher photocurrents being generated (figure 11).

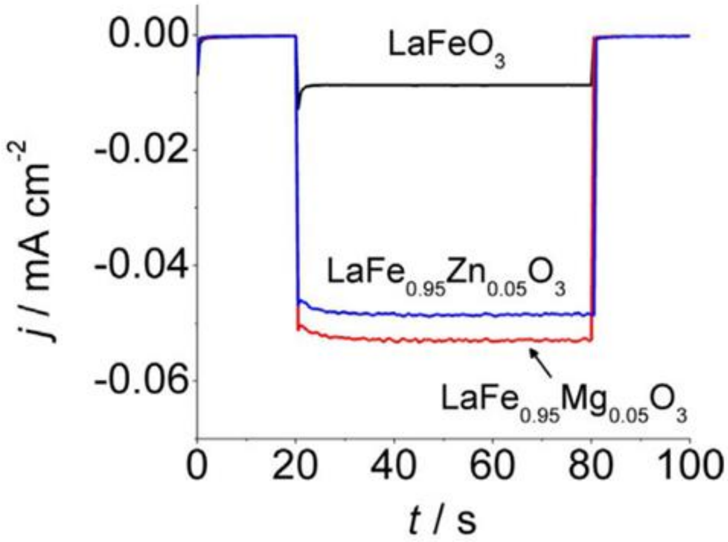

Figure 11: Plot showing the current densities of $LaFeO_3$ (black line) and $LaFeO_3$ doped with either Zn (blue line) or Mg (red line).

2.4.1.3 Group III-V Materials

Group III-V materials which have relatively narrow band gaps have shown high photoresponse. Most common group III-V materials are InP, GaP and GaInP. These three materials are discussed below.

2.4.1.3.1 InP

InP (indium phosphide) has several attractive features for it to be used as a photocathode; its band gap value is 1.3 eV (allowing for visible light absorption), its conduction band edge potential is just above the water reduction potential and its surface recombination is low.[63,64] Due to these reasons InP has been studied as a photocathode material for water splitting.[65–67] Lee *et al.*[63] have achieved a remarkably high photocurrent of 37 mA cm^{-2} (figure 12) with a hydrogen production efficiency of 14% with an applied bias of 0.5 V. Although InP can produce high photocurrent, it suffers for poor stability in acidic electrolyte solution, but by adding protective layers (e.g. TiO_2 or NiO) to InP its stability is vastly improved.[63,68] Despite its excellent performance, due to the high cost of materials required for fabrication and fabrication processes, InP is limited in its scalability.

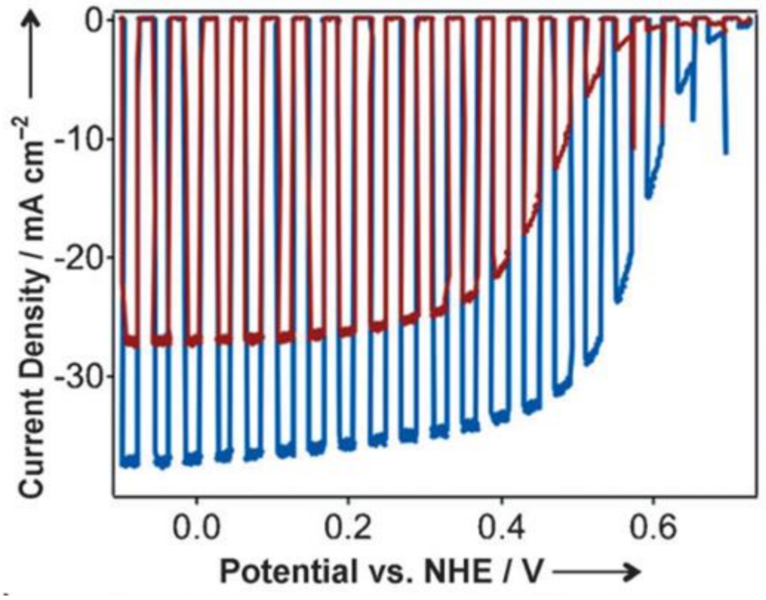

Figure 12: *J-V* plot of planar InP (red line) and nanopillar InP (blue line).[63]

2.4.1.3.2 GaP

The GaP (gallium phosphide) semiconductor material has an indirect band gap of 2.26 eV with its conduction band potential energy at -0.6 V vs NHE (pH = 0), making it a good candidate for solar hydrogen generation from water splitting.[69,70] Nanowire arrays of GaP presents an opportunity for nearly 100%

light absorption across all wavelengths due to photonic effects, which provides light concentration at each nanowire, as well as lowering the reflective index causing a decrease in reflection loss compared to planar GaP.[71] With the nanowire array there is an increased surface area which allows for better performances compared to planar samples, however there is also an increased chance for surface recombination effect which will lower the rate of reaction.[71] Figure 13 compared the current density of planar GaP to that of the nanowire GaP.

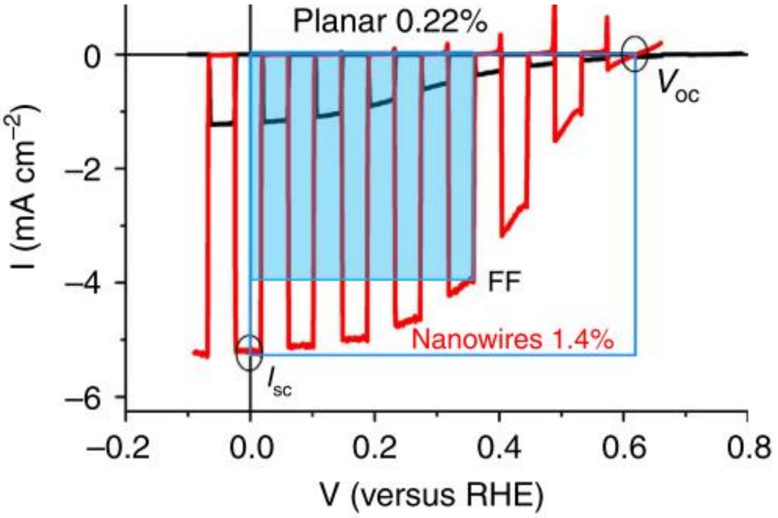

Figure 13: *J*-*V* plot comparison of planar GaP (black line) and nanowire GaP (red line).[71]

2.4.1.3.3 $GaInP_2$

Khaselev and Turner demonstrated that $GaInP_2$ PEC cell can provide 12.4% solar to hydrogen conversion, proving that high efficiency PEC water splitting is possible if properly engineered.[72] $GaInP_2$ photocathode has a direct band gap 1.83 eV which is ideal for hydrogen evolution from water splitting.[73] Gu *et* *al.*[74] have shown that by incorporating TiO_2 and a cobalt catalyst on to the $GaInP_2$ semiconductor, not only does the materials current density increase significantly but its stability also hugely improves (figure 14).

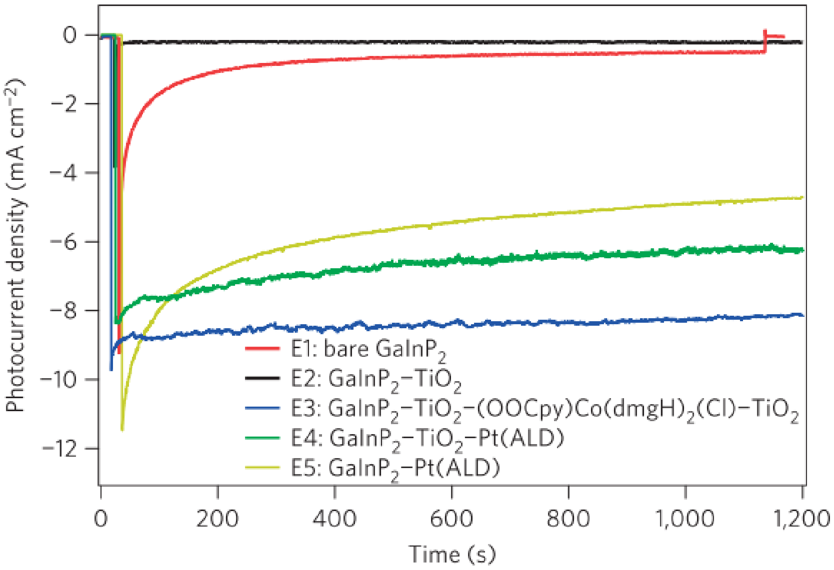

Figure 14: Current density of plain $GaInP_2$ compared to that of co-catalysed $GaInP_2$.[74]

2.4.1.4 Copper Based Chalcogenides

Copper chalcogenides have drawn a lot of interest due to three key reasons: (i) abundance, low-cost, reduced environmental impact; (ii) excellent properties such as appropriate band gaps, plasmonic properties charge carrier mobility and low thermal conductivity; (iii) they have low energy of formation of defects.[75] Recently $CuGaSe_2$ and $CuInS_2$ have been developed. These are discussed below.

2.4.1.4.1 $CuGaSe_2$

Copper gallium selenide ($CuGaSe_2$ (CGSe)) is frequently reported as a p-type semiconductor.[76] CGSe are promising is a material as a photocathode for water splitting because of their stability, long absorption edges and ability to tune its band structure by controlling compositions.[77,78] CGSe has a band gap of 1.7 eV.[78] Moriya *et al.*[77] have reported that $CuGaSe_2$ modified with CdS and Pt shows stable hydrogen evolution over a ten day period in an alkaline solution (figure 15). Although $CuGaSe_2$ possess excellent stability and hydrogen evolution capabilities, it requires large external bias due to shallow potential of the valance band edge.[78] Kim *et al.*[79,80] have shown that by tuning the band structure of CGSe by changing the compositional ratio of Ga/ Cu, the band structure can be altered providing deeper valance band edge and larger band gap.

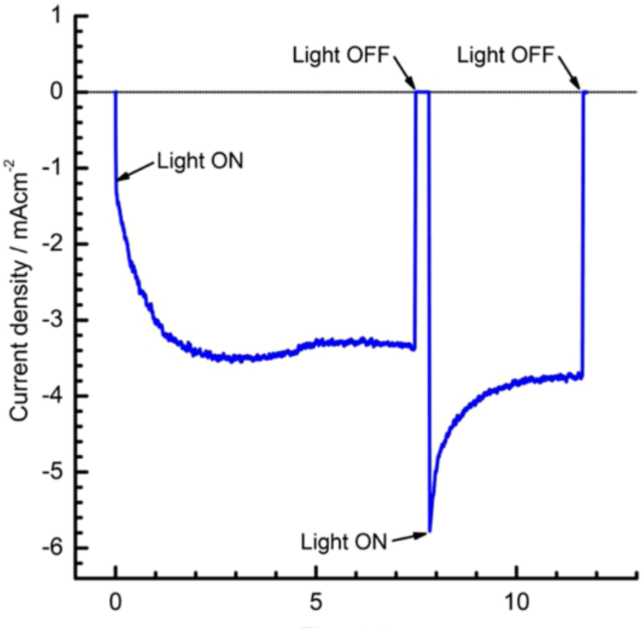

Figure 15: Current-time curve for $CuGeSe_2$ modified with Pt/ CdS.[77]

2.4.1.4.2 $CuInS_2$

Copper indium disulphide ($CuInS_2$) has a direct band gap of 1.5 eV, allowing it to absorb into the longer wavelength of visible light.[81] Furthermore $CuInS_2$ solar cells show a high theoretical solar energy conversion efficiency of ~25%,[82] where the highest reported efficiency is 11.4%.[83] Fabrication of $CuInS_2$ thin films are expensive, however electrodeposition technique have recently been employed in synthesising low-cost and scalable $CuInS_2$ thin film.[84,85] Zhao *et al.*[85] have shown that a $CuInS_2$ composite can achieve very high photocurrents of -13 mA cm^{-2} at 0 V vs RHE made by the electrodeposition technique (figure 16).

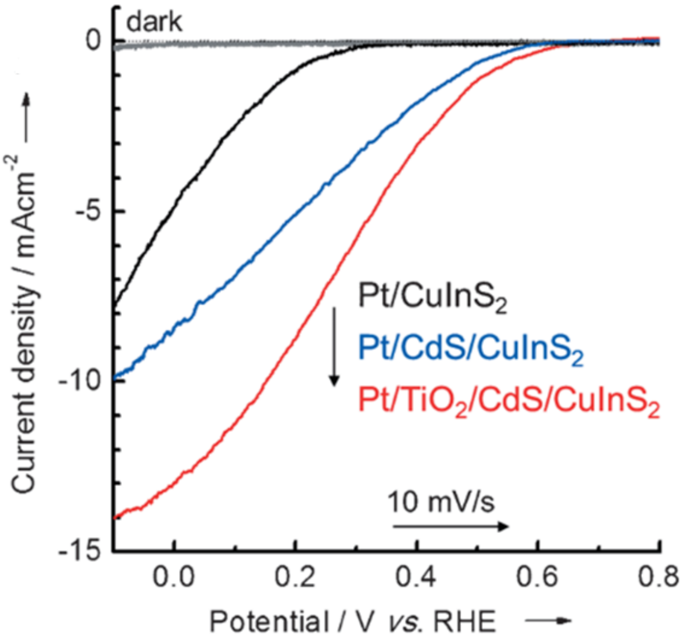

Figure 16: *J-V* curves for various $CuInS_2$ composites made by electrodeposition.[85]

2.4.1.5 Group II-VI Materials

Cadmium sulphide (CdS) and cadmium telluride (CdTe) are the most common group II-VI materials investigated for solar water splitting. They are discussed below.

2.4.1.5.1 CdS

Cadmium sulphide (CdS) has a direct band gap of 2.4 eV and appropriate band edges positions for water oxidation and reduction.[38] CdS is found to be an n-type semiconductor material due to formation of sulphur vacancies, but it suffers significantly from photocorrosion due to self-photo-oxidation at the electrode/ electrolyte interface by the photogenerated holes.[38] However, doping it with copper forms a p-type CdS semiconductor able to evolve hydrogen from the solar water splitting reaction with current a density of 0.6 mA cm^{-2} (figure 17).[86]

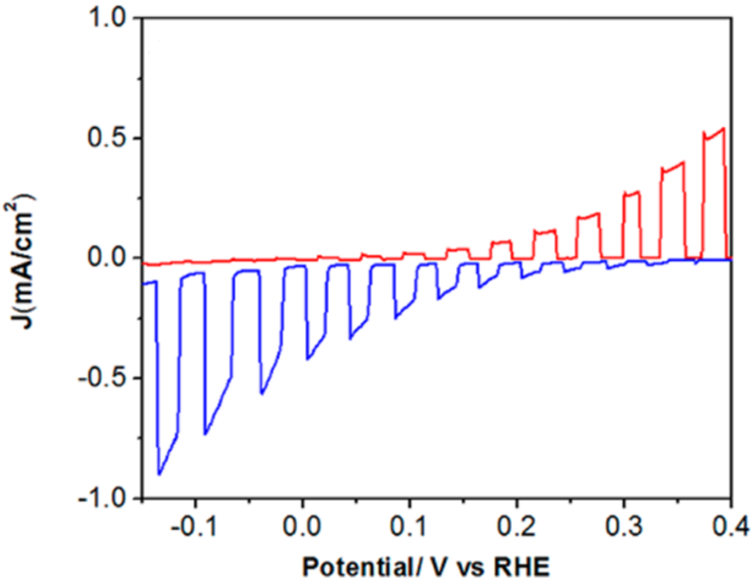

Figure 17: *J-V* curve for n-type CdS (red line) and p-type CdS:Cu (blue line).[86]

2.4.1.5.2 CdTe

Cadmium telluride (CdTe) is one of the leading thin film material for solar cells due to its optimum band gap of 1.44eV and the variety of film preparation.[38] CdTe films are typically a p-type semiconductor material due to the formation of Te vacancies. Mathew *et al.*[87] have reported that CdTe is capable of hydrogen evolution under one sun illumination and when modified with Ru both stability and hydrogen evolution efficiency improve.

2.4.1.6 Silicon

Silicon (Si) is the most widely used semiconductor for solar energy conversion due to its abundance. Aside from its use in photovoltaic solar cells, Si is promising as a photocathode because of its appropriate conduction band edge for hydrogen evolution.[88] Si has a narrow band gap of ~1.1 eV and its valance band is more negative than the oxidation potential for water.[38,89] A problem with planar Si is that about 25% of incident photons are reflected away from the Si surface which cannot generate electron-hole pairs.[89] Metal co-catalysts such as Pt[90] have been employed to lower the over potential to efficiently transfer photo-charges for hydrogen evolution. Oh *et al.*[89] have addressed the reflectance of planar Si by fabricating nanoporous black Si photocathodes. The Uv-Vis data shows that over the whole spectral range <2% of incident photons are reflected for a more efficient hydrogen production. Also the nanoporous Si generates more current density compared to polished Si (figure 18).

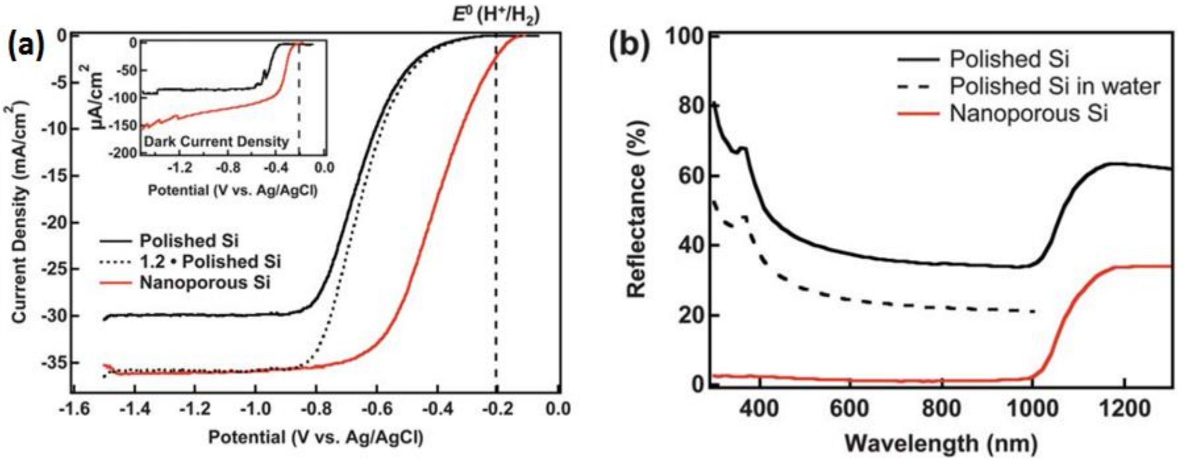

Figure 18: (a) Current density comparison of nanoporous Si and polished Si. **(b)** Reflectance measurement comparison of nanoporous Si and polished Si.[89]

2.4.2 Photoanodes for Water Splitting

In this section, the literature will focus on the many different types of semiconductor materials as a photoanode. These will include: monometallic oxides, bimetallic oxides and metal nitrides.

2.4.2.1 Monometallic Oxides

2.4.2.1.1 TiO_2

TiO_2 (titanium dioxide) is possible the most well-known photocatalytic material for water splitting application since the discovery by Fujishima and Honda.[15]

TiO_2 is an n-type material with a band gap of 3.2 eV (anatase) or 3.03 eV (rutile), its valence band is far more positive than the oxidation potential of water with the conduction band only just above the reduction potential of water (figure 19),[91] and has excellent stability in aqueous environment. However, due to its large band gap it is only able to access the UV part of the light spectrum meaning that its efficiency for water splitting is low. To improve its visible light absorption either narrowing its band gap or doping with cocatalysts have been done. Narrowing the band gap has been reported in microcrystalline TiO_2 films where it is doped with either nitrogen, carbon or sulphur.[92–94] Cocatalysts such as platinum, gold, silver and cobalt, have also been investigated.[95–98] The cocatalyst help the TiO_2 to access more of the visible light part of the spectrum for improved efficiency.

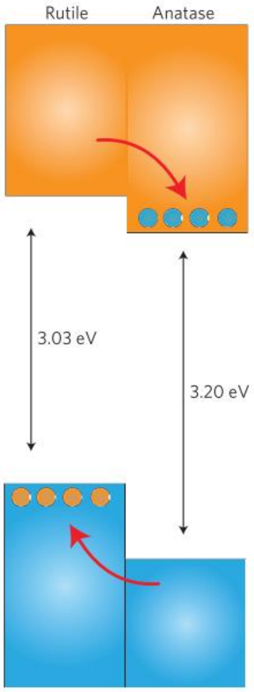

Figure 19: Proposed valence and conduction band alignment of anatase and rutile TiO_2 interface.[91]

2.4.2.1.2 α-Fe_2O_3

Alpha-Hematite (α-Fe_2O_3) is another n-type semiconductor material which has been extensively studies over the years.[99–103] Due to irons abundance (the earth's crust fourth most common element), non-toxicity and ability to absorb solar irradiation make iron oxide particularly attractive for use in solar water slitting.[104] α-Fe_2O_3 has a bad gap of ~2.1 eV which allows for 15.3% of theoretical solar to hydrogen (STH) efficiency, excellent stability under alkaline conditions and is environmentally friendly.[105] However, a major drawback of α-Fe_2O_3 is its poor electrical conducting property. Therefore, most α-Fe_2O_3 exhibit low PEC performance due to excessive charge recombination. A number of approaches have been taken to improve its electrical property; doping is commonly employed.[99,102,106] Another way method is synthesising 1-D nanorods, nanowires or nanotubes to shorten the pathway for photoexcited charge carriers to travel. Kim *et al.*[105] report a single-crystalline wormlike hematite photoanode for efficient solar water splitting where they achieve 4.32 mA cm^{-2} current density corresponding to 34% of the maximum limit expected of hematite with 2.1 eV bandgap, and have doped with co-catalysts (Pt and Co-Pi) to help improve the electrical conducting property of α-Fe_2O_3 (figure 20).

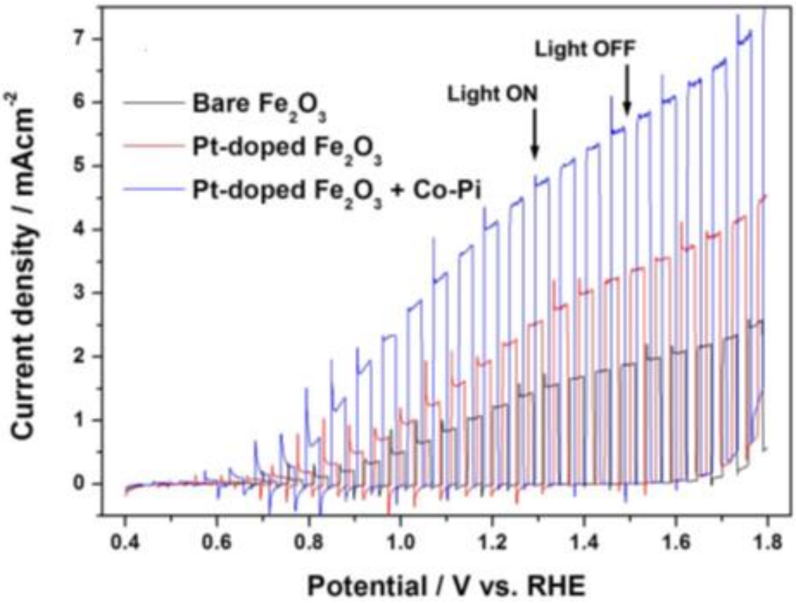

Figure 20: *J-V* curve for the PEC water oxidation reaction of hematite photoanodes.[105]

2.4.2.1.3 ZnO

Zinc oxide (ZnO) is another n-type semiconductor with a wide band gap of 3.37 eV, which limits the amount of solar absorption.[107] Its band gap is similar to TiO_2 but is significantly better due to its conduction of electrons and holes.[108–110] ZnO photoanode is not reliable and efficient in PEC water splitting due to material limitations such as photocorrosion in an aqueous environment under UV illumination. Degradation of ZnO in higher pH is more prevalent, even in dark.[110,111] Liu *et al.*[110] reported that by growing ultrathin titania shell on to ZnO nanowire its improved its stability and reached current densities of 0.7 mA cm^{-2}, the highest for doped or undoped ZnO. Figure 21 shows the current density of ZnO made by slightly different reaction conditions.

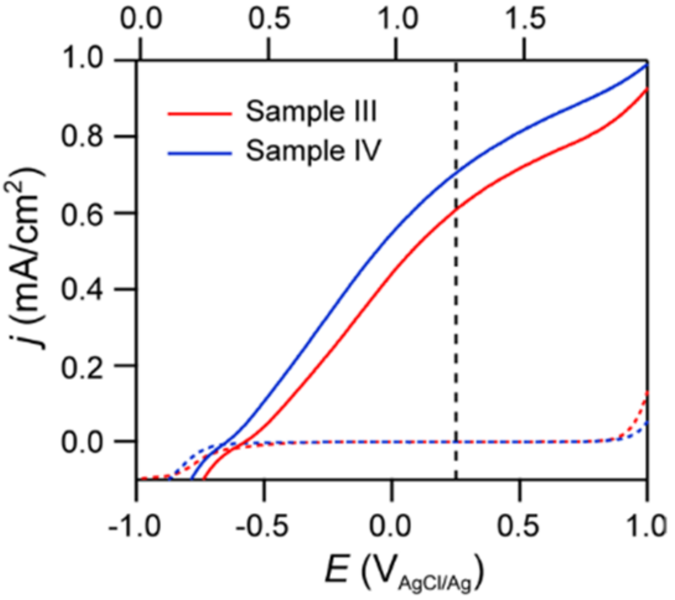

Figure 21: *J*-*V* plot of ZnO samples where sample IV had an extra annealing step.[110]

2.4.2.1.4 WO_3

Tungsten oxide (WO_3) is an n-type semiconductor with an indirect band gap ~2.5 - 2.8 eV which can capture about 12% of the solar spectrum and can absorb light in the visible spectrum up to 500 nm.[112] The theoretical maximum conversion efficiency of solar energy into H_2 for WO_3 photoanode is approximately 4.8%. Also, WO_3 is highly resistant to photocorrosion and has good stability in acidic aqueous solution (pH < 4) under illumination.[112] The visible light response of WO_3 can be enhanced with doping.[113–116] Kalanur *et al.*[114] have reported that by doping WO_3 with TiO_2 it improves its photocurrent density by 3.5 times than its undoped counterpart. Additionally, the IPCE measurement shows that when doped with TiO_2 a maximum value of 75% is achieved compared to 43% when undoped. This shows that when doped a greater portion of light is absorbed (figure 22).

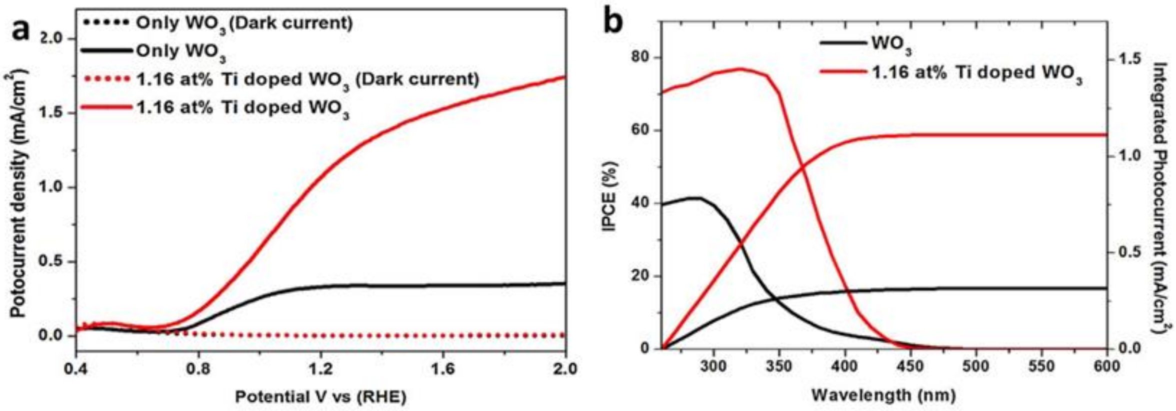

Figure 22: (a) *J-V* plot of plain WO_3 and Ti doped Wo_3. **(b)** IPCE of plain WO_3 and Ti doped WO_3.[114]

2.4.2.2 Bimetallic Oxides

2.4.2.2.1 $MgFe_2O_4$

Magnesium ferrite ($MgFe_2O_4$) belongs to a group of face-centred cubic close packed spinel structures and has a bandgap of 1.9 eV allowing it access to visible region part of the spectrum. [117] However, due to fast recombination of photogenerated charges it causes non-ideal photocatalytic activity. By incorporating reduced graphene oxide and MoS_2 the activity and performance of $MgFe_2O_4$ is improved.[117,118] Another way to overcome the limitations of bare $MgFe_2O_4$ is by fabricating 1D heterostructure, this can suppress charge recombination.[117,119]

2.4.2.2.2 $ZnFe_2O_4$

Zinc ferrite ($ZnFe_2O_4$) is a class of spinel ferrite (MFe_2O_4) and is a promising candidate for photoelectrode due to its narrow bandgap of about 2.0 eV, low rate of surface recombination and low onset potential.[120] $ZnFe_2O_4$ have been prepared by a number of techniques such as aerosol-assisted chemical vapour deposition,[121] atomic layer deposition[122] and spray pyrolysis,[123] but the photocurrent densities have remained below 0.4 mA/ cm^2. However, recently $ZnFe_2O_4$ nanorod array have been synthesised and have set a new benchmark for solar photocurrent of $ZnFe_2O_4$ at 1.7 mA/ cm^2 (figure 23).[124]

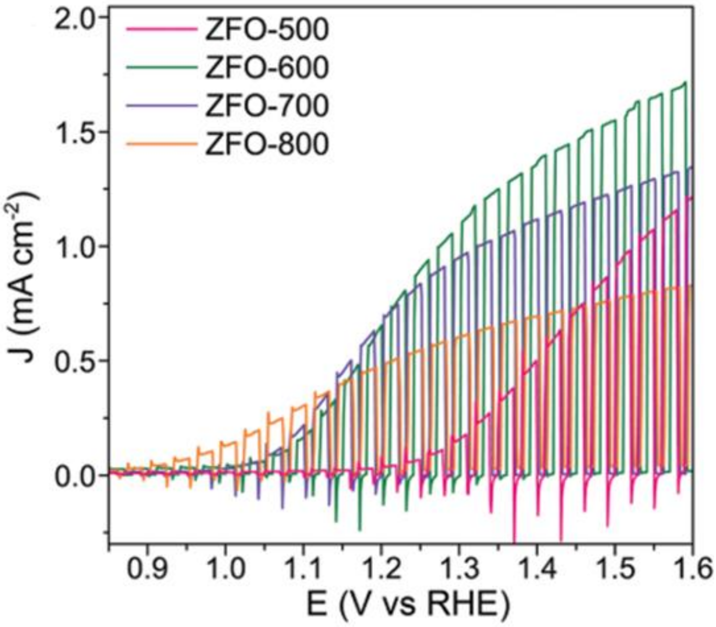

Figure 23: *J-V* plot of $ZnFe_2O_4$ at different annealing temperatures.[124]

2.4.2.2.3 $BiVO_4$

Bismuth vanadate ($BiVO_4$), also an n-type semiconductor material, has recently received attention as a potential photocatalyst for solar water splitting.[125–128] $BiVO_4$ has a direct band gap of 2.4 eV and can deliver a theoretical maximum photocurrent density of 7.5 mA cm^{-2} under AM 1.5G illumination, corresponding to STH conversion efficiency of 9.2%.[127] Its conduction band position is located near the H_2 evolution potential, and a relatively low onset potential and a much higher photocurrent density at low potential. The carrier transport in $BiVO_4$ is slow resulting in higher recombination rate of charges.[125] Strategies have been developed to overcome these drawbacks which involve metal doping or construction of heterojunction structures (figure 24).[128,129]

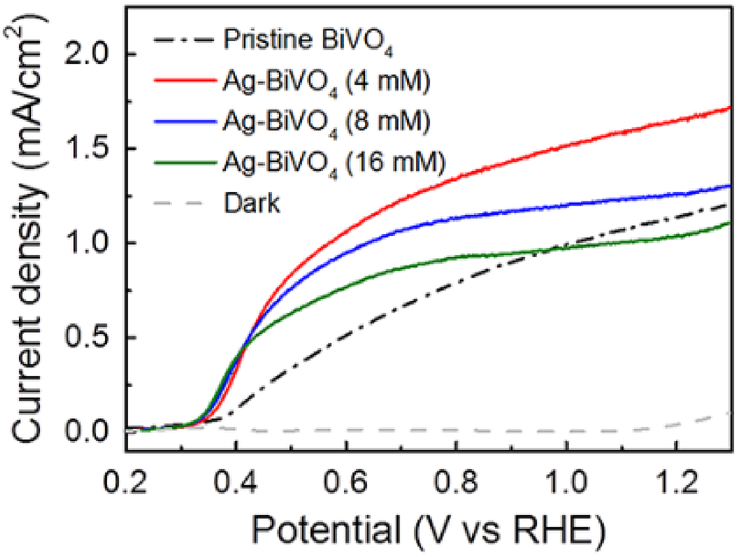

Figure 24: *J-V* plot of $BiVO_4$ doped with different concentrations of Ag compared to pristine $BiVO_4$.[128]

2.4.2.3 Metal Nitride

2.4.2.3.1 TaON

Tantalum oxynitride (TaON) is a promising visible light active photoanode with a band gap of 2.5 eV.[130] Most TaON has a band structure which straddles the redox potential water, suggesting that they can do overall water splitting. However, TaON suffer from poor stability due to self-oxidation by photogenerated holes. This can be addressed by loading cocatalysts on to TaON.[131] Ruthenium has been added onto TaON as such a cocatalyst for addressing the self-oxidation problem. Recent studies have shown that the photoactivity of TaON can be enhanced by incorporating ruthenium.[132]

2.4.2.3.2 Ta_3N_5

Tantalum nitride (Ta_3N_5), an n-type semiconductor, has a band gap of 2 eV and suitable band positions for solar water splitting, where the valance band lies as 1.6 V and conduction band lies at -0.4 V (vs NHE at pH = 0).[133,134] This allows for visible light absorption up to 600 nm. Ta_3N_5 suffers from poor charge transport and low photocurrent efficiency.[135] To address this issue research into 1D structures in the form of nanorods has been investigated. Li *et al.*[136] have fabricated vertically aligned Ta_3N_5 nanorod array yielding high crystallinity and high PEC water splitting performance, where a photocurrent density of 3.8 mA cm^{-2} is achieved at 1.23 V vs RHE. They also reported a maximum incident photon to current conversion efficiency (IPCE) of 41.3% (figure 25).

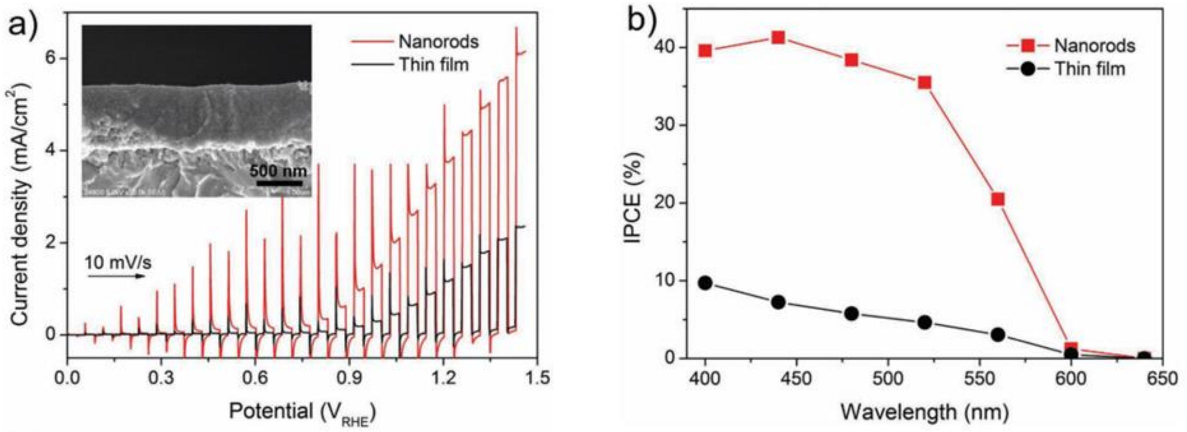

Figure 25: **(a)** *J-V* plot comparison of planar Ta_3N_5 and nanorod Ta_3N_5. **(b)** IPCE comparison of thin film Ta_3N_5 and nanorod Ta_3N_5.

2.5 Semiconductor Fabrication Techniques

Over the years a number of different techniques have been employed to fabricate metal ferrite semiconductor materials such as: spin coating, spray pyrolysis, atomic layer deposition (ALD), magnetron sputtering, electrodeposition, aerosol-assisted chemical vapour deposition (AACVD), hydrothermal, sol-gel and pulsed laser deposition (PLD).[58,59,121,137–149] The detail for each techniques are described below.

2.5.1 Spin Coating

Spin coating dilute solutions onto a planar substrate is a common way of producing thin, uniform, film layers. Different thickness levels of films can be achieved by altering parameters during the spin coating process such as: viscosity of solution, rotational speed, spin time and layering of solution. During the process, solution is deposited onto the substrate and the substrate is rapidly accelerated to the desired rotational rate. The liquid flows radially, due to centrifugal force, and the excess liquid is expelled of the substrates edge. The film continues to until pressure effects cause the films to reach equilibrium thickness or the solution turns solid-like due to an increase in viscosity from solvent evaporation. The final film thinning is due to solvent evaporation.[150]

2.5.2 Atomic Layer Deposition (ALD)

ALD is a modification of the chemical vapour deposition (CVD) where the film growth takes place I a cyclic manner. Usually one growth cycle consists of four steps: (i) exposure of the first precursor, (ii) purge of the reaction chamber, (iii) exposure of the second precursor and (iv) further purge of the reaction chamber. The growth cycles are repeated as many times necessary to achieve the desired film thickness. One cycle can take 0.5 s to a few seconds. The film growth is self-limiting; the amount of film material deposited in each cycle is constant. There are several advantages of the self-limiting growth mechanism: (i) film thickness depends only on the number of reaction cycles, making the thickness controlled, accurate and simple, (ii) there is less need of reactant flux homogeneity. ALD precursors can be either gases, volatile liquids or solids.[151]

2.5.3 Magnetron Sputtering

In this process a target plate is bombarded by energetic ions generated in a glow discharge plasma, which is situated in front of the target. This process causes the removal, i.e. “sputtering”, of atoms, which deposits on to a substrate as a thin film. Secondary electrons are also emitted from the targets surface due to the bombardment process, and these electrons play an important role in maintaining the plasma. Magnetrons make use of the magnetic field configured parallel to the target surface which constrains the secondary electrons to the vicinity of the target. Trapping the electrons like this increases the probability of an ionising electron atom collision. This leads to increased ion bombardment of the target, leading to higher sputtering rates, therefore, higher deposition rates.[152]

2.5.4 Electrodeposition

Electrodeposition, also known as electrophoretic deposition (EPD), is an electrochemical method used to deposit thin films on to a substrate. It is usually carried out in a cell consisting of two electrodes. The mechanism involves two steps: (i) an electric field is applied between two electrodes and charged particles suspended in a suitable solvent move towards oppositely charged electrodes, (ii) secondly, the particles accumulate at the deposition electrode and create a compact and homogeneous film. In order to apply this technique, it is essential to produce a stable suspension containing charged particles free to move when an electric field is applied. After the deposition process, the substrate is subjected to a heat treatment step to make the film dense and eliminate porosity.[153]

2.5.5 Aerosol-assisted chemical vapour deposition (AACVD)

AACVD is a technique used for transporting and depositing gas phase precursors with the assistance of a gas carrier (e.g. nitrogen/ compressed air) onto a substrate creating thin films. AACVD can be used to deposit onto large areas (e.g. glass/ steel) and small areas (e.g. microelectronics). This technique provides good film uniformity and composition control providing excellent coverage. Crystal structure and film morphologies can be controlled by altering temperature and deposition rate. There are three main steps involved in AACVD: (i) precursors are dissolved in a solvent, (ii) an aerosol is generated from the solution using a ultrasonic humidifier creating a “precursor mist”, which is then transported to the CVD reactor using the gas carrier, (iii) the solvent is evaporated when it reaches the substrate due to increased temperature, and the precursor material is deposited onto the substrate to yield the desired material.[154]

2.5.6 Hydrothermal

This method does not require the use of organic solvents or additional processing of products, making it a simple and environmentally friendly technique. The synthesis takes place in an autoclave, where a mixture of precursors is heated gradually to low temperatures of 100ºC – 300ºC. Due to heating followed by cooling, crystal nuclei are formed which then grow. This process has several advantages including, carrying out the synthesis at low temperatures, diverse size and shapes of crystals depending on the composition of the starting material and process temperature and pressure, high degree of crystallinity of the product and the high purity of product obtained.[155]

2.5.7 Sol-Gel

Also known as sol-gel dip-coating, consists of withdrawing a substrate from a fluid sol, gravitational draining and solvent evaporation and heating, resulting in the deposition of a thin solid film. This technique is inexpensive as it requires no specialist equipment. The sol-gel process uses inorganic or metal organic compounds as precursors. In aqueous or organic solvents these compounds are hydrolysed and condensed. Once the substrate has the material coated onto it heat is applied to evaporate the solvent and to condense the film leaving a solid thin film behind.[156]

2.5.8 Pulsed Laser Deposition (PLD)

PLD is a growth technique where photonic energy is coupled to the bulk starting material by electronic processes. During PLD, an intense laser pulse passes through an optical window of a vacuum chamber and is focused onto a solid or liquid surface target, where the laser is partially absorbed. A significant material removal occurs in the form of a plume. The material generated from the plume then recondenses onto the substrate where film growth occurs. The growth process can be enhanced by a passive or reactive gas or ion source.[157]

2.5.9 Spray Pyrolysis

This technique consists of a spray nozzle, precursor solution, a temperature controlled hot plate, syringe pump, ultrasonicator and a gas propellant. In the deposition process, the precursor solution is pumped to the nozzle where the ultrasonicator breaks down the solution to an aerosol. The gas flow (of neutral origin, e.g. compressed air or nitrogen) uniformly disperses the aerosol as it comes out of the nozzle tip over the substrate, which rests on top of a temperature controlled hot plate. The film thickness depends on the distance between the nozzle tip and substrate, substrate temperature, concentration of precursor, and the quantity of precursor sprayed. The film formation depends on the process of droplets landing on to the substrate and solvent evaporation. The ideal condition for film deposition is when the approaching droplets solvent evaporates just as it lands on the substrate.[158] This technique compared to ones such as PLD, sputtering and ALD as you will not require specific precursors, is low cost and is scalable to larger sizes. Also the films formed are well adhered, very uniform and synthesised very quickly e.g. minutes.

2.6 Summary

In this chapter we have investigated the principle of water splitting, the general approaches to water splitting, how to evaluate the materials performance, the physics of the electrode/ electrolyte interface, the types of semiconductor materials for water splitting and ways of fabricating the semiconductors. For high efficiencies the semiconductor must adhere to three conditions: (i) appropriate band edges, (ii) appropriate band gap and (iii) high chemical stability. The conduction and valance bands should straddle the redox potential of water and the band gap should be between 1.8 - 2.2 eV for maximum visible light absorption. At present most materials do not cover all these criteria’s. Further to these criteria’s the semiconductor materials should be environmentally friendly as to not pollute the environment. A lot of the high performing materials are fabricated using expensive non-saclable techniques such as PLD, ALD and sputtering. A simple low-cost fabrication technique which is scalable is required such as spray pyrolysis.

Reference

(1) Barber, J. Photosynthetic Energy Conversion: Natural and Artificial. *Chem. Soc. Rev.* **2009**, *38* (1), 185–196.

(2) van de Krol, R.; Grätzel, M. *Photoelectrochemical Hydrogen Production*; Spriger Science & Business Media: New York, USA, 2011.

(3) Xie, G.; Zhang, K.; Guo, B.; Liu, Q.; Fang, L.; Gong, J. R. Graphene-Based Materials for Hydrogen Generation from Light-Driven Water Splitting. *Adv. Mater.* **2013**, *25* (28), 3820–3839.

(4) Abe, R. Recent Progress on Photocatalytic and Photoelectrochemical Water Splitting under Visible Light Irradiation. *J. Photochem. Photobiol. C Photochem. Rev.* **2010**, *11* (4), 179–209.

(5) Luca, G.; Aguirre, M. H.; Selli, E. Hydrogen Production by Photocatalytic Steam Reforming of Methanol on Noble. *J. Catal.* **2010**, *273* (2), 182–190.

(6) Ahmad, H.; Kamarudin, S. K.; Minggu, L. J.; Kassim, M. Hydrogen from Photo-Catalytic Water Splitting Process : A Review. *Renew. Sustain. Energy Rev.* **2015**, *43*, 599–610.

(7) Tachibana, Y.; Vayssieres, L.; Durrant, J. R. Artificial Photosynthesis for Solar Water-Splitting. *Nat. Photonics* **2012**, *6* (8), 511–518.

(8) Wang, Y.; Suzuki, H.; Xie, J.; Tomita, O.; Martin, D. J.; Higashi, M.; Kong, D.; Abe, R.; Tang, J. Mimicking Natural Photosynthesis: Solar to Renewable H2Fuel Synthesis by Z-Scheme Water Splitting Systems.

Chem. Rev. **2018**, *118* (10), 5201–5241.

(9) Osterloh, F. E. Inorganic Nanostructures for Photoelectrochemical and Photocatalytic Water Splitting. *Chem. Soc. Rev.* **2013**, *42* (6), 2294–2320.

(10) Tang, S. J.; Moniz, S. J. A.; Shevlin, S. A.; Martin, D. J.; Guo, Z.-X.; Tang, J. Visible-Light Driven Heterojunction Photocatalysts for Water Splitting – a Critical Review. *Energy Environ. Sci.* **2015**, *8*, 731–759.

(11) Pan, H. Principles on Design and Fabrication of Nanomaterials as Photocatalysts for Water-Splitting. *Renew. Sustain. Energy Rev.* **2016**, *57*, 584–601.

(12) Joy, J.; Mathew, J.; George, S. C. Nanomaterials for Photoelectrochemical Water Splitting - Review. *Int. J. Hydrogen Energy* **2018**, 1–14.

(13) Maeda, K. Z-Scheme Water Splitting Using Two Different Semiconductor Photocatalysts. *ACS Catal.* **2013**, *3* (7), 1486–1503.

(14) Choudhary, S.; Upadhyay, S.; Kumar, P.; Singh, N.; Satsangi, V. R.; Shrivastav, R.; Dass, S. Nanostructured Bilayered Thin Films in Photoelectrochemical Water Splitting - A Review. *Int. J. Hydrogen Energy* **2012**, *37* (24), 18713–18730.

(15) Fujishima, a; Honda, K. Electrochemical Photolysis of Water at a Semiconductor Electrode. *Nature* **1972**, *238*, 37–38.

(16) Grätzel, M. Photoelectrochemical Cells. *Nature* **2001**, *414* (6861), 338–

344.

(17) Lewis, N. S. Light Work with Water. *Nature* **2001**, *414* (6864), 589–590.

(18) Governments, S.; Sciences, N. *From Molecules to Materials*; 2012.

(19) Chen, Z.; Dinh, H. N.; Miller, E. *Photoelectrochemical Water Splitting: Standards, Experimental Methods, and Protocols*; 2013.

(20) Hisatomi, T.; Kubota, J.; Domen, K. Recent Advances in Semiconductors for Photocatalytic and Photoelectrochemical Water Splitting. *Chem. Soc. Rev.* **2014**, *43* (22), 7520–7535.

(21) Chen, Z.; Jaramillo, T. F.; Deutsch, T. G.; Kleiman-Shwarsctein, A.; Forman, A. J.; Gaillard, N.; Garland, R.; Takanabe, K.; Heske, C.; Sunkara, M.; McFarland, E. W.; Domen, K.; Milled, E. L.; Dinh, H. N. Accelerating Materials Development for Photoelectrochemical Hydrogen Production: Standards for Methods, Definitions, and Reporting Protocols. *J. Mater. Res.* **2010**, *25* (1), 3–16.

(22) Warren, E. L.; McKone, J. R.; Boettcher, S. W.; Mi…, Q.; Lewis, N. S. Solar Water Splitting Cells. *Chem. Rev.* **2010**, *110*, 6446–6473.

(23) Kushwaha, A.; Moakhar, R. S.; Goh, G. K. L.; Dalapati, G. K. Morphologically Tailored CuO Photocathode Using Aqueous Solution Technique for Enhanced Visible Light Driven Water Splitting. *"Journal Photochem. Photobiol. A Chem.* **2017**, *337*, 54–61.

(24) Masudy-panah, S.; Moakhar, R. S.; Chua, C. S.; Kushwaha, A.; Wong, T. I.; Dalapati, G. K. Rapid Thermal Annealing Assisted Stability and

Efficiency Enhancement in a Sputter Deposited CuO. *RSC Adv.* **2016**, *6*, 29383–29390.

(25) Chiang, C.; Shin, Y.; Aroh, K.; Ehrman, S. Copper Oxide Photocathodes Prepared by a Solution Based Process. *Int. J. Hydrogen Energy* **2012**, *37* (10), 8232–8239.

(26) Chiang, C.; Aroh, K.; Franson, N.; Satsangi, V. R.; Dass, S.; Ehrman, S. Copper Oxide Nanoparticle Made by Flame Spray Pyrolysis for Photoelectrochemical Water Splitting e Part II . Photoelectrochemical Study. *Int. J. Hydrogen Energy* **2011**, *36* (24), 15519–15526.

(27) Long, M.; Beranek, R.; Cai, W.; Kisch, H. Hybrid Semiconductor Electrodes for Light-Driven Photoelectrochemical Switches. *Electrochim. Acta* **2008**, *53* (14), 4621–4626.

(28) Liu, C.; Dasgupta, N. P.; Yang, P. Semiconductor Nanowires for Artificial Photosynthesis. *Chem. Mater.* **2014**, *26*, 415–422.

(29) Masudy-panah, S.; Moakhar, R. S.; Chua, C. S.; Tan, H. R.; Wong, T. I.; Chi, D.; Dalapati, G. K. Nanocrystal Engineering of Sputter-Grown CuO Photocathode for Visible-Light-Driven Electrochemical Water Splitting. *ACS Appl. Mater. Interfaces* **2016**, *8*, 1206−1213.

(30) Masudy-panah, S.; Moakhar, R. S.; Chua, C. S.; Kushwaha, A.; Dalapati, G. K. Stable and Efficient CuO Based Photocathode through Oxygen-Rich Composition and Au − Pd Nanostructure Incorporation for Solar- Hydrogen Production. *ACS Appl. Mater. Interfaces* **2017**, *9*, 27596–27606.

(31) Zhao, X.; Wang, P.; Yan, Z.; Ren, N. Ag Nanoparticles Decorated CuO Nanowire Arrays for Efficient Plasmon Enhanced Photoelectrochemical Water Splitting. *Chem. Phys. Lett.* **2014**, *609*, 59–64.

(32) Guo, X.; Diao, P.; Xu, D.; Huang, S.; Yang, Y.; Jin, T.; Wu, Q.; Xiang, M.; Zhang, M. CuO / Pd Composite Photocathodes for Photoelectrochemical Hydrogen Evolution Reaction. *Int. J. Hydrogen Energy* **2014**, *39* (15), 7686–7696.

(33) Hsu, Y.; Yu, C.; Chen, Y.; Lin, Y. Synthesis of Novel Cu 2 O Micro / Nanostructural Photocathode for Solar Water Splitting. *Electrochim. Acta* **2013**, *105*, 62–68.

(34) Li, C.; Li, Y.; Delaunay, J. A Novel Method to Synthesize Highly Photoactive Cu2O Microcrystalline Films for Use in Photoelectrochemical Cells. *ACS Appl. Mater. Interfaces* **2014**, *6* (1), 480–486.

(35) Liang, D.; Han, G.; Zhang, Y.; Rao, S.; Lu, S.; Wang, H.; Xiang, Y. Efficient H2 Production in a Microbial Photoelectrochemical Cell with a Composite Cu2O / NiO x Photocathode under Visible Light. *Appl. Energy* **2016**, *168*, 544–549.

(36) Chhetri, M.; Rao, C. N. R. Photoelectrochemical Hydrogen Generation Employing a Cu2O-Based Photocathode with Improved Stability and Activity by Using NixPy as the Cocatalyst. *Phys. Chem. Chem. Phys.* **2018**, *20*, 15300–15306.

(37) Wang, P.; Wen, X.; Amal, R.; Hau, Y. Introducing a Protective Interlayer

of TiO2 in Cu2O – CuO Heterojunction Thin Film as a Highly Stable Visible Light Photocathode. *RSC Adv.* **2015**, *5*, 5231–5236.

(38) Huang, Q.; Ye, Z.; Xiao, X. Recent Progress in Photocathodes for Hydrogen Evolution. *J. Mater. Chem. A* **2015**, *3*, 15824–15837.

(39) Jongh, P. . . . d.; Vanmaekelbergh, D.; Kelly, J. J. Photoelectrochemistry of Electrodeposited Cu2O. *J. Electrochem. Soc.* **2000**, *147* (2), 486–489.

(40) Luo, J.; Steier, L.; Son, M. K.; Schreier, M.; Mayer, M. T.; Gratzel, M. Cu2O Nanowire Photocathodes for Efficient and Durable Solar Water Splitting. *Nano Lett.* **2016**, *16* (3), 1848–1857.

(41) Paracchino, A.; Laporte, V.; Sivula, K.; Grätzel, M.; Thimsen, E. Highly Active Oxide Photocathode for Photoelectrochemical Water Reduction. *Nat. Mater.* **2011**, *10* (6), 456–461.

(42) Gupta, R. K. Ã.; Ghosh, K.; Kahol, P. K. Fabrication and Characterization of NiO / ZnO p – n Junctions by Pulsed Laser Deposition. *Phys. E Low-Dimensional Syst. Nanostructures* **2009**, *41* (4), 617–620.

(43) Mat-Teridi, M. A.; Tahir, A. A.; Senthilarasu, S.; Wijayantha, K. G. U.; Sulaiman, M. Y.; Ahmad-Ludin, N.; Ibrahim, M. A.; Sopian, K. Fabrication of NiO Photoelectrodes by Aerosol-Assisted Chemical Vapour Deposition (AACVD). *Phys. Status Solidi - Rapid Res. Lett.* **2014**, *8* (12), 982–986.

(44) Wang, J.; Lee, C.; Chen, Y.; Chen, C.; Chen, Y.; Lin, C.; Chen, Y.; Lin, C.; Chen, Y. Double Side Electroluminescence from Nanowire Heterojunctions. *Appl. Phys. Lett.* **2009**, *95*, 93–95.

(45) Dong, Y.; Chen, Y.; Jiang, P.; Wang, G.; Wu, X.; Wu, R. Efficient and Stable MoS2 / CdSe / NiO Photocathode for Photoelectrochemical Hydrogen Generation from Water. *Chem. an Asian J.* **2015**, *10*, 1660–1667.

(46) Ji, Z.; He, M.; Huang, Z.; Ozkan, U.; Wu, Y. Photostable p ‐ Type Dye-Sensitized Photoelectrochemical Cells for Water Reduction. *J. Am. Chem. Soc.* **2013**, *135* (32), 11696–11699.

(47) Barcelo, I.; Guille, E.; Lana-villarreal, T.; Gomez, R. Preparation and Characterization of Nickel Oxide Photocathodes Sensitized with Colloidal Cadmium Selenide Quantum Dots. *J. Phys. Chem. C* **2013**, *117* (44), 22509–22517.

(48) Matsumoto, Y.; Omae, M.; Sugiyama, K.; Sato, E. New Photocathode Materials for Hydrogen Evolution: Calcium Iron Oxide (CaFe2O4) and Strontium Iron Oxide (Sr7Fe10O22). *J. Phys. Chem.* **1987**, *91* (3), 577–581.

(49) Ida, S.; Yamada, K.; Matsunaga, T.; Hagiwara, H.; Matsumoto, Y.; Ishihara, T. Preparation of P-Type CaFe2O 4 Photocathodes for Producing Hydrogen from Water. *J. Am. Chem. Soc.* **2010**, *132* (49), 17343–17345.

(50) Alfaifi, B. Y.; Ullah, H.; Alfaifi, S.; Tahir, A. A.; Mallick, T. K.

Photoelectrochemical Solar Water Splitting: From Basic Principles to Advanced Devices. *Veruscript Funct. Nanomater.* **2018**, *2*, 1–26.

(51) Sekizawa, K.; Nonaka, T.; Arai, T.; Morikawa, T. Structural Improvement of CaFe2O4by Metal Doping toward Enhanced Cathodic Photocurrent. *ACS Appl. Mater. Interfaces* **2014**, *6* (14), 10969–10973.

(52) Marquardt, M. A.; Ashmore, N. A.; Cann, D. P. Crystal Chemistry and Electrical Properties of the Delafossite Structure. *Thin Solid Films* **2006**, *496* (1), 146–156.

(53) Sheets, W. C.; Mugnier, E.; Barnabé, A.; Marks, T. J.; Poeppelmeier, K. R. Hydrothermal Synthesis of Delafossite-Type Oxides. *Chem. Mater.* **2006**, *18* (1), 7–20.

(54) Read, C. G.; Park, Y.; Choi, K.-S. Electrochemical Synthesis of P-Type CuFeO2 Electrodes for Use in a Photoelectrochemical Cell. *J. Phys. Chem. Lett.* **2012**, *3* (14), 1872–1876.

(55) Prevot, M. S.; Jeanbourquin, X. A.; Bouree, W. S.; Abdi, F.; Friedrich, D.; Krol, R. and de; Guijarro, N.; Formal, F. Le; Sivula, K. Evaluating Charge Carrier Transport and Surface States in CuFeO2 Photocathodes. *Chem. Mater.* **2017**, *29* (11), 4952–4962.

(56) Jang, Y. J.; Park, Y. Bin; Kim, H. E.; Choi, Y. H.; Choi, S. H.; Lee, J. S. Oxygen-Intercalated CuFeO $_2$ Photocathode Fabricated by Hybrid Microwave Annealing for Efficient Solar Hydrogen Production. *Chem. Mater.* **2016**, *28* (17), 6054–6061.

(57) Yu, Q.; Meng, X.; Wang, T.; Li, P.; Liu, L.; Chang, K.; Liu, G.; Ye, J. Highly Durable P-LaFeO3/n-Fe2O3 Photocell for Effective Water Splitting under Visible Light. *Chem. Commun.* **2015**, *51*.

(58) Wheeler, G. P.; Choi, K.-S. Photoelectrochemical Properties and Stability of Nanoporous P-Type $LaFeO_3$ Photoelectrodes Prepared by Electrodeposition. *ACS Energy Lett.* **2017**, No. 1, 2378–2382.

(59) Pawar, G. S.; Tahir, A. A. Unbiased Spontaneous Solar Fuel Production Using Stable LaFeO3 Photoelectrode. *Sci. Rep.* **2018**, *8* (1), 3501.

(60) Díez-García, M. I.; Gómez, R. Metal Doping to Enhance the Photoelectrochemical Behavior of LaFeO3 Photocathodes. *ChemSusChem* **2017**, *10* (11), 2457–2463.

(61) Bhat, I.; Husain, S.; Khan, W.; Patil, S. I. Effect of Zn Doping on Structural , Magnetic and Dielectric Properties of LaFeO 3 Synthesized through Sol – Gel Auto-Combustion Process. *Mater. Res. Bull.* **2013**, *48* (11), 4506–4512.

(62) Dong, S.; Xu, K.; Tian, G. Photocatalytic Activities of LaFe 1 2 x Zn x O 3 Nanocrystals Prepared by Sol – Gel Auto-Combustion Method. *J. Mater. Sci.* **2009**, *44* (10), 2548–2552.

(63) Lee, M. H.; Takei, K.; Zhang, J.; Kapadia, R.; Zheng, M.; Chen, Y.; Nah, J.; Matthews, T. S.; Chueh, Y.; Ager, J. W.; Javey, A. P-Type InP Nanopillar Photocathodes for Efficient Solar-Driven Hydrogen Production. *Angew. Chem. Int. Ed. Engl.* **2012**, *51*, 10760–10764.

(64) Hoffman, C. A.; Jarasiunas, K.; Gerritsen, H. J.; Nurmikko, A. V. Measurement of Surface Recombination Velocity in Semiconductors by Diffraction from Picosecond Transient Free-Carrier Gratings. *Appl. Phys. Lett.* **1978**, *536*, 536–539.

(65) Gao, L.; Cui, Y.; Wang, J.; Cavalli, A.; Standing, A.; Vu, T. T. T.; Verheijen, M. A.; Haverkort, J. E. M.; Bakkers, E. P. A. M.; Notten, P. H. L. Photoelectrochemical Hydrogen Production on InP Nanowire Arrays with Molybdenum Sulfi de Electrocatalysts. *Nano Lett.* **2014**, *14* (7), 3715–3719.

(66) Lin, Y.; Kapadia, R.; Yang, J.; Zheng, M.; Chen, K.; Hettick, M.; Yin, X.; Battaglia, C.; Sharp, I. D.; Ager, J. W.; Javey, A. Role of TiO2 Surface Passivation on Improving the Performance of p‑InP Photocathodes. *J. Phys. Chem. C* **2015**, *119* (5), 2308–2313.

(67) Ohmori, T.; Mametsuka, H.; Suzuki, E. Photocatalytic Hydrogen Evolution on InP Suspension with Inorganic Sacrificial Reducing Agent. *Int. J. Hydrogen Energy* **2000**, *25* (10), 953–955.

(68) Sun, K.; Kuang, Y.; Verlage, E.; Brunschwig, B. S.; Tu, C. W.; Lewis, N. S. Sputtered NiO x Films for Stabilization of p + N-InP Photoanodes for Solar-Driven Water Oxidation. *Adv. Energy Mater.* **2015**, 1402276.

(69) Liu, C.; Sun, J.; Tang, J.; Yang, P. Zn-Doped p‑Type Gallium Phosphide Nanowire Photocathodes from a Surfactant-Free Solution Synthesis. *Nano Lett.* **2012**, *12*, 5407–5411.

(70) Sun, J.; Liu, C.; Yang, P. Surfactant-Free, Large-Scale, Solution-Liquid-Solid Growth of Gallium Phosphide Nanowires and Their Use for Visible-Light-Driven Hydrogen Production from Water Reduction. *J. Am. Chem. Soc.* **2011**, *133* (48), 19306–19309.

(71) Standing, A.; Assali, S.; Gao, L.; Verheijen, M. A.; Dam, D. Van; Cui, Y.; Notten, P. H. L.; Haverkort, J. E. M.; Bakkers, E. P. A. M. Efficient Water Reduction with Gallium Phosphide Nanowires. *Nat. Commun.* **2015**, *6*, 1–7.

(72) Khaselev, O.; Turner, J. A. A Monolithic Photovoltaic-Photoelectrochemical Device for Hydrogen Production via Water Splitting. *Science (80-.).* **1998**, *280* (5362), 425–428.

(73) Macleod, B. A.; Steirer, K. X.; Young, J. L.; Koldemir, U.; Sellinger, A.; Turner, J. A.; Deutsch, T. G.; Olson, D. C. Phosphonic Acid Modi Fi Cation of GaInP 2 Photocathodes Toward Unbiased Photoelectrochemical Water Splitting. *ACS Appl. Mater. Interfaces* **2015**, *7* (21), 11346–11350.

(74) Gu, J.; Yan, Y.; Young, J. L.; Steirer, K. X.; Neale, N. R.; Turner, J. A. Water Reduction by a P-GaInP2 Photoelectrode Stabilized by an Amorphous TiO2 Coating and a Molecular Cobalt Catalyst. *Nat. Mater.* **2016**, *15*, 456–460.

(75) Coughlan, C.; Ibanez, M.; Dobrozhan, O.; Singh, A.; Cabot, A.; Ryan, K. M. Compound Copper Chalcogenide Nanocrystals. *Chem. Rev.* **2017**, *117* (9), 5865–6109.

(76) Marsen, B.; Cole, B.; Miller, E. L. Photoelectrolysis of Water Using Thin Copper Gallium Diselenide Electrodes. *Sol. Energy Mater. Sol. Cells* **2008**, *92* (9), 1054–1058.

(77) Moriya, M.; Minegishi, T.; Kumagai, H.; Katayama, M.; Kubota, J.; Domen, K. Stable Hydrogen Evolution from Cds-Modified CuGaSe2 Photoelectrode under Visible-Light Irradiation. *J. Am. Chem. Soc.* **2013**, *135* (10), 3733–3735.

(78) Kumagai, H.; Minegishi, T.; Moriya, Y.; Kubota, J.; Domen, K. Photoelectrochemical Hydrogen Evolution from Water Using Copper Gallium Selenide Electrodes Prepared by a Particle Transfer Method. *J. Phys. Chem. C* **2014**, *118* (30), 16386–16392.

(79) Kim, J.; Minegishi, T.; Kobota, J.; Domen, K. Investigation of Cu-Deficient Copper Gallium Selenide Thin Film aS a Photocathode for Photoelectrochemical Water Splitting. *Jpn. J. Appl. Phys.* **2012**, *51* (1).

(80) Kim, J.; Minegishi, T.; Kobota, J.; Domen, K. Enhanced Photoelectrochemical Properties of CuGa3Se5 Thin Films for Water Splitting by the Hydrogen Mediated Co-Evaporation Method. *Energy Environ. Sci.* **2012**, *5* (4), 6368–6374.

(81) Li, M.; Zhao, R.; Su, Y.; Hu, J.; Yang, Z.; Zhang, Y. Synthesis of CuInS2nanowire Arrays via Solution Transformation of Cu2S Self-Template for Enhanced Photoelectrochemical Performance. *Appl. Catal. B Environ.* **2017**, *203*, 715–724.

(82) Sheng, X.; Wang, L.; Chang, L.; Luo, Y.; Zhang, H.; Wang, J.; Yang, D.

Growth and Photoelectrochemical Properties of Ordered CuInS 2 Nanorod Arrays. *Chem. Commun.* **2012**, *48* (39), 4746–4748.

(83) Siemer, K.; Klaer, J.; Luck, I.; Bruns, K.; Klenk, R.; Bra, D. Efficient CuInS Solar Cells from a Rapid Thermal Process (RTP). *Sol. Energy Mater. Sol. Cells* **2001**, *67*, 159–166.

(84) Lee, S. M.; Ikeda, S.; Yagi, T.; Harada, T. Fabrication of CuInS 2 Films from Electrodeposited Cu / In Bilayers : Effects of Preheat Treatment on Their Structural , Photoelectrochemical and Solar Cell Properties. *Phys. Chem. Chem. Phys.* **2011**, *13*, 6662–6669.

(85) Zhao, J.; Minegishi, T.; Zhang, L.; Zhong, M.; Nakabayashi, M.; Ma, G.; Hisatomi, T.; Katayama, M.; Ikeda, S.; Shibata, N.; Yamada, T.; Domen, K. Enhancement of Solar Hydrogen Evolution from Water by Surface Modification with CdS and TiO 2 on Porous CuInS 2 Photocathodes Prepared by an Electrodeposition – Sulfurization Method. *Angew. Chemie Int. Ed.* **2014**, *53*, 11808–11812.

(86) Huang, Q.; Li, Q.; Xiao, X. Hydrogen Evolution from Pt Nanoparticles Covered P-Type CdS:Cu Photocathode in Scavenger-Free Electrolyte. *J. Phys. Chem. C* **2014**, *118* (5), 2306–2311.

(87) Mathew, X.; Bansal, A.; Turner, J. A.; Dhere, R.; Mathews, N. R.; Sebastian, P. J. Photoelectrochemical Characterization of Surface Modified CdTe for Hydrogen Production. *J. New Mater. Electrochem. Syst.* **2002**, *5* (2), 149–154.

(88) Dominey, R. N.; Lewis, N. S.; Bruce, J. A.; Bookbinder, D. C.; Wrighton,

M. S. Improvement of Photoelectrochemical Hydrogen Generation by Surface Modification of P-Type Silicon Semiconductor Photocathodes. *J. Am. Chem. Soc.* **1982**, *104* (2), 467–482.

(89) Oh, J.; Deutsch, T. G.; Yuan, H.-C.; Branz, H. M. Nanoporous Black Silicon Photocathode for H2 Production by Photoelectrochemical Water Splitting. *Energy Environ. Sci.* **2011**, *4* (5), 1690.

(90) Maier, C. U.; Specht, M.; Bilger, G. Hydrogen Evolution on Platinum-Coated p-Silicon Photocathodes. *Int. J. Hydrogen Energy* **1996**, *21* (10), 859–864.

(91) Scanlon, D. O.; Dunnill, C. W.; Buckeridge, J.; Shevlin, S. A.; Logsdail, A. J.; Woodley, S. M.; Catlow, C. R. A.; Powell, M. J.; Palgrave, R. G.; Parkin, I. P.; Watson, G. W.; Keal, T. W.; Sherwood, P.; Walsh, A.; Sokol, A. A. Band Alignment of Rutile and Anatase TiO2. *Nat. Mater.* **2013**, *12* (9), 798–801.

(92) Yu, J. C.; Ho, W.; Yu, J.; Yip, H.; Po, K. W.; Zhao, J. Efficient Visible-Light-Induced Photocatalytic Disinfection on Sulfur-Doped Nanocrystalline Titania. *Environ. Sci. Technol.* **2005**, *39* (4), 1175–1179.

(93) Park, J. H.; Kim, S.; Bard, A. J. Novel Carbon-Doped TiO 2 Nanotube Arrays with High Aspect Ratios for Efficient Solar Water Splitting. *Nano Lett.* **2006**, *6* (1), 24–28.

(94) Sathish, M.; Viswanathan, B.; Viswanath, R. P.; Gopinath, C. S. Synthesis, Characterization, Electronic Structure, and Photocatalytic Activity of Nitrogen-Doped TiO2 Nanocatalyst. *Chem. Mater.* **2005**, *17*

(25), 6349–6353.

(95) Pu, Y. C.; Wang, G.; Chang, K. Der; Ling, Y.; Lin, Y. K.; Fitzmorris, B. C.; Liu, C. M.; Lu, X.; Tong, Y.; Zhang, J. Z.; Hsu, Y. J.; Li, Y. Au Nanostructure-Decorated TiO2 Nanowires Exhibiting Photoactivity across Entire UV-Visible Region for Photoelectrochemical Water Splitting. *Nano Lett.* **2013**, *13* (8), 3817–3823.

(96) Yu, J.; Qi, L.; Jaroniec, M. Hydrogen Production by Photocatalytic Water Splitting over Pt/TiO 2 Nanosheets with Exposed (001) Facets. *J. Phys. Chem. C* **2010**, *114* (30), 13118–13125.

(97) Liu, E.; Kang, L.; Yang, Y.; Sun, T.; Hu, X.; Zhu, C.; Liu, H.; Wang, Q.; Li, X.; Fan, J. Plasmonic Ag Deposited TiO2nano-Sheet Film for Enhanced Photocatalytic Hydrogen Production by Water Splitting. *Nanotechnology* **2014**, *25* (16).

(98) Le, T. T.; Akhtar, M. S.; Park, D. M.; Lee, J. C.; Yang, O. B. Water Splitting on Rhodamine-B Dye Sensitized Co-Doped TiO2catalyst under Visible Light. *Appl. Catal. B Environ.* **2012**, *111–112*, 397–401.

(99) Hu, Y.; Kleiman-shwarsctein, A.; Forman, A. J.; Hazen, D.; Park, J.; Mcfarland, E. W.; Barbara, S.; Barbara, S. Pt-Doped r-Fe2O3 Thin Films Active for Photoelectrochemical Water Splitting. *Chem. Mater.* **2008**, *20*, 3803–3805.

(100) Thimsen, E.; Le Formal, F.; Gr??tzel, M.; Warren, S. C. Influence of Plasmonic Au Nanoparticles on the Photoactivity of Fe 2O3 Electrodes for Water Splitting. *Nano Lett.* **2011**, *11* (1), 35–43.

(101) Chai, X.; Zhang, H.; Pan, Q.; Bian, J.; Chen, Z.; Cheng, C. 3D Ordered Urchin-like TiO2@Fe2O3 Arrays Photoanode for Efficient Photoelectrochemical Water Splitting. *Appl. Surf. Sci.* **2019**, *470* (November 2018), 668–676.

(102) Jansi Rani, B.; Ravi, G.; Yuvakkumar, R.; Ravichandran, S.; Ameen, F.; AlNadhary, S. Sn Doped α-Fe2O3 (Sn=0,10,20,30 wt%) Photoanodes for Photoelectrochemical Water Splitting Applications. *Renew. Energy* **2019**, *133*, 566–574.

(103) Chang, H. W.; Fu, Y.; Lee, W. Y.; Lu, Y. R.; Huang, Y. C.; Chen, J. L.; Chen, C. L.; Chou, W. C.; Chen, J. M.; Lee, J. F.; Shen, S.; Dong, C. L. Visible Light-Induced Electronic Structure Modulation of Nb- and Ta-Doped α-Fe2O3nanorods for Effective Photoelectrochemical Water Splitting. *Nanotechnology* **2018**, *29* (6).

(104) Sivula, K.; Le Formal, F.; Grätzel, M. Solar Water Splitting: Progress Using Hematite (α-Fe 2O3) Photoelectrodes. *ChemSusChem* **2011**, *4* (4), 432–449.

(105) Kim, J. Y.; Magesh, G.; Youn, D. H.; Jang, J. W.; Kubota, J.; Domen, K.; Lee, J. S. Single-Crystalline, Wormlike Hematite Photoanodes for Efficient Solar Water Splitting. *Sci. Rep.* **2013**, *3*, 1–8.

(106) Bedoya-Lora, F. E.; Hankin, A.; Holmes-Gentle, I.; Regoutz, A.; Nania, M.; Payne, D. J.; Cabral, J. T.; Kelsall, G. H. Effects of Low Temperature Annealing on the Photo-Electrochemical Performance of Tin-Doped Hematite Photo-Anodes. *Electrochim. Acta* **2017**, *251*, 1–11.

(107) Wang, Z. L. Zinc Oxide Nanostructures: Growth, Properties and Applications. *J. Phys. Condens. Matter* **2004**, *16* (25).

(108) Look, D. C.; Reynolds, D. C.; Sizelove, J. R.; Jones, R. L.; Litton, C. W.; Cantwell, G.; Harsch, W. C. Electrical Properties of Bulk ZnO. *Solid State Commun.* **1998**, *105* (6), 399–401.

(109) Look, D. C.; Reynolds, D. C.; Litton, C. W.; Jones, R. L.; Eason, D. B.; Cantwell, G. Characterization of Homoepitaxial P-Type ZnO Grown by Molecular Beam Epitaxy. *Appl. Phys. Lett.* **2002**, *81* (10), 1830–1832.

(110) Liu, M.; Nam, C. Y.; Black, C. T.; Kamcev, J.; Zhang, L. Enhancing Water Splitting Activity and Chemical Stability of Zinc Oxide Nanowire Photoanodes with Ultrathin Titania Shells. *J. Phys. Chem. C* **2013**, *117* (26), 13396–13402.

(111) Frank, S. N.; Bard, A. J. Heterogeneous Photocatalytic Oxidation of Cyanide and Sulfite in Aqueous Solutions at Semiconductor Powders. *J. Phys. Chem.* **1977**, *81* (15), 1484–1488.

(112) Liu, X.; Wang, F.; Wang, Q. Nanostructure-Based WO3 Photoanodes for Photoelectrochemical Water Splitting. *Phys. Chem. Chem. Phys.* **2012**, *14* (22), 7894–7911.

(113) Cheng, X. F.; Leng, W. H.; Liu, D. P.; Zhang, J. Q.; Cao, C. N. Enhanced Photoelectrocatalytic Performance of Zn-Doped WO3 Photocatalysts for Nitrite Ions Degradation under Visible Light. *Chemosphere* **2007**, *68* (10), 1976–1984.

(114) Kalanur, S. S.; Yoo, I. H.; Seo, H. Fundamental Investigation of Ti Doped WO3 Photoanode and Their Influence on Photoelectrochemical Water Splitting Activity. *Electrochim. Acta* **2017**, *254*, 348–357.

(115) Nah, Y. C.; Paramasivam, I.; Hahn, R.; Shrestha, N. K.; Schmuki, P. Nitrogen Doping of Nanoporous WO3 Layers by NH3 Treatment for Increased Visible Light Photoresponse. *Nanotechnology* **2010**, *21* (10).

(116) Liew, S. L.; Zhang, Z.; Goh, T. W. G.; Subramanian, G. S.; Seng, H. L. D.; Hor, T. S. A.; Luo, H. K.; Chi, D. Z. Yb-Doped WO3 Photocatalysts for Water Oxidation with Visible Light. *Int. J. Hydrogen Energy* **2014**, *39* (9), 4291–4298.

(117) Fan, W.; Li, M.; Bai, H.; Xu, D.; Chen, C.; Li, C.; Ge, Y.; Shi, W. Fabrication of MgFe2O4/MoS2 Heterostructure Nanowires for Photoelectrochemical Catalysis. *Langmuir* **2016**, *32* (6), 1629–1636.

(118) Ain, N. ul; Shaheen, W.; Bashir, B.; Abdelsalam, N. M.; Warsi, M. F.; Khan, M. A.; Shahid, M. Electrical, Magnetic and Photoelectrochemical Activity of RGO/MgFe2O4nanocomposites under Visible Light Irradiation. *Ceram. Int.* **2016**, *42* (10), 12401–12408.

(119) Li, M.; Bai, H. Y.; Da, Z. L.; Yan, X.; Chen, C.; Jiang, J. H.; Fan, W. Q.; Shi, W. D. Electrospinning Synthesis and Photocatalytic Property of CaFe2O4/MgFe2O4 Heterostructure for Degradation of Tetracycline. *Cryst. Res. Technol.* **2015**, *50* (3), 244–249.

(120) Wang, M.; Sun, Y.; Chen, H.; Zhang, Y.; Wu, X.; Huang, K.; Feng, S. Enhanced Photoelectrochemical Activity of Nanostructured ZnFe $_2$ O $_4$

Thin Films Prepared by the Electrospray Technique. *CrystEngComm* **2017**, *19* (5), 772–775.

(121) Tahir, A. A.; Wijayantha, K. G. U. Photoelectrochemical Water Splitting at Nanostructured ZnFe2O4 Electrodes. *J. Photochem. Photobiol. A Chem.* **2010**, *216* (2–3), 119–125.

(122) Hufnagel, A. G.; Peters, K.; Müller, A.; Scheu, C.; Fattakhova-Rohlfing, D.; Bein, T. Zinc Ferrite Photoanode Nanomorphologies with Favorable Kinetics for Water-Splitting. *Adv. Funct. Mater.* **2016**, *26* (25), 4435–4443.

(123) Guo, Y.; Zhang, N.; Wang, X.; Qian, Q.; Zhang, S.; Li, Z.; Zou, Z. A Facile Spray Pyrolysis Method to Prepare Ti-Doped ZnFe $_2$ O $_4$ for Boosting Photoelectrochemical Water Splitting. *J. Mater. Chem. A* **2017**, *5* (16), 7571–7577.

(124) Zhu, X.; Guijarro, N.; Liu, Y.; Schouwink, P.; Wells, R. A.; Le Formal, F.; Sun, S.; Gao, C.; Sivula, K. Spinel Structural Disorder Influences Solar-Water-Splitting Performance of ZnFe 2 O 4 Nanorod Photoanodes. *Adv. Mater.* **2018**, *30*, 1801612.

(125) Lamers, M.; Fiechter, S.; Friedrich, D.; Abdi, F. F.; Van De Krol, R. Formation and Suppression of Defects during Heat Treatment of BiVO4 Photoanodes for Solar Water Splitting. *J. Mater. Chem. A* **2018**, *6* (38), 18694–18700.

(126) Lee, D. K.; Choi, K. S. Enhancing Long-Term Photostability of BiVO4 Photoanodes for Solar Water Splitting by Tuning Electrolyte

Composition. *Nat. Energy* **2018**, *3* (1), 53–60.

(127) Wang, S.; Chen, P.; Bai, Y.; Yun, J. H.; Liu, G.; Wang, L. New BiVO4 Dual Photoanodes with Enriched Oxygen Vacancies for Efficient Solar-Driven Water Splitting. *Adv. Mater.* **2018**, *30* (20), 1–7.

(128) Jeong, S. Y.; Shin, H. M.; Jo, Y. R.; Kim, Y. J.; Kim, S.; Lee, W. J.; Lee, G. J.; Song, J.; Moon, B. J.; Seo, S.; An, H.; Lee, S. H.; Song, Y. M.; Kim, B. J.; Yoon, M. H.; Lee, S. Plasmonic Silver Nanoparticle-Impregnated Nanocomposite BiVO4 Photoanode for Plasmon-Enhanced Photocatalytic Water Splitting. *J. Phys. Chem. C* **2018**, *122* (13), 7088–7093.

(129) Bhat, S. S. M.; Suh, J. M.; Choi, S.; Hong, S. P.; Lee, S. A.; Kim, C.; Moon, C. W.; Lee, M. G.; Jang, H. W. Substantially Enhanced Front Illumination Photocurrent in Porous SnO2 Nanorods/Networked BiVO4 Heterojunction Photoanodes. *J. Mater. Chem. A* **2018**, *6* (30), 14633–14643.

(130) Gujral, S. S.; Simonov, A. N.; Higashi, M.; Abe, R.; Spiccia, L. Optimization of Titania Post-Necking Treatment of TaON Photoanodes to Enhance Water-Oxidation Activity under Visible-Light Irradiation. *ChemElectroChem* **2015**, *2* (9), 1270–1278.

(131) Zhang, P.; Zhang, J.; Gong, J. Tantalum-Based Semiconductors for Solar Water Splitting. *Chem. Soc. Rev.* **2014**, *43*, 4395–4422.

(132) Hara, M.; Nunoshige, J.; Takata, T.; Kondo, J. N.; Domen, K. Unusual Enhancement of H2 Evolution by Ru on TaON Photocatalyst under

Visible Light Irradiation. *Chem. Commun.* **2003**, *3* (24), 3000–3001.

(133) Yokoyama, D.; Hashiguchi, H.; Maeda, K.; Minegishi, T.; Takata, T.; Abe, R.; Kubota, J.; Domen, K. Ta3N5 Photoanodes for Water Splitting Prepared by Sputtering. *Thin Solid Films* **2011**, *519* (7), 2087–2092.

(134) Ishikawa, A.; Takata, T.; Kondo, J. N.; Hara, M.; Domen, K. Electrochemical Behavior of Thin Ta3N5 Semiconductor Film. *J. Phys. Chem. B* **2004**, *108* (30), 11049–11053.

(135) Pinaud, B. A.; Vesborg, P. C. K.; Jaramillo, T. F. Effect of Film Morphology and Thickness on Charge Transport in Ta3N5/Ta Photoanodes for Solar Water Splitting. *J. Phys. Chem. C* **2012**, *116* (30), 15918–15924.

(136) Li, Y.; Takata, T.; Cha, D.; Takanabe, K.; Minegishi, T.; Kubota, J.; Domen, K. Vertically Aligned Ta3N5 Nanorod Arrays for Solar-Driven Photoelectrochemical Water Splitting. *Adv. Mater.* **2013**, *25* (1), 125–131.

(137) Tahir, A. A.; Mat-Teridi, M. A.; Wijayantha, K. G. U. Photoelectrochemical Properties of Texture-Controlled Nanostructured ??-Fe2O3 Thin Films Prepared by AACVD. *Phys. Status Solidi - Rapid Res. Lett.* **2014**, *8* (12), 976–981.

(138) Srivastava, M.; Chaubey, S.; Ojha, A. K. Investigation on Size Dependent Structural and Magnetic Behavior of Nickel Ferrite Nanoparticles Prepared by Sol-Gel and Hydrothermal Methods. *Mater. Chem. Phys.* **2009**, *118* (1), 174–180.

(139) Phumying, S.; Labuayai, S.; Swatsitang, E.; Amornkitbamrung, V.; Maensiri, S. Nanocrystalline Spinel Ferrite (MFe2O4, M = Ni, Co, Mn, Mg, Zn) Powders Prepared by a Simple Aloe Vera Plant-Extracted Solution Hydrothermal Route. *Mater. Res. Bull.* **2013**, *48* (6), 2060–2065.

(140) Joshi, S.; Nawathey, R.; Koinkar, V. N.; Godbole, V. P.; Chaudhari, S. M.; Ogale, S. B.; Date, S. K. Pulsed Laser Deposition of Iron Oxide and Ferrite Films. *J. Appl. Phys.* **1988**, *64* (10), 5647–5649.

(141) Li, S. Z.; Liu, J.; Wang, X. Z.; Yan, B. W.; Li, H.; Liu, J. M. Epitaxial Growth of Delafossite CuFeO2thin Films by Pulse Laser Deposition. *Phys. B Condens. Matter* **2012**, *407* (13), 2412–2415.

(142) Peng, Q.; Wang, J.; Feng, Z.; Du, C.; Wen, Y.; Shan, B.; Chen, R. Enhanced Photoelectrochemical Water Oxidation by Fabrication of P-LaFeO $_3$ /n-Fe $_2$ O $_3$ Heterojunction on Hematite Nanorods. *J. Phys. Chem. C* **2017**, *121* (24), 12991–12998.

(143) Sathaye, S. D.; Patil, K. R.; Kulkarni, S. D.; Bakre, P. P.; Pradhan, S. D.; Sarwade, B. D.; Shintre, S. N. Modification of Spin Coating Method and Its Application to Grow Thin Films of Cobalt Ferrite. *J. Mater. Sci.* **2003**, *38* (1), 29–33.

(144) Bera, A.; Deb, K.; Sinthika, S.; Thapa, R.; Saha, B. Chemical Modulation of Valance Band in Delafossite Structured CuFeO2 Thin Film and Its Photoresponse. *Mater. Res. Express* **2018**, *5* (1).

(145) Pawar, G. S.; Elikkottil, A.; Seetha, S.; Reddy, S.; Pesala, B.; Tahir, A.

A.; Mallick, T. K. Enhanced Photoactivity and Hydrogen Generation of LaFeO 3 Photocathode by Plasmonic Silver Nanoparticle Incorporation. *ACS Appl. Energy Mater.* **2018**, *1* (7), 3449–3456.

(146) Wu, Z.; Okuya, M.; Kaneko, S. Spray Pyrolysis Deposition of Zinc Ferrite Films from Metal Nitrates Solutions. *Thin Solid Films* **2001**, *385* (1–2), 109–114.

(147) Scheffe, J. R.; Allendorf, M. D.; Coker, E. N.; Jacobs, B. W.; McDaniel, A. H.; Weimer, A. W. Hydrogen Production via Chemical Looping Redox Cycles Using Atomic Layer Deposition-Synthesized Iron Oxide and Cobalt Ferrites. *Chem. Mater.* **2011**, *23* (8), 2030–2038.

(148) Barnabé, A.; Mugnier, E.; Presmanes, L.; Tailhades, P. Preparation of Delafossite CuFeO2 Thin Films by Rf-Sputtering on Conventional Glass Substrate. *Mater. Lett.* **2006**, *60* (29–30), 3468–3470.

(149) Spray, R. L.; Choi, K. S. Photoactivity of Transparent Nanocrystalline Fe2O3 Electrodes Prepared via Anodic Electrodeposition. *Chem. Mater.* **2009**, *21* (15), 3701–3709.

(150) Hall, D. B.; Underhill, P.; Torkelson, J. M. Spin Coating of Thin and Ultrathin Polymer Films. *Polym. Eng. Sci.* **1998**, *38* (12), 2039–2045.

(151) Leskelä, M.; Ritala, M. Atomic Layer Deposition Chemistry: Recent Developments and Future Challenges. *Angew. Chemie - Int. Ed.* **2003**, *42* (45), 5548–5554.

(152) Kelly, P. . J.; Arnell, R. . D. Magnetron Sputtering: A Review of Recent

Developments and Applications. *Vacuum* **2000**, *56* (3), 159–172.

(153) Corni, I.; Ryan, M. P.; Boccaccini, A. R. Electrophoretic Deposition: From Traditional Ceramics to Nanotechnology. *J. Eur. Ceram. Soc.* **2008**, *28* (7), 1353–1367.

(154) Marchand, P.; Hassan, I. A.; Parkin, I. P.; Carmalt, C. J. Aerosol-Assisted Delivery of Precursors for Chemical Vapour Deposition: Expanding the Scope of CVD for Materials Fabrication. *Dalt. Trans.* **2013**, *42* (26), 9406–9422.

(155) Kolodziejczak-Radzimska, A.; Jesionowski, T. Zinc Oxide-from Synthesis to Application: A Review. *Materials (Basel).* **2014**, *7* (4), 2833–2881.

(156) Brinker, C. J.; Frye, G. C.; Hurd, A. J.; Ashley, C. S.; Laboratories, S. N.; Introduction, I. Fundamentals of Sol-Gel Dip Coating. *Thin Solid Films* **1991**, *201*, 97–108.

(157) Willmott, P. R.; Huber, J. R. Pulsed Laser Vaporization and Deposition. *Rev. Mod. Phys.* **2000**, *72* (1), 315–328.

(158) Patil, P. S. Versatility of Chemical Spray Pyrolysis Technique. *Mater. Chem. Phys.* **1999**, *59* (3), 185–198.

Chapter 3: Characterisation Techniques

In this chapter the main techniques used to characterise the synthesised materials will be briefly described in order to provide a theoretical background.

3.1 X-Ray Diffraction

X-Ray Diffraction (XRD) method is the most essential and effective method for determining the crystal structure of materials, it allows us to determine the atomic structure of a crystalline material.[1,2] The material will have a crystal lattice structure which is layered and ordered where a “unit cell” is periodically repeated in three dimension. When an X-ray photon travels through the sample matter it interacts with the electron density surrounding the atomic nuclei resulting to a coherent scattering (also known as Rayleigh scattering). Some of the X-ray photons will be diffracted upon hitting the first plane of atoms, while others will travel further and are diffracted by the second plane, and so on. By comparing the X-ray which is diffracted by the first and second plane, the latter will have travelled a longer distance, shown as green lines AB and BC in figure 26. This results in a constructive interference, where the incoming X-ray forms an angle θ with the crystal plane and will be diffracted with the same angle, leaving the lattice in the same phase where the waves stack producing a wave with higher amplitude.

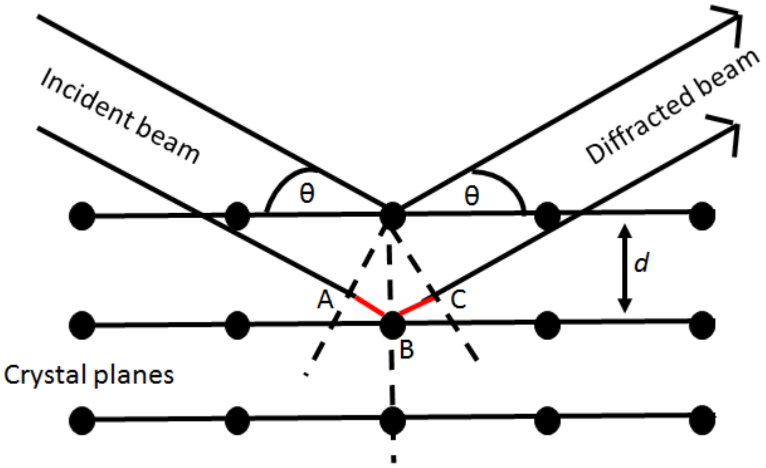

Figure 26: Representation of two X-ray being diffracted by the first and second layer in a crystal lattice. The red lines show the extra distance travelled by the X-ray in the second layer compared to the first layer.

The relationship between the wavelengths of the incident X-rays, angle of incidence and distance between the lattice planes is described by Bragg's Law in equation 9:

$$n\lambda = 2d\sin(\theta) \qquad \textbf{(eq. 8)}$$

Where n is the order of diffraction, λ is the wavelength of the incident beam in nm, d is the lattice spacing in nm and θ is the angle of the diffracted beam. If the Bragg's law is not obeyed the individual diffracted X-ray's will be out of phase and cancel each other out resulting in a destructive interference.

The main application of XRD is to identify and quantify the materials phase and compounds by search and match procedures available in extensive databases. Each material will produce a pattern unique to others so identification is easy. This technique was used to help determine that the correct single phase material we was targeting was made.

3.2 Scanning Electron Microscope/ Energy-dispersive X-Ray Spectroscopy

Scanning electron microscope (SEM) is a technique which uses a focused high-energy beam of electrons to obtain high resolution images of the materials surface by rapidly scanning its surface. A beam is generated of highly energetic electrons that behave as waves of lower wavelength than that of visible light, as our eyes cannot detect photons below 400 nm wavelength. The electrons wavelength depends on their speed and the accelerating voltage applied to it. As a result most SEMs can go down to a resolution of 10 nm compared to optical microscope which are limited to 200 nm.[3]

The working principles of an SEM is as follows: a beam of electrons from a source, either from a thermoionic, Schottky or a field emission cathode, are generated and are accelerated through a voltage difference through a anode and cathode between the ranges of 0.1 – 50 keV. Magnetic fields, or “lenses”, are employed to focus the electron beam, resulting in the electrons to converge to form a highly focused beam. This all occurs in a vacuum chamber to avoid the electrons interacting with air particles. When the electron beam interacts with the sample it produces emissions which are captured by detectors placed in appropriate positions and form an image on a computer screen.[4,5] Figure 27 shows the diagram for the SEM.

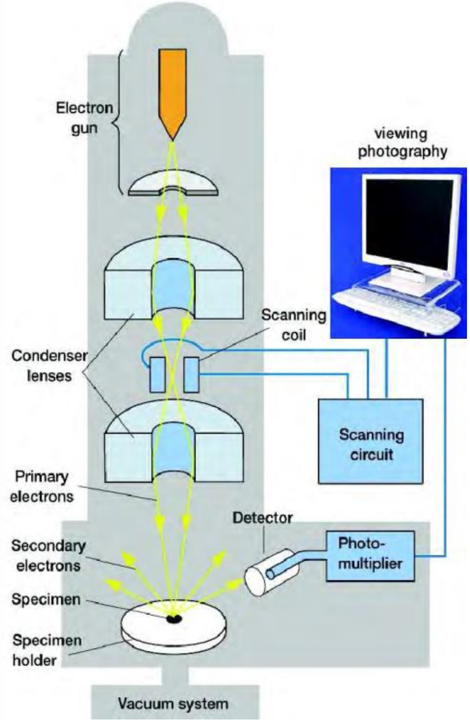

Figure 27: Schematic diagram of the scanning electron microscope.

SEM is usually accompanied by an energy-dispersive X-ray spectroscopy (EDX), allowing the user to determine the elemental composition of the features in SEM image. This is done by properly positioning an X-ray detector allowing it to intercept emitted X-rays from the sample. When these X-rays are detected it generates a small current that is converted to a voltage, where the size is proportional to the X-rays frequency. This feature allows the user select specific features in the live image to obtain the elemental composition. This technique was used to determine the fabricated materials morphology and particle size.

3.3 Raman Spectroscopy

Raman spectroscopy is a scattering technique which is based on the Raman Effect, where frequency of small fraction of scattered radiation is different from frequency of monochromatic incident radiation. This technique probes the molecular vibrations.

In Raman spectroscopy the sample is illuminated with a monochromatic laser beam which then interacts with the samples molecules and scatters the light. The scattered light has a frequency different than that of the incident light (inelastic scattering) and is used to construct a Raman spectrum. The Raman spectra arises due to inelastic collision between incident monochromatic radiation and sample molecules. When the monochromatic light hits the sample, it scatters in all directions. Most of the scattered radiation has a frequency equal to the frequency of incident radiation (Rayleighs scattering). Only a small fraction of the scattered radiation has a frequency different to the incident radiation and constitutes Raman scattering. If the frequency of incident radiation is higher than the frequency of the scattered radiation, Stokes lines appear in the Raman spectrum. However, if the frequency of the incident radiation is lower than the frequency of the scattered radiation, anti-Stokes lines appear in the Raman spectrum.[6,7] Figure 28 shows the schematic of a Raman spectra. A Raman spectra can provide information on the materials such as chemical structure, phase, contamination and impurities. This technique was used to determine the materials structural fingerprint.

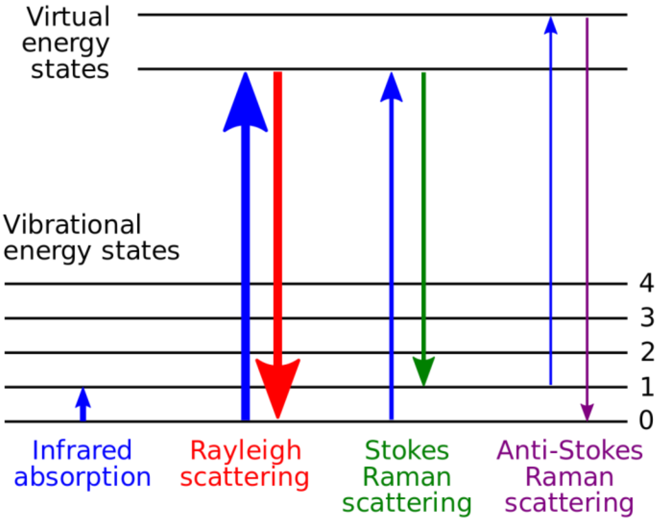

Figure 28: Energy level diagram for Raman, Rayleigh, Stokes and anti-Stokes scattering.

3.4 Ultraviolet – Visible Spectroscopy

Ultraviolet-Visible (UV-Vis) spectroscopy is a popular analytical technique which uses the ultraviolet and visible part of the light spectrum to determine at what wavelength that material (in our case a semiconductor) absorbs light. This provides useful information allowing us to know if the material is visible light active or only ultraviolet active. When the beam of light passes through the sample, the energy from the light promotes an electron from bonding or non-bonding orbital to an anti-bonding orbital. When the energy matches the energy difference between an electronic transition, a part of the lights wavelength is absorbed allowing the promotion of the electron to a higher energy state.[8] The absorption at different wavelengths from the sample is recorded resulting in a plot of absorbance (A) versus wavelength (λ). Figure 29 shows the diagram of a typical UV-Vis spectrometer. This technique was used to help determine the materials bandgap and to compare the absorption amount of the varying concentrations of $LaFeO_3$-Ag and $LaFeO_3$-Ni, to help determine which level of concentration of metal gave best performance.

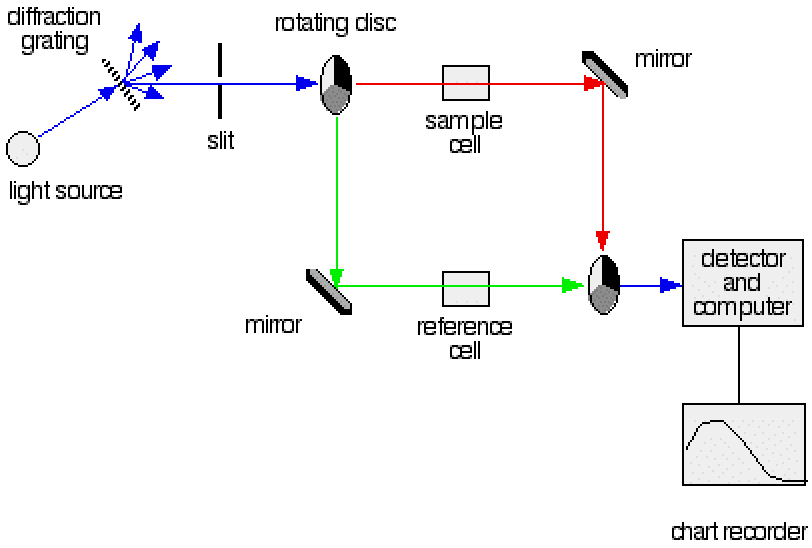

Figure 29: Schematic diagram of a UV-Vis spectrophotometer.

Reference

(1) Leng, Y. *MATERIALS CHARACTERIZATION Introduction to Microscopic and Spectroscopic Methods*; 2010.

(2) Epp, J. *X-Ray Diffraction (XRD) Techniques for Materials Characterization*; Elsevier Ltd, 2016.

(3) Electron microscope tutorial https://advanced-microscopy.utah.edu/education/electron-micro/index.html (accessed Nov 13, 2018).

(4) Suga, M.; Asahina, S.; Sakuda, Y.; Kazumori, H.; Nishiyama, H.; Nokuo, T.; Alfredsson, V.; Kjellman, T.; Stevens, S. M.; Cho, H. S.; Cho, M.; Han, L.; Che, S.; Anderson, M. W.; Schüth, F.; Deng, H.; Yaghi, O. M.; Liu, Z.; Jeong, H. Y.; Stein, A.; Sakamoto, K.; Ryoo, R.; Terasaki, O. Recent Progress in Scanning Electron Microscopy for the Characterization of Fine Structural Details of Nano Materials. *Prog. Solid State Chem.* **2014**, *42* (1–2), 1–21.

(5) Reimer, L. *Scanning Electron Microscopy Physics of Image Formation and Microanalysis*, 2nd ed.; Hawkes, P. W., Ed.; Springer, 1998; Vol. 45.

(6) Das, R. S.; Agrawal, Y. K. Raman Spectroscopy: Recent Advancements, Techniques and Applications. *Vib. Spectrosc.* **2011**, *57* (2), 163–176.

(7) Bumbrah, G. S.; Sharma, R. M. Raman Spectroscopy – Basic Principle, Instrumentation and Selected Applications for the Characterization of Drugs of Abuse. *Egypt. J. Forensic Sci.* **2016**, *6*, 209–215.

(8) UV-VISIBLE ABSORPTION SPECTRA

https://www.chemguide.co.uk/analysis/uvvisible/theory.html (accessed Nov 14, 2018).

Chapter 4: Experimental Techniques

In this chapter the experimental techniques used to study the materials performance are discussed. The basic theory behind the various experiments are also discussed.

4.1 Spray Pyrolysis Method

Spray pyrolysis (SP) is a low-cost, scalable and simple technique used for depositing thin films uniformly onto large substrate areas at relatively low-cost for mass production. SP deposition technique has several advantages: 1) provides an easy way to dope films with virtually any element, 2) does not require high quality substrates or require any vacuum at any stage, 3) deposition rate and thickness can be controlled by changing its parameters, and 4) its operating temperatures are moderate (100 – 500ºC).[1]

In this deposition process a precursor solution is pumped via a syringe pump at a set rate. The precursor is passed through a nozzle tip which is turned into an aerosol by an atomizer via ultrasonication. These very fine droplets are then blown through a vortex chamber by a carrier gas where a vortex is generated. This is passed over a substrate which is on a hotplate (at moderate temperatures) where a uniform layer is deposited, as the solvent evaporates. A second annealing step is usually required to form the target crystalline material. The SP set-up consists of the following syringe pump, atomizer, temperature controlled hotplate, precursor solution, vortex and a carrier gas (figure 30)

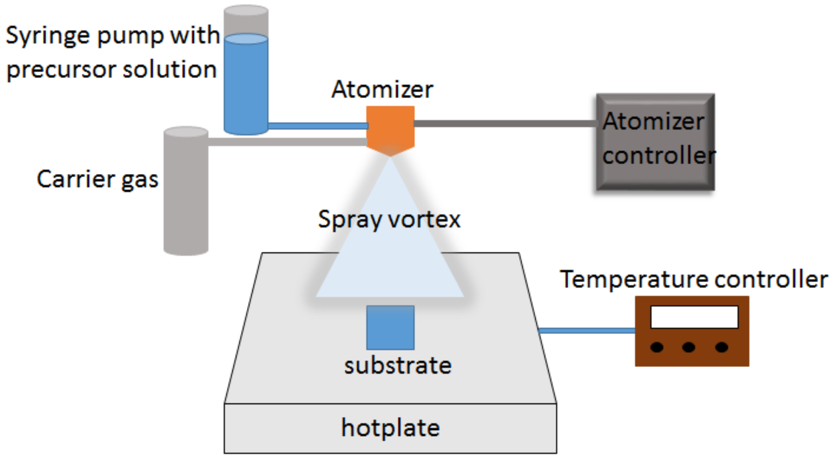

Figure 30: Diagram of spray pyrolysis system.

4.2 Spin Coating Method

Spin coating is a low-cost, simple batch process in which a liquid film is spread by centrifugal force onto a rotating substrate. This method spins low viscosity liquid to thickness of from few microns down to a few nanometres. Solvent evaporation is greatly enhanced by the air flow induced by the high spinning speeds, therefore the application, coating and drying of the film can be accomplished all together less than a minute.[2] However, if further solvent evaporation is required then heating on a hotplate at the solvents boiling point can be done. A vacuum pump attachment is used to hold the substrate in place during the spinning process. The films produced are highly uniform and the thickness can be controlled by altering the spin coater's parameters, such as spin time and spin speed. Also, multiple layers can be added by repeating the process more than once to achieve the desired thickness. Figure 31 shows the diagram of a spin coater.

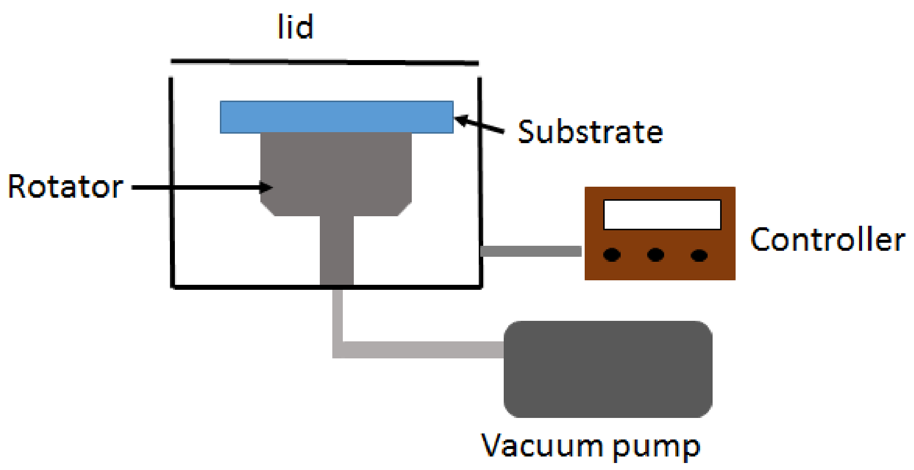

Figure 31: Diagram of a spin coater.

4.3 Sol-Gel Method

“Sols” are dispersions of colloidal particles in a liquid and “gel” is an interconnected, rigid network with pores less than a micrometre and polymeric chains whose average length is greater than a micrometre.[3] Typically inorganic metal salts or metal organic compounds are used as precursors.

Sol-gel fabrication technique is a common and well used method of fabricating high purity materials as powders, fibres, monoliths, thin film coatings and self-supporting bulk structures. Three dimensional network structures can be developed in the form of a gel, through controlled hydrolysis and polycondensation reactions of precursors. Subsequent drying and calcination steps may results in an oxide structure. Through sol-gel process the homogeneity, purity and microstructure of a material can be controlled. The ability of shaping the material in different forms is considered an advantage of the sol-gel process.[4]

4.4 Gas Chromatography

Gas chromatography (GC) is a separation technique used to isolate gas components of a mixture and are separated as a function of their retention time in a liquid or solid stationary phase within a column. GC is made up of four components: injector, column, carrier gas and detector (figure 32). A syringe is used to take a sample from the dead space of an electrochemical cell and inject it into the injection port. An inert gas carrier (argon) carries the sample through the column and the different analytes separate at different times depending on their retention coefficient before arriving at the detector. Our detector is a thermal conductivity detector, which senses the changes in thermal conductivity of separated gases and is compared to a reference flow (which in our case is argon). The detector then sends a signal to the computer which makes a plot as a function of time, where each analyte appears as a peak at a specific time. The time serves to identify the peaks, and the area of peaks are correlated to the percentage of the particular gas in the dead space of electrochemical cell by calibration lines which have been made for each gas using commercially obtained gas cylinders containing specific percentages of the particular gas in argon. These percentages are then converted to number of moles with the known dead space, and then multiplied by the electrodes surface area to determine how much hydrogen is produced per cm^2 area of electrode.

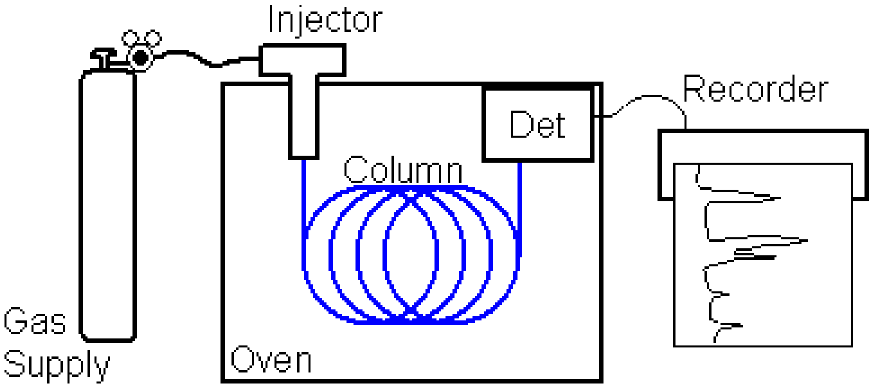

Figure 32: Diagram showing the gas chromatograph.

4.5 Photoelectrochemical Measurements

4.5.1 Linear Sweep Voltammetry

A linear sweep voltammetry (LSV) is a technique used to measure the current of the photoelectrode between a range of potential, typically in a 3 electrode system consisting of a working electrode, reference electrode and a counter electrode. In LSV the potential is linearly swept, either in a forward direction or in the reverse direction, from potential V_1 to a potential V_2 with illumination from a light source. The data is recorded as a current vs potential and is called a voltammogram. Furthermore, during the measurement the light can be chopped at certain intervals to see if the material is photoactive and to see the materials dark current.

4.5.2 Chronoamperometry

Chronoamperometry (CA) is a measurement technique used to investigate the photoelectrodes stability. A constant potential is applied to the working electrode with illumination from a light source. Long term stability measurement is performed under continuous illumination and the data is recorded as current vs time.

4.5.3 Electrochemical Impedance Spectroscopy

Electrochemical impedance spectroscopy (EIS) is a widely used technique to study the kinetic properties and adsorption properties of thin films.[5,6] In principle, impedance is the opposition force to electrical current in a circuit and is measured in the same unit as resistance, ohms (Ω).[7] The EIS method is used to measure the response of an electrode to a sinusoidal potential modulation at different frequencies.[8] It is then measured as a function of frequency at the applied potential and is repeated at various potentials. From EIS measurements a Mott-Schottky plot can be made to estimate the photoelectrodes flat band potential (V_{fb}). As a potential is applied to the working electrode, the potential difference across the electrode/ electrolyte junction increases. Under a depleted condition there are only a few charge carriers at the electrode/ electrolyte interface, while on the other hand under charge accumulation the amount of charge carriers' increase resulting to an increase to the interfacial capacitance. Therefore, the flat band potential can be estimated by measuring and plotting the electrodes capacitance (*C*) as a function of electrode potential (*V*). Equation 9 shows the capacitance as a function of the electrode potential:

$$\frac{1}{C^2} = \frac{2}{\varepsilon\varepsilon^0 A q N_q}\left(-V + V_{fb} + \frac{kT}{q}\right) \qquad \textbf{(eq. 9)}$$

Where ε and ε_0 are the dielectric constant of the passive film and permittivity vacuum respectively, q is the elementary charge ($-e$ for electron and $+e$ for holes), N_q is the doping density (for donor N_d or acceptor N_a densities for an *n*- or *p*-type semiconductor), k is the Boltzmann constant, V_{fb} is the flat band potential, A is the area of electrode. Therefore, a plot of $1/C^2$ against the applied potential V should yield a straight line from which the flat band potential can be determined from the intercept of the X-axis (the potential axis).[8]

Reference

(1) Patil, P. S. Versatility of Chemical Spray Pyrolysis Technique. *Mater. Chem. Phys.* **1999**, *59* (3), 185–198.

(2) Larson, R. G.; Rehg, T. J. Spin Coating; 1997; pp 709–734.

(3) Hench, L. L.; West, J. K. The Sol-Gel Process. *Chem. Rev.* **1990**, *90* (1), 33–72.

(4) Keshmiri, M.; Troczynski, T.; Mohseni, M. Oxidation of Gas Phase Trichloroethylene and Toluene Using Composite Sol-Gel TiO2photocatalytic Coatings. *J. Hazard. Mater.* **2006**, *128* (2–3), 130–137.

(5) Vorotyntsev, M. A.; Badiali, J. P.; Inzelt, G. Electrochemical Impedance Spectroscopy of Thin Films with Two Mobile Charge Carriers: Effects of the Interfacial Charging. *J. Electroanal. Chem.* **1999**, *472* (1), 7–19.

(6) Randviir, E. P.; Banks, C. E. Electrochemical Impedance Spectroscopy: An Overview of Bioanalytical Applications. *Anal. Methods* **2013**, *5* (5), 1098–1115.

(7) Alexander, C. K.; Sadiku, M. N. O. *Fundamentals of Electric Circuits*, 5th ed.; McGraw-Hill, 2006.

(8) Cesiulis, H.; Tsyntsaru, N.; Ramanavicius, A.; Ragoisha, G. *The Study of Thin Films by Electrochemical Impedance Spectroscopy*; 2016.

Chapter 5: Experimental Procedure

In this chapter the following are discussed: 1) materials used in synthesis procedure and 2) the synthesis procedures for making the materials. This chapter also includes the list of equipment's and their details used to carry out this work.

5.1 Materials

All the materials used were purchased from commercial suppliers and used as is when received, unless stated otherwise.

5.1.1 Substrate

Fluorine – doped tin oxide (FTO) glass substrate served as a charge collector for the photogenerated electrons due to its excellent conductive property. FTO is mechanically, chemically and electrochemically stable making it an ideal candidate for application in photoelectrodes.[1,2] The FTO should have very little resistance (ohmic contact) to allow for maximum charge collection/ transportation, to provide the maximum efficiency allowed for the system. The FTO glass substrate used in this work were obtained from NSG Pilkington (TEC 7).

Before the fabrication of photocathodes onto the FTO glass substrate, it is first cut into 3 x 3 cm squares. Thereafter, it undergoes a cleaning process where the FTO glass substrate is ultrasonicated in several solvents (ethanol, iso-propanol, acetone and de-ionized water) for 15 minutes each. Finally, the cleaned substrates are then stored in ethanol until used. Scheme 1 shows the process.

Scheme 1: FTO cleaning procedure with ultrasonication for 15 minutes at each stage.

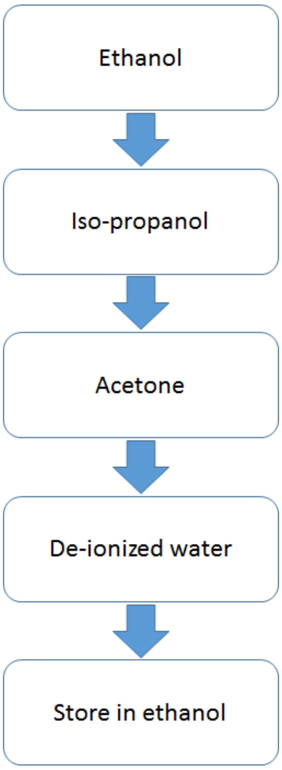

5.1.2 $LaFeO_3$ Solution Preparation

Iron (III) nitrate (>98 %) and trifluoroacetic acid (>99 %) were purchased from Sigma – Aldrich. Lanthanum (III) iso-propoxide (40 % La) was purchased from Alfa Aesar. Ammonium hydroxide solution (35 %) was purchased from Fisher Scientific. Methanol (99.8 %) was purchased from ACROS Organics.

The $LaFeO_3$ (LFO) precursor solution is prepared by first dissolving iron (III) nitrate (1 mmol) in methanol (20 ml), under constant stirring. Once fully dissolved, ammonium hydroxide is added to the solution under vigorous stirring for 15 minutes to form precipitates of iron (III) hydroxide. The precipitates are then collected by centrifuge where it is spun for 5 minutes at a rate of 3600 rpm. The supernatant is decanted off and de-ionized water is added for cleaning process. After shaking vigorously, the precipitate is centrifuged again for 5 minutes at 3600 rpm and the supernatant is decanted off. This cleaning process occurs 2 times. After centrifugation the precipitate is collected and dissolved in trifluoroacetic acid (0.1 ml) and methanol (25 ml). Lanthanum (III) iso-propoxide (0.1 mmol) is added to the solution. The mixture is ultrasonicated until all the lanthanum has dissolved. The LFO solution preparation is shown in scheme 2. This mixture is then ready to be deposited onto the FTO glass substrate.

Scheme 1: Procedure for $LaFeO_3$ solution preparation.

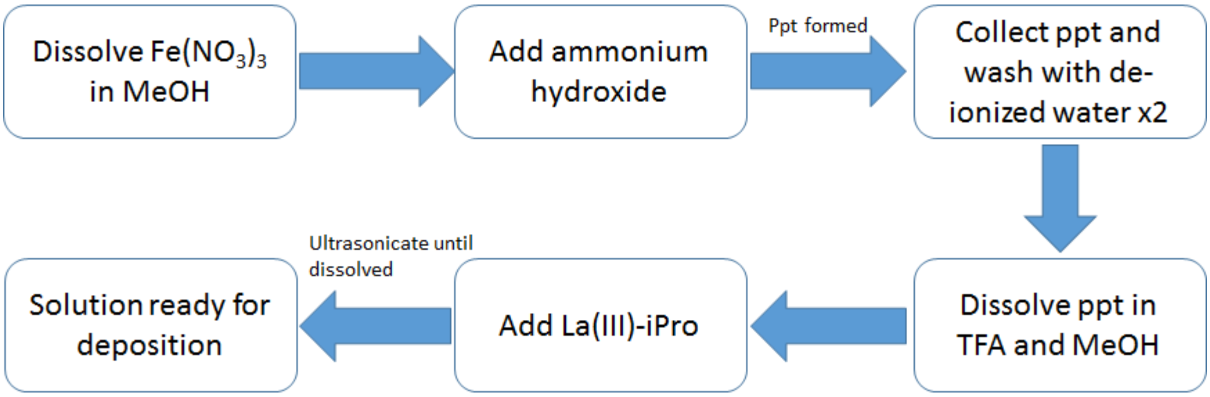

5.1.3 $LaFeO_3$ Photocathode Synthesis by Spray Pyrolysis

The LFO photocathodes were prepared by spray pyrolysis technique.[3] A clean FTO glass substrate is taken and washed with de-ionized water to remove the ethanol and is dried. It was then placed in the centre of the hot plate at 150ºC. The LFO solution is pumped via a syringe to the spray tip. The spray system comprised of a syringe pump system (New Era Pump System NE-1000), an ultrasonic atomizer nozzle (Sonozap) 1 mm diameter and a vortex attachment (figure 33 (a)). 5 ml of the precursor solution was sprayed on to the FTO at a rate of 1 ml min^{-1} assisted with compressed air at a rate of 6 L min^{-1}, which is passed through the vortex attachment to generate a large plume of aerosol to get a uniform coverage on the FTO. After the completion of spray, the films were further annealed in a box furnace (Carbolite AAF 1100) 550^{o}C for 3 hours in air. Once cool the photocathode was ready for testing (figure 33 (b)).

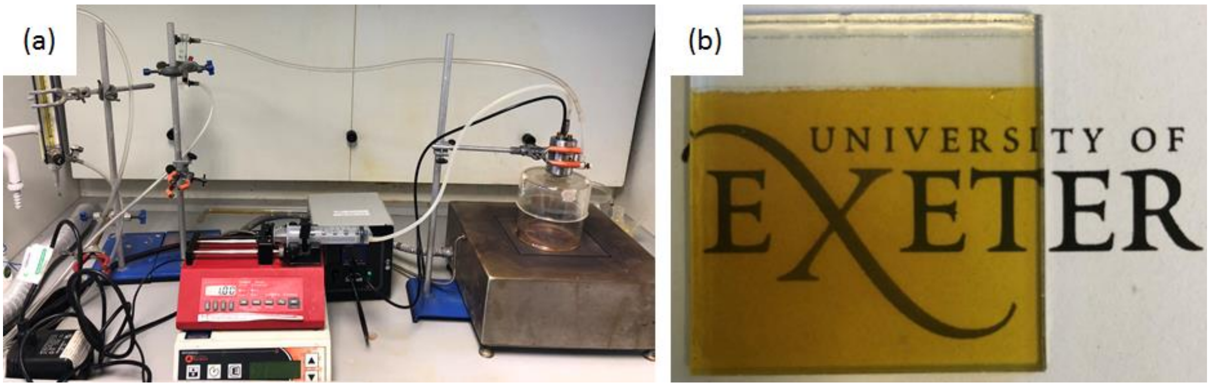

Figure 33: a) Spray pyrolysis set up and **b)** LFO photocathode after second annealing step.

5.1.4 LaFeO$_3$ – Ag and LaFeO$_3$ – Ni Photocathode Synthesis

The silver nanoparticles were obtained from Nanoshel (99.9%), where the particle size was 70nm . The nickel nanoparticles were obtained from Sigma – Aldrich (> 99%), where the particle size was in the range of 60-100 nm.

Firstly, the LFO photocathodes are fabricated the exact same way as in section 2.1.3, via spray pyrolysis, and ready for either silver (Ag) or nickel (Ni) nanoparticle incorporation.

5.1.4.1 Preparation of Silver Nanoparticles

The silver nanopowder (0.77 mmol) is placed into a vial containing acetone (15 ml). Subsequently, it was ultrasonicated for 2 hours to break down large particles and reduce the agglomeration for obtaining a homogeneous suspension of Ag nanoparticles in acetone. The concentrated Ag nanoparticle suspension was serially diluted to obtain concentrations of 0.37, 0.19, and 0.10 mmol for photocathode performance evaluation. In addition to this, a higher concentration of 1.5 mmol solution was also prepared. These solutions were then ready to be incorporated into the LFO films by spin coating method.

5.1.4.2 Preparation of Nickel Nanoparticles

The Ni nanopowder (2.84 mmol) is placed into a vial containing acetone (15 ml). Subsequently, it was ultrasonicated for 2 hours to break down any large particles and for obtaining a homogeneous suspension of Ni nanoparticles in acetone. The concentrated Ni nanoparticle suspension was serially diluted to obtain a concentration of 1.42 mmol for photocathode performance evaluation. In addition to this, a higher concentration of 5.68 mmol solution was also prepared. These solutions were then ready to be incorporated into the LFO films by spin coating method.

5.1.4.3 Fabrication of $LaFeO_3$ – Ag and $LaFeO_3$ – Ni by Spin Coating

A strip of Kapton tape was pasted onto FTO glass for electrical contact (figure 34 (a)). The 5 different Ag nanoparticle concentrations were pipetted (4 drops) onto separate LFO film surfaces, and named LFO-Ag (1.5 mmol), LFO-Ag (0.77 mmol), LFO-Ag (0.37 mmol), LFO-Ag (0.19 mmol) and LFO-Ag (0.10 mmol) respectively. The 3 different concentrations of Ni nanoparticles were also pipetted (4 drops) onto separate LFO film surfaces, and named LFO-Ni (5.68 mmol), LFO-Ni (2.84 mmol) and LFO-Ni (1.42 mmol) respectively.

These were then spin coated (Midas System Spin – 1200D, figure 34 (b)) at 500 rpm for 30 seconds to uniformly spread the nanoparticles across the films. These electrodes were then annealed at a low temperature of 50 - 60 °C for 15 min. This ensures the evaporation of acetone and enhances the binding of Ag/ Ni nanoparticles to the film without their oxidation. These films are then ready for testing.

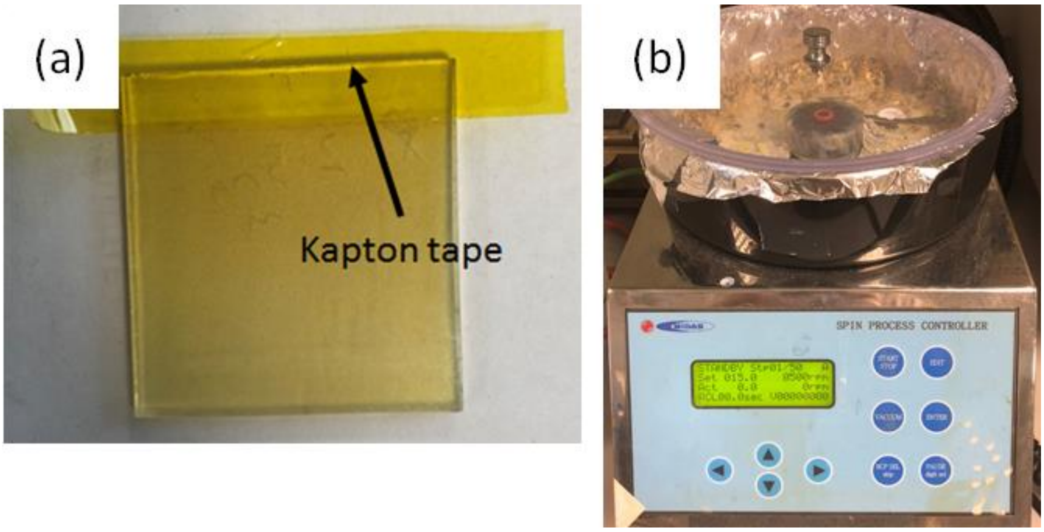

Figure 34: a) Image showing photocathode with Kapton tape strip for electrical contact and **b)** spin coater.

5.1.5 TaFeO$_4$ Preparation

Tantalum (V) chloride (99.99 %) and Methanol (99.8 %) was obtained from Acros Organics. Citric acid (99 %) and iron (III) chloride was obtained from Sigma – Aldrich. Ammonium hydroxide solution (35 %) was purchased from Fisher Scientific.

Iron (III) chloride (0.1 mol) and tantalum (V) chloride (0.1 mol) were dissolved in methanol under constant stirring. Ammonium hydroxide (25 ml) was added to for precipitates of iron and tantalum hydroxide. The precipitates are then collected by centrifuge where it is spun for 5 minutes at a rate of 3600 rpm. The supernatant is decanted off and de-ionized water is added for cleaning process. After shaking vigorously, the precipitate is centrifuged again for 5 minutes at 3600 rpm and the supernatant is decanted off. This cleaning process occurs 2 times. In a separate beaker citric acid (2 mol) is dissolved in de-ionized water. The precipitates are added to the citric acid solution and stirred with gentle heating until dissolved. Heating is continued until solvent has evaporated until a gel remains.

5.2 Material Characterisation

5.2.1 Structural Properties

The structural properties and composition of the synthesised materials were characterized using Bruker D8 Advance X-ray diffractometer (Cu Kα irradiation λ – 1.5406 Å, 40kV/ 40mA, 0.02 °2θ step and a scan time of 3 seconds per step) in the range of 20-70 °2θ. The Raman shift pattern was obtained using the Renishaw RM1000 (Renishaw plc, Gloucestershire, UK) with a 532 nm Ar ion-laser.

5.2.2 Morphological Study

The morphology and composition of the films were characterized using a high resolution scanning electron microscope (SEM, HITACHI S3200N) coupled with and energy dispersive spectroscopy (EDS, Oxford instrument elemental analysis). Film thickness was characterised using focus ion beam scanning electron microscope (FIB – SEM, NOVA NanoLab FEI 600 dual beam FIB SEM).

5.2.3 Optical Properties

The films absorbance measurements were conducted using a UV-Vis-NIR Spectrophotometer (PerkinElmer lambda 1050 with 150 mm integrated InGaAs sphere). The incident photon to electron conversion efficiency (IPCE) was obtained by measuring the incident photon flux using a 75 W xenon lamp connected to a monochromator (TMc300, Bentham Instruments Ltd., Berkshire, UK). The light was calibrated using a silicon diode. Photocurrent spectra for IPCE were measured at -0.7 V using a combination of a lock-in amplifier (Bentham Instrument Ltd., Berkshire, UK) and a custom built potentiostat.

5.3 Electrochemical Characterisation

All electrochemical experiments were carried out in a standard 3 electrode system, composed of a working electrode (synthesised photocathode), platinum (Pt) wire as counter electrode and a reference electrode of Ag/AgCl in saturated KCl (figure 35). All data were collected by a potentiostat (SP 200, BioLogic Science Instruments). The working electrode potential versus the Ag/AgCl reference electrode used in all experiments was converted into the reversible hydrogen (RHE) electrode using Nernst equation (equation 10)[4]:

$$E_{\mathrm{RHE}} = E_{\mathrm{Ag/AgCl}} + 0.197\ \mathrm{V} + 0.059\ \mathrm{V} * \mathrm{pH}. \qquad \textbf{(eq. 10)}$$

Where E_{RHE} is the converted potential vs. RHE, $E°_{Ag/AgCl}$ = 0.197 V at 25 °C and $E_{\mathrm{Ag/AgCl}}$ is the experimentally measured potential against Ag/AgCl.

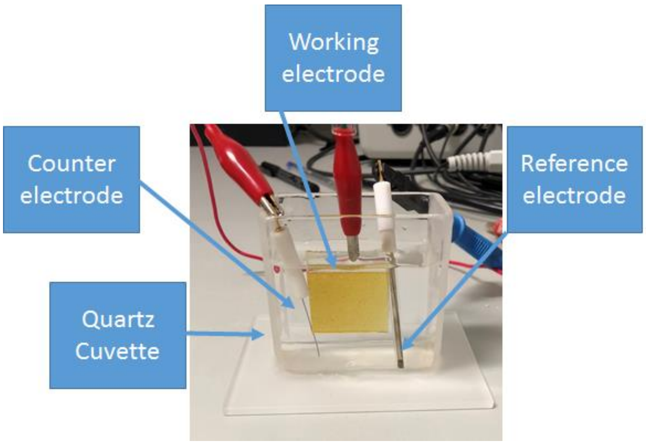

Figure 35: Image depicting a three electrode system for photoelectrochemical measurements.

5.3.1 Linear Sweep Voltammetry

The photoelectrochemical (PEC) performance of the synthesised materials were measured in 0.1 M NaOH aqueous solution (pH 13) under chopped light illumination using a 100 W ozone free Xenon lamp equipped with an AM 1.5 filter (Oriel LCS-100, Newport). The light intensity was 1 sun illumination (100 mW cm^{-2}). The liner sweep voltammetry (LSV) was scanned in the positive to negative direction between the ranges of +0.3 V to -0.7 V.

5.3.2 Electrochemical Impedance Spectroscopy

Mott-Schottky analysis was carried out using electrochemical impedance spectroscopy (EIS) in the dark in 0.1 M NaOH (pH 13). The impedance spectra were acquired at frequencies from 3 MHz to 10 mHz in the potential range of -0.3 V to +0.6 V.

5.3.3 Chronoamperometric Measurements

Chronoamperometric (CA) measurements was used to test the stability of $LaFeO_3$. It was conducted over a period of 21 hours under 1 sun illumination with periodic chopping. The sample was subjected to illumination conditions of 45 minutes and dark conditions for 15 minutes. This was carried out in 0.1 M NaOH (pH 13) in a standard 3 electrode system in ambient atmosphere and temperature. A constant current of -0.3 V was maintained over the measurement period. CA measurements for LaFeO3−Ag and $LaFeO_3$-Ni was conducted over a period of 24 h under a continuous 1 sun illumination. This was carried out in 0.1 M NaOH (pH 13) aqueous solution with no sacrificial agents, in a standard three electrode system in ambient atmosphere and temperature. A constant voltage of 0 V was maintained over the measurement period.

5.4 Hydrogen Evolution Measurement for Photocathodes

Gas chromatography (GC) measurements were carried out using a manual injection GC system (PerkinElmer Clarus 580) using a molecular sieve (PerkinElmer) and a PDD detector with an argon flow of 28 ml min^{-1}. A custom made glass reactor vessel with an attached fused silica viewport (figure 36) containing 0.1 M NaOH (pH 13) with a dead space of 100 ml was purged with argon for 2 hours with gentle heating and stirring to remove atmospheric air from the system. No sacrificial agents were used. The sealed vessel contained either LFO/ LFO-Ag/ LFO-Ni working electrode connected to a Pt mesh by a single outer wire and was subjected to light illumination (1 sun) for the water splitting reaction. GC measurements were carried out for 6 hours with measurements taken at an hourly interval. No external bias was used.

Figure 36: Custom made reactor vessel attached with fused silica viewport, with a single looped wire connecting the working electrode to the Pt mesh counter electrode. Used in hydrogen evolution test.

5.5 Hydrogen Evolution Measurements for Photocatalyst

Gas chromatography (GC) measurements were carried out using a manual injection GC system (PerkinElmer Clarus 580) using a molecular sieve (PerkinElmer) and a PDD detector with an argon flow of 28 ml min^{-1}. A vial containing 0.1 M NaOH (pH 13) with a dead space of 5 ml, and 0.1 g of photocatalyst powder, was purged with argon for 2 hours with gentle heating and stirring to remove atmospheric air from the system. The system is then sealed. No sacrificial agents were used. The vial is subjected to continuous light illumination (1 sun) under constant stirring for the water splitting reaction.

GC measurements were carried out for 6 hours with measurements taken at an hourly interval.

5.6 Finite Difference Time Domain (FDTD) Simulation

The excitation, absorption and scattering simulations for optimizing the Ag and Ni nanoparticles for LFO-Ag and LFO-Ni photocathodes were conducted using Lumerical software.

5.7 Summary

All the materials, methods and equipment's used to carry out the research in this thesis is presented in this chapter. All the materials synthesis and characterisation was done in the laboratories at the University of Exeter by me. The FDTD simulation and their study were done by our collaborators at IIT Madras. Transparent yellow thin film of $LaFeO_3$ is synthesised by spray pyrolysis, which produced very uniform films consistently.

Reference

(1) Ching-Prado, E.; Watson, A.; Miranda, H. Optical and Electrical Properties of Fluorine Doped Tin Oxide Thin Film. *J. Mater. Sci. Mater. Electron.* **2018**, *29* (18), 15299–15306.

(2) Tesfamichael, T.; Will, G.; Colella, M.; Bell, J. Optical and Electrical Properties of Nitrogen Ion Implanted Fluorine Doped Tin Oxide Films. *Nucl. Instruments Methods Phys. Res. Sect. B Beam Interact. with Mater. Atoms* **2003**, *201* (4), 581–588.

(3) Patil, P. S. Versatility of Chemical Spray Pyrolysis Technique. *Mater. Chem. Phys.* **1999**, *59* (3), 185–198.

(4) Gómez-Solís, C.; Ballesteros, J. C.; Torres-Martínez, L. M.; Juárez-Ramírez, I. RuO2-NaTaO3 Heterostructure for Its Application in Photoelectrochemical Water Splitting under Simulated Sunlight Illumination. *Fuel* **2016**, *166*, 36–41.

Chapter 6: Results and Discussion

In this chapter the synthesis and optimisation of the p-type $LaFeO_3$*,* $LaFeO_3$*-Ag and* $LaFeO_3$*-Ni photoelectrode for photoelectrochemical (PEC) water splitting is investigated. Also, the synthesis and optimisation of* $TaFeO_4$ *photocatalyst is investigated. In order to fabricate these inexpensive photoelectrodes and photocatalysts simple, low-cost and reproducible synthesis and deposition techniques were employed. Sol-gel, spray pyrolysis (SP) and spin coating techniques were used to fabricate thin film photoelectrodes and photocatalysts. The synthesis, characterisation and performance of these synthesised materials are described and discussed in this chapter. The synthesised materials are studied and discussed in several sections.*

In the first section of this chapter the synthesis and optimisation of $LaFeO_3$ *(LFO) photocathode by SP is discussed. The material is characterised, its performance is evaluated using various electrochemical techniques and its hydrogen evolution capability is also evaluated. This section has been published in Natures Scientific Reports where I am the first author and is given in appendix 1.*

The second section of this chapter discusses the synthesis and optimisation of $LaFeO_3$*-Ag (LFO-Ag) photocathode by SP of LFO and incorporation of silver (Ag) nanoparticles by spin coating method, to enhance the LFOs performance for higher hydrogen yield. The material is characterised and its electrochemical and hydrogen evolution performances are evaluated vs plain LFO. This work is done in collaboration with colleagues from IIT Madras where they investigated the finite difference time domain (FDTD), providing* *theoretical simulations of the Ag nanoparticle to determine the optimized Ag particle size for best performance. This section has been published in ACS Applied energy material where I am the first author and is given in appendix 2.*

The third section of this chapter discusses the synthesis and optimisation of $LaFeO_3$*-Ni (LFO-Ni) by SP of LFO and incorporation of nickel (Ni) nanoparticles by spin coating method, for improving it performance in hydrogen evolution against the plain LFO but replacing the costly Ag with Ni to bring down the overall cost. The material is characterised and its electrochemical and hydrogen evolution performances are evaluated vs plain LFO. This work is done in collaboration with colleagues from IIT Madras where they investigated the finite difference time domain (FDTD), providing theoretical simulations of the Ni nanoparticle to determine the optimized Ni particle size for best performance. This section has been published in the International Journal of Hydrogen Energy where I am the first author and is given in appendix 3.*

The fourth section of this chapter investigates the synthesis and optimisation of $TaFeO_4$ *photocatalyst prepared by sol-gel method. The material is characterised and its hydrogen evolution capability is investigated.*

The fifth section is work done with collaborators where they fabricated and characterised different ZnO/carbon metal organic frameworks (MOFs) and tested for photocatalytic dye degradation. I measured the various ZnO/carbon MOFs for photocatalytic water splitting application to measure it hydrogen generation performance. This section has been published in Carbon journal where I am the second author and is given in appendix 4.

6.1 Unbiased Spontaneous Solar Fuel Production Using Stable $LaFeO_3$ Photoelectrode

6.1.1 Introduction

A promising way of storing solar energy is via chemical fuels, in particular hydrogen as it is considered as a future energy carrier.[1–4] The greatest challenge is to develop a suitable technology for large scale and cost effective solar fuel production to compete with fossil fuel. One way this could be achieved is by using photoelectrochemical (PEC) water splitting which directly converts water and sunlight to solar fuel (hydrogen). Since the discovery of solar water splitting by Fujishima and Honda,[5] extensive research interest has been growing in developing efficient and stable PEC water splitting devices for a carbon free method of hydrogen generation,[6–11] however the ideal material has not been discovered.

Cost effective solar fuel generation is hindered by the semiconductor material not meeting certain essential criteria to achieve highly efficient solar to hydrogen conversion. These criteria are as follows: (i) the visible part of the solar spectrum must be absorbed for higher efficiency of hydrogen production and the band edges should ideally straddle the redox potential of water splitting, (ii) the photoexcited carriers must separate and migrate to the surface without recombination, (iii) adsorbed species must be reduced and oxidized by the photogenerated electrons and holes to produce H_2 and O_2.[1,12] Also for cost effective, environmental and scalability issues, earth abundant non-toxic materials should be the focus of research into new semiconductor materials.

Since Fujishima and Honda, who first demonstrated solar water splitting using TiO_2 electrode,[5] the optimal material remains to be discovered. Many common semiconductor materials have been investigated, including TiO_2,[13] ZnO,[14] WO_3,[15] α-Fe_2O_3,[16,17] $BiVO_4$,[18] metal chalcogenides,[19] Ta_3N_5[20] and oxynitrides TaON.[21] Most of the stable oxide semiconductors such as SnO_2, Ta_2O_5, TiO_2, and ZnO are only photoactive in UV region due to their wide bandgap, which limits their absorption of sunlight. While small bandgap metal oxides such as α-Fe_2O_3, and $ZnFe_3O_4$ can harvest maximum solar spectrum, their conduction band potentials are more positive than water reduction potential, thus, they require an external bias for water splitting. Metal chalcogenides such as CdS and CdSe have ideal band structures for spontaneous water splitting but are highly unstable under water photo-oxidation conditions. Similarly, other ideal candidates such as metal nitrides and oxynitrides also suffer from photocorrosion and photo-oxidation, which limits their applications in water splitting.

A number of different p-type semiconductor materials have been developed for PEC water splitting application, such as; Cu_2O[6], NiO[22], $CaFe_2O_4$[23]. These photocathode materials show good photocatalytic activity for water splitting. However, a number of issues with these materials inhibit them from performing effectively as PEC devices. Cu_2O has been shown to have one of the highest current densities (10 mA cm^{-2}) of metal oxide semiconductor materials and has attracted wide research interest, however it is highly unstable as after a few minutes the material will visibly degrade under PEC performances.[24] This high level of instability has led researchers to add protective aluminium-doped zinc oxide (AZO) and TiO_2 layers to improve the

Cu_2O stability but this requires complicated, expensive and non-scalable techniques such as atomic layer deposition or sputtering. NiO is a highly stable material under PEC conditions, however exhibit poor photon harvesting performance due to its large band gap (3.45 eV) which only enables it to access to the UV region. $CaFe_2O_4$ has been shown to be a very promising material as it has a narrow band gap of 1.9 eV and band edges that straddle the redox potential of water (-0.6 and +1.3 V). This allows $CaFe_2O_4$ access to the visible region of the light spectrum and to be able to split water into its constituents (H_2 and O_2). However, it requires high fabrication temperatures (1100 – 1200^{o}C) which does not make the synthesis process very cost effective.

Recently, tremendous research efforts have been made to develop unassisted PEC system for H_2 production and Wang et al. has reviewed recent progress made in unassisted PEC water splitting.[25] Among cheap visible light active and stable oxides, the bench mark PEC device with tandem structure are (i) the core-shell WO_3/ $BiVO_4$/ CoPi with GaAsP photovoltaic has photocurrent of 6.56 mA cm^{-2} with H_2 evolution rate of 102 μmol/h[26] and (ii) without photovoltaic assistance *p*-$LaFeO_3$ photocathode and *n*-Fe_2O_3 photoanode based PEC water splitting devices have demonstrated H_2 evolution of 11.5 μlmol/ h with longest working life of 120 h[7]. Among single oxide visible PEC materials, α-Fe_2O_3 is one of the most investigated material, only Pt-doped α-Fe_2O_3:Co-Pi photoelectrode is reported to generate unassisted H_2 from water.[27] Along with PEC water splitting, $LaFeO_3$ has been involved in photocatalytic dye degradation[28,29] and hydrogen evolution[20,21] using powder samples. Another important fact related to $LaFeO_3$ is p-type photocurrent characteristics with the potential to act as photocathode in tandem PEC cell. Stable photocathode under PEC condition is highly desirable to progress in field of solar fuel production. However, progress to improve PEC response of $LaFeO_3$ photocathode is very slothful due to the lack of a sophisticated fabrication technique for high quality nanostructured thin films.

To the best of our knowledge, we report for the first time the nanostructured $LaFeO_3$ photoelectrode for spontaneous hydrogen evolution from water without any external applied bias. The $LaFeO_3$ photoelectrode was fabricated by spray-pyrolysis, a novel, inexpensive and scalable method, to create a stable thin film p-type semiconductor material which displays an ideal band structure with band edges saddled above and below the redox potential of water. The fabricated photoelectrode exhibits excellent PEC performance and is stable under redox water condition for more than 21 hours.

6.1.2 Optimisation of $LaFeO_3$ by Sol-Gel

The aim of this work is to synthesise single phase crystalline LFO for solar hydrogen evolution and optimising the reaction conditions for making LFO. Initially in this work the sol-gel method was used and the optimum annealing temperature was determined. Iron (III) nitrate (50 mmol) is dissolved in methanol and ammonium hydroxide is added to form precipitates of iron hydroxide. The precipitates were collected by centrifuge and washed with de-ionized water two times. Lanthanum (III) isopropoxide (50 mmol) is added to the precipitate of iron hydroxide with trifluoroacetic acid (1 ml) and methanol (1 ml) and is ground together until it dissolves and a gel forms. The gel is then calcined in the box furnace at different temperatures (550ºC, 600ºC, 650ºC and 700ºC) for 3 hours to form crystalline nanopowders.

6.1.3 Optimisation of $LaFeO_3$ by AACVD

In a typical deposition 20 ml of solution containing 0.1 M of $La(iPro)_3$, $FeCl_3$ and methanol is placed in a round bottomed flask and turned to an aerosol by ultrasonication. A flow of compressed air is used to transport the generated aerosol to another round bottomed flask, at a rate of 120 ml min^{-1}, to trap any droplets. A second flow rate of 3 L min^{-1} transports the remaining aerosol to the hot plate containing FTO for deposition, where the temperature is set to 550ºC.

6.1.4 Optimisation of $LaFeO_3$ by Hydrothermal

In this process 0.1 M of $La(iPro)_3$, $FeCl_3$ and citric acid is dissolved in methanol and placed into a Teflon lined steel autoclave. The autoclave contains FTO substrate. This is placed into a box furnace where it was annealed at low temperatures of 200ºC for 12 hours.

6.1.5 Conclusion of Optimisation

The sol-gel method is used to fabricate single phase crystalline $LaFeO_3$ (figure 37) at various temperatures. We can see that they all have LFO peaks (JCPDS 00-037-1493) with an orthorhombic system. No observable impurities were detected. As the temperature increases to 700ºC the peaks become sharper indicating the material is becoming more crystalline.

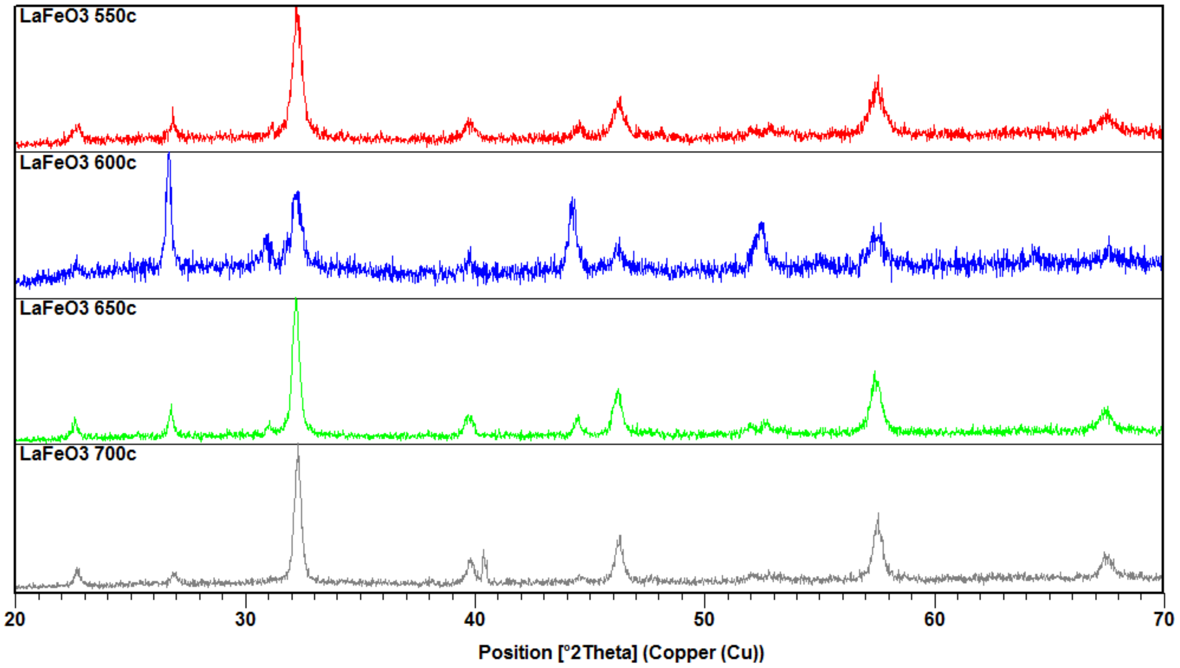

Figure 37: XRD pattern of $LaFeO_3$ samples calcined at different temperatures.

Once it was confirmed that a single crystalline phase of LFO is formed, the gel was pasted onto FTO glass substrate to attempt to fabricate a LFO photoelectrode. The coated FTO was then annealed at 550°C, 600°C, 650°C and 700°C. After the annealing process it was observed that all the films had cracks on them, were not uniform and was peeling off. This may be due to gas bubbles being released from the gel during the heating process causing films to crack and peel as the bubbles form.

The aerosol assisted deposition (AACVD) method was used to overcome the film cracking/ delamination. From sol-gel method 550°C temperature was required for single phase material. However, it was observed that with this method the temperature causes the precursor to undergo thermal decomposition before coating the substrate. Hence it was difficult to synthesis uniform films.

Hydrothermal method was used to address the temperature issue as this method synthesises materials at low temperatures under high pressure. However, it was discovered that the particles did not adhere to the FTO substrate at all.

To overcome this problem an alternative synthesis method is used, spray pyrolysis (SP). In this process it is based on a two-step fabrication process, where the film is uniformly coated onto the FTO at low temperatures followed by a higher heat treatment to form the desired material. The reason this involves a two-step heating process is due deposition temperature. If the hotplate during SP is too low the droplets splash onto the FTO substrate and decomposes leaving a non-uniform film layer. However, if the temperature is too high the solvent evaporates completely before the droplets arrive at the FTO substrate and dried particle ashes will land onto the FTO with poor or no adherence at all.[32] Therefore, an optimum temperature is required to allow the solvent to evaporate just as the droplets arrive onto the FTO substrate to allow for good film adherence and uniformity.

Spray rate is another important factor which could affect the films deposition during SP. If the spray rate is too high it will lead to formation of rough films and there is a low evaporation rate of the solvent, leading to thicker films which can peel off during the second annealing stage. If the deposition takes place at a lower spray rate then typically more uniform and thinner films are produced due to higher evaporation rate.[33]

From our experience with the spray pyrolysis technique, we observed that a deposition temperature of 150ºC and spray rate of 1 ml min^{-1} was the optimum parameters to obtain well adhered uniform films. These parameters are fixed for all SP synthesis methods and are discussed in the following section.

6.1.6 Synthesis of $LaFeO_3$ Photocathode by Spray Pyrolysis

The full experimental details for $LaFeO_3$ are given in chapter 5.

6.1.6.1 Results and Discussion

Nanostructured LFO photoelectrode were successfully synthesised and the optimisation of film synthesis is investigated. A comparative study on the effect of long term chronoamperometric (CA) test of the film before and after is investigated and showed excellent stability of the film. Moreover, the hydrogen evolution capability of the films without any bias is studied as well as its reusability.

6.1.6.1.1 Material Characterisation

LFO photoelectrode was prepared by spraying precursor solution at 150°C with spray rate of 1 ml min^{-1} and then annealed at different temperature from 475°C to 625°C with an increment of 25°C to get single phase crystalline $LaFeO_3$ material. The XRD pattern for the various annealed samples are given in figure 38. We observe a single crystalline phase of LFO with no impurities (JCPDS 00-037-1493) with an orthorhombic system at 550ºC and as the temperature increases the peaks become more crystalline.

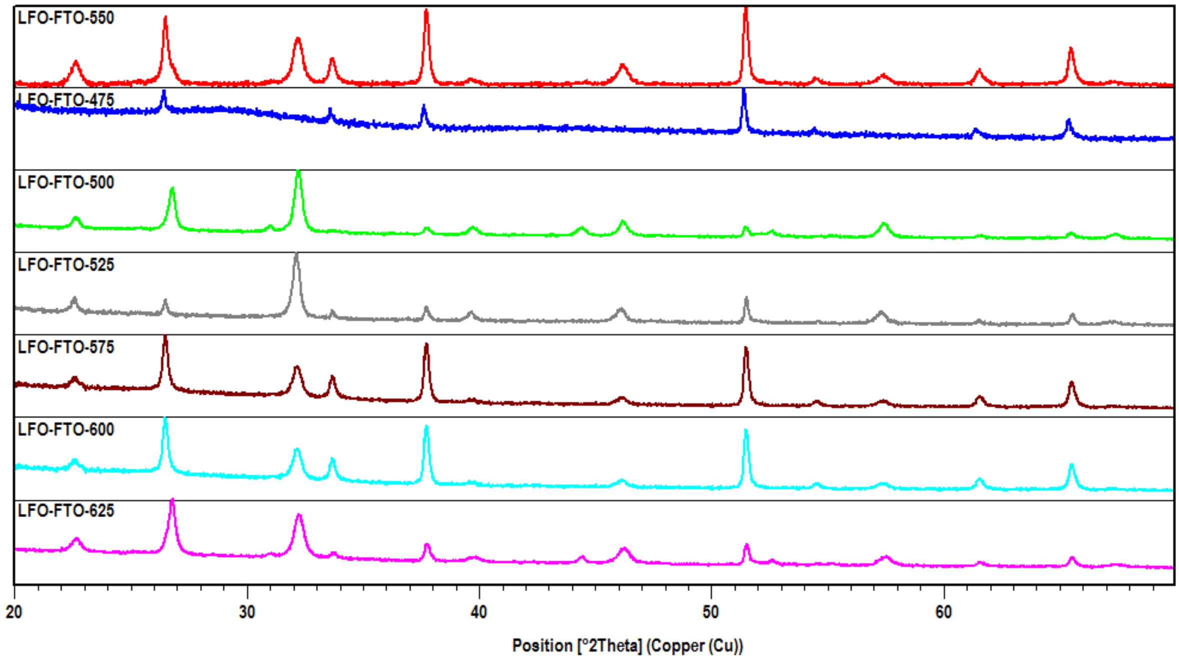

Figure 38: XRD pattern of the various LFO samples annealed at various temperatures.

Furthermore, an XRD pattern before and after chronoamperometric (CA) test is taken to see if there is any change in the materials crystallinity or if there is any phase change (figure 39). The peaks marked with an asterisk indicate FTO and all other peaks correspond to LFO. It can be observed that after the CA test there is no change to the materials crystallinity and no new phase is detected, it is still single phase LFO. This indicates that the material is very stable during and after CA testing. The XRD Peak pattern shows that the films are crystalline with LFO particles preferentially oriented in (121) direction.

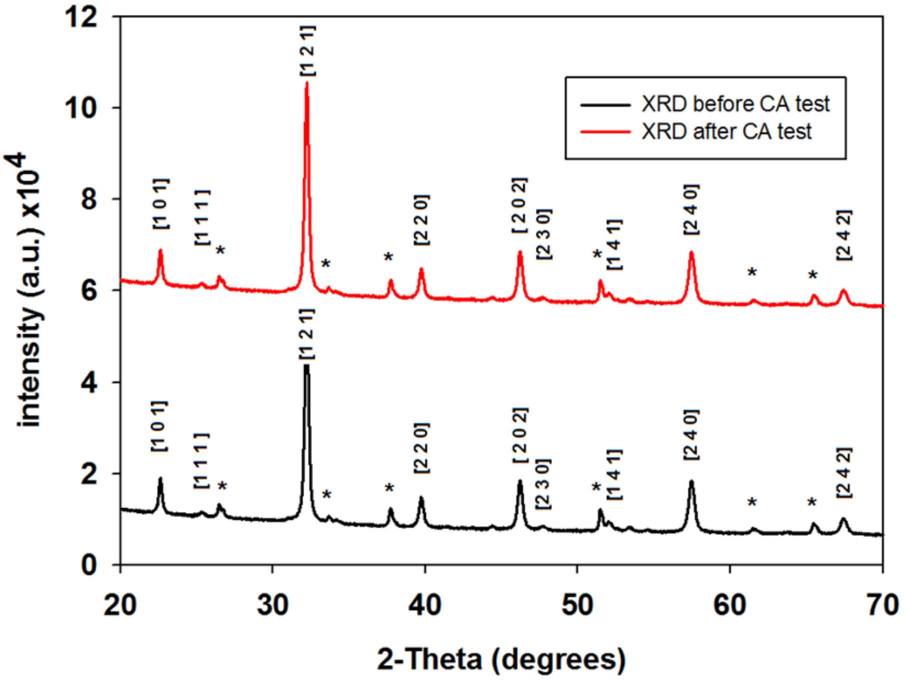

Figure 39: XRD pattern of LFO deposited onto FTO glass substrate before and after chronoamperometric test, where peaks marked with an asterisk represent FTO.

Figure 40 shows the Raman shift pattern of LFO, which is in good agreement with previous Raman shift patterns described elsewhere.[34,35] The pattern presents the structural phase of the thin film before and after chronoamperometric test. It shows that after the chronoamperometric test there is no structural phase change in the film when compared to its fresh counterpart as the pattern overlaps that of the fresh film showing no obvious change. This data is in good agreement with the XRD pattern, providing further support that the film is highly stable and does not degrade into iron oxide and lanthanum oxide. Modes caused by the La vibrations are present below 200 cm^{-1}, labelled 149 cm^{-1} and assigned B_{2g}. Mode 249 cm^{-1} is the lanthanum-oxygen octahedral tilt mode where it is assigned A_g. Modes between 400 – 450 cm^{-1} are correlated to oxygen octahedral bending vibrations, assigned B_{3g}, and modes above 500 cm^{-1} are oxygen stretching vibrations.[35] The peaks at 1128 and 1317 cm^{-1} can be attributed to the two photon scattering, however in the literature it is hotly debated whether the peak at 637 cm^{-1} is due to impurity or two photon scattering.[34] However considering the XRD pattern, it is most likely due to two photon scattering as XRD shows a single phase of $LaFeO_3$. No other peaks corresponding to lanthanum oxide or iron oxide was found which is in good agreement to the XRD pattern.

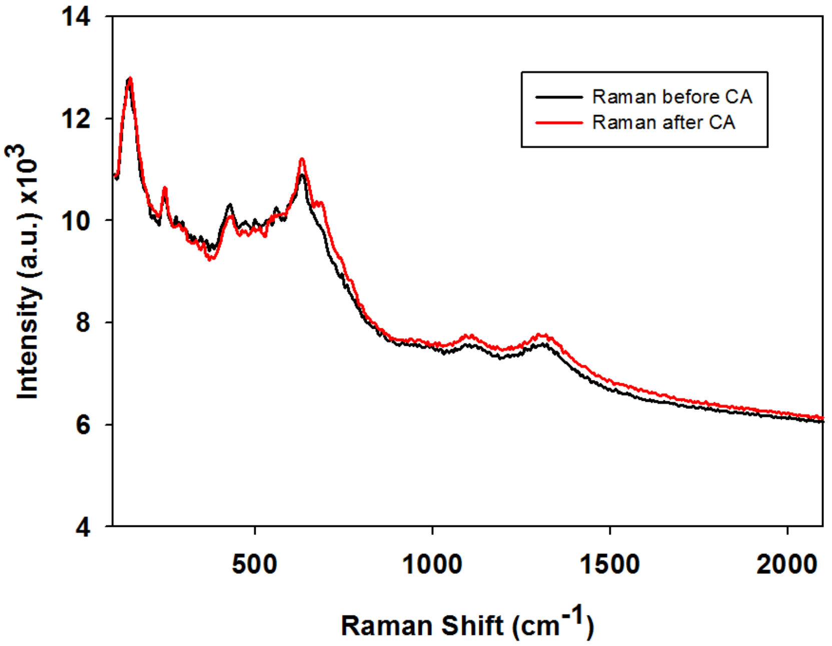

Figure 40: Raman shift pattern of LFO before and after chronoamperometric test.

The surface morphology of the LFO films before and after the CA test is studied to see if the film structure has degraded. Figure 41 (a) shows the top view SEM image of LFO before CA test. Here it is observed that the nanostructure of the material has excellent compact uniformity and well connected crystal grains in a coral like structure, post-annealing at 550^{o}C. Figure 41 (b) shows the top view SEM image of the film after the chronoamperometric test. We can clearly note that the film retains its uniformity and good interconnection between the crystal grains. Figure 42 (c) shows the FIB-SEM cross section of the film with thickness of 382 nm.

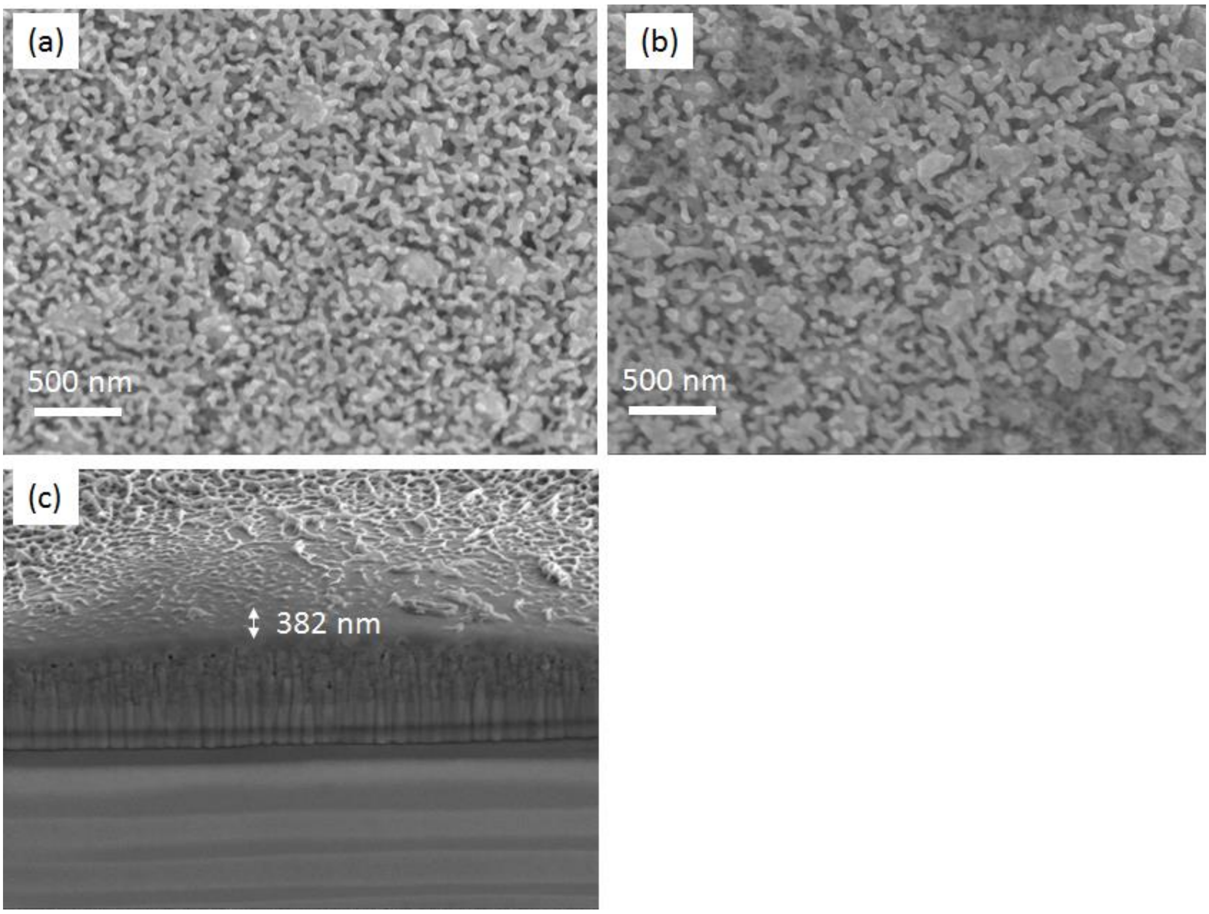

Figure 41: (a) and **(b)** Top view SEM of $LaFeO_3$ thin film before and after chronoapeometric test and **(c)** FIB-SEM cross section of $LaFeO_3$ photoelectrode.

In addition, figure 42 shows the EDX of LFO indicating the lanthanum, iron and oxygen peaks. This further confirms the composition of the materials, which aligns with the XRD and Raman patterns. Figure 43 shows that the lanthanum and iron are homogenously mixed in the LFO film, by element mapping from top view EDX characterization, further emphasizing the uniformity of the film.

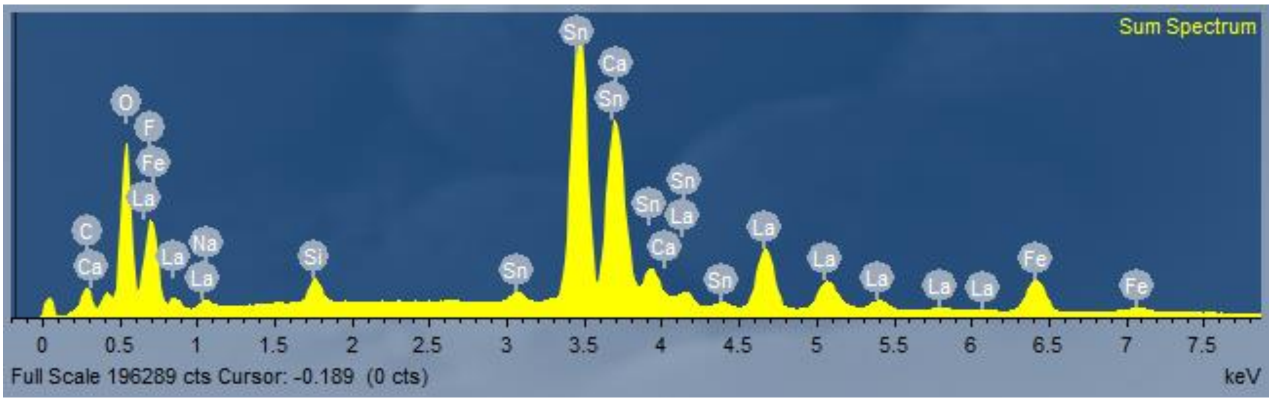

Figure 42: EDX of $LaFeO_3$ showing peaks of lanthanum, iron and oxygen.

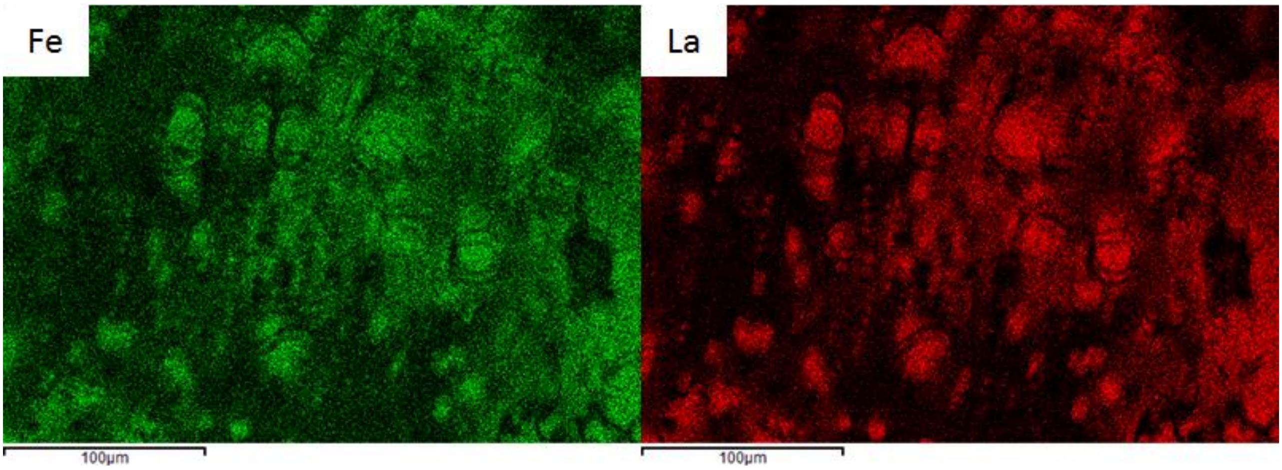

Figure 43: Elemental mapping from EDX showing the distribution of iron and lanthanum in the film.

6.1.6.1.2 Photoelectrochemical Analysis

The PEC performance of LFO was performed in 0.1 M aqueous NaOH (pH 13) solution by illuminating the photoelectrode from the electrolyte side, where the light was chopped every 0.01 V. The photocurrent density (*J*) is plotted against bias potential (*V)* as shown in figure 44. The steady state photocurrent onset potential estimated from the *J*-*V* plot was at 1.2 V vs. RHE. The photocurrent density rises up to approximately 0.16 mA cm^{-2} at 0.26 V vs. RHE, while no clear dark current is observed between the measured potential ranges. Due to the compact nature of the film it will be difficult for the electrolyte to penetrate deep into the film, thus we have a relatively low photocurrent. The large spikes during each chop is due to transient electrons generated undergoing recombination with their respective hole, as the accumulated charges do not have enough time to interact with the electrolyte before/ after each rapid chop. This recombination effect can be seen when comparing figure 44 *J*-*V* plot to the *J*-*V* plot of figure 45, where the light was chopped at a slower rate every 0.5 V. As the light is chopped at a slower rate it allows the accumulated charges enough time to interact with the electrolyte solution allowing the charges to separate, hence we do not observe the spikes[36]. This indicate a slow charge transfer dynamics which needs to be improved and investigated further to enhance the efficiency of LFO photoelectrodes.

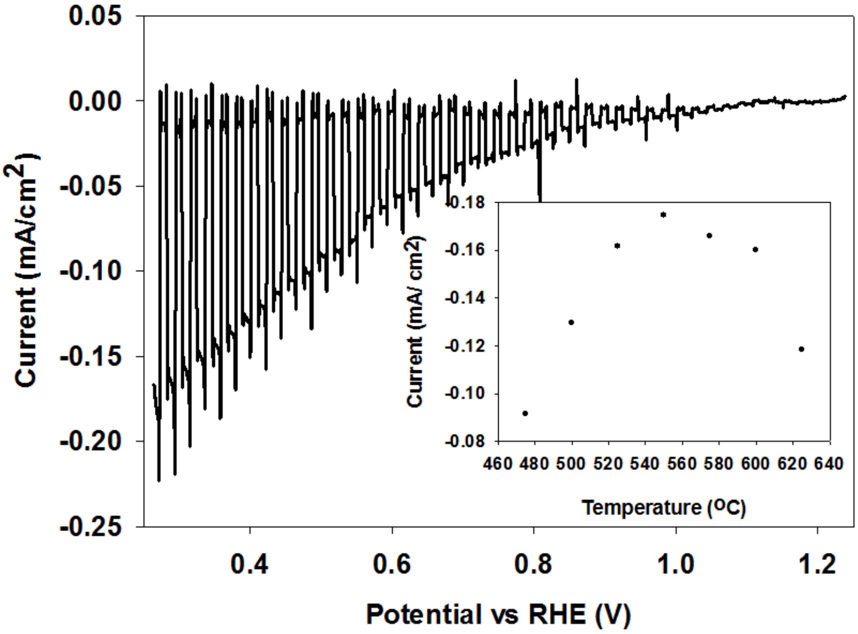

Figure 44: *J-V* characteristics of LFO under chopped illumination in a 0.1M pH 13 electrolyte, with inset showing annealing temperature effect on current density.

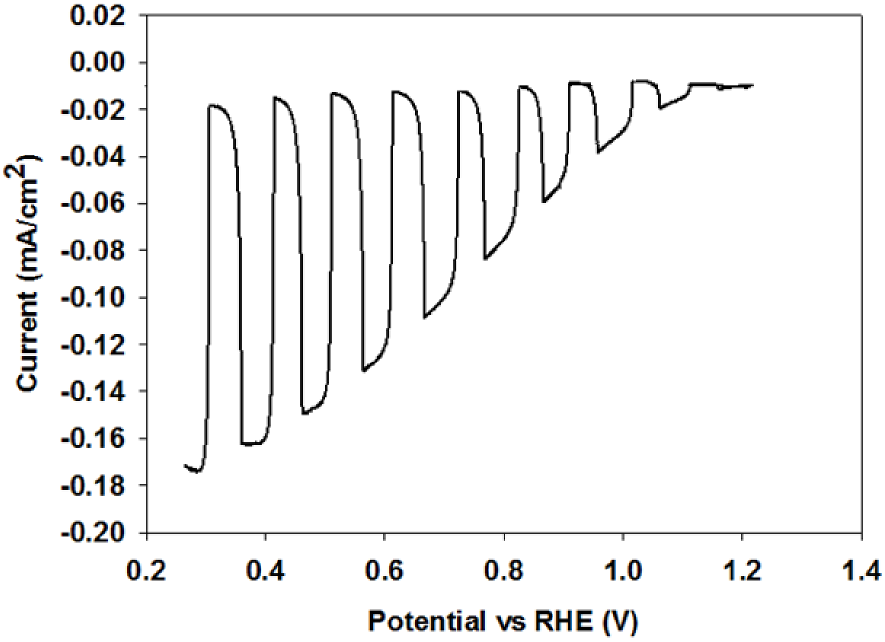

Figure 45: *J-V* characteristics of $LaFeO_3$ under chopped illumination, where each chop was done every 0.5V, in a 0.1M NaOH pH 13 electrolyte.

To determine the best fabrication conditions for LFO photoelectrode, annealing temperature and spray amount has been optimised. The annealing temperature was found to be an important factor which directly affected the photocurrent density of LFO photoelectrodes. The dependence of photocurrent density on annealing temperature is shown as inset in figure 44 and the effect of annealing temperature on *J-V* curve is given in figure 46. The photocurrent density increases with the increase of annealing temperature and reaches the optimum level at 550ºC. With further increase of the deposition temperature, the photocurrent of LFO photoelectrodes decreases significantly. XRD shows that at low temperature regime, the decomposition was not completed and the XRD peak for LFO was not detected at 475ºC. The LFO XRD peak starts appearing at 500ºC and becomes more crystalline with the increase in temperature. The low photocurrent at lower (< 550 ºC) and high (> 550 ºC) temperature regime can be due to incomplete decomposition and sintering of film respectively which can create defects, dislocations and kink sites in the film. These dislocations and kink sites may act as the recombination centres for the photogenerated electron-hole pairs and consequently showing poorer photocurrent density.

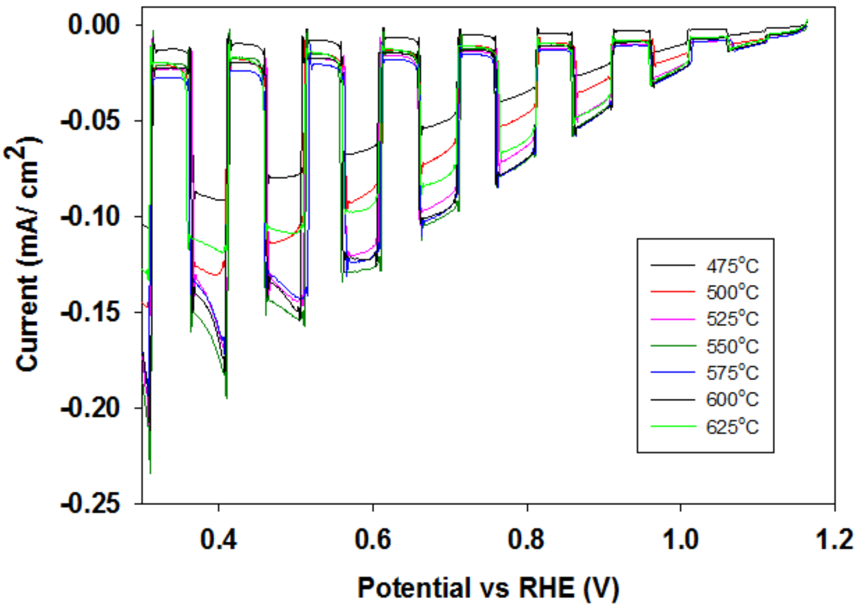

Figure 46: *J-V* characteristics of LFO at various annealing temperatures under chopped illumination in a 0.1M NaOH pH 13 electrolyte.

The photocurrent density varied with amount of spray solution /time. The amount of spray solution/ time was directly correlated to the photoelectrode thickness. As expected the photoelectrodes with short spray times are relatively thin whereas the electrodes associated with long spray times are thick. The photoelectrode deposited using 3 ml spray solution shows lowest photoresponse, which increases with increase in spray time and reached to maximum at 5 ml spray amount and then decreases. The *J-V* characteristics are shown in figure 47. The photoelectrode which showed the maximum photocurrent density had a thickness of 382 nm and corresponds to 5ml spray solution/ 5 minutes of spray time. For electrodes with higher thickness the photogenerated electrons require to travel more before collecting at the FTO substrate (here the electrodes were illuminated from the electrolyte side) depending on the thickness of photoelectrode. The electron transport within LFO is significantly slow as evident from high recombination spikes in faster chopped *J-V* (figure 44). The slow and trap dominant charge transport mechanisms within nanostructured matrix have been already reported in other metal oxide semiconductor systems.[37]

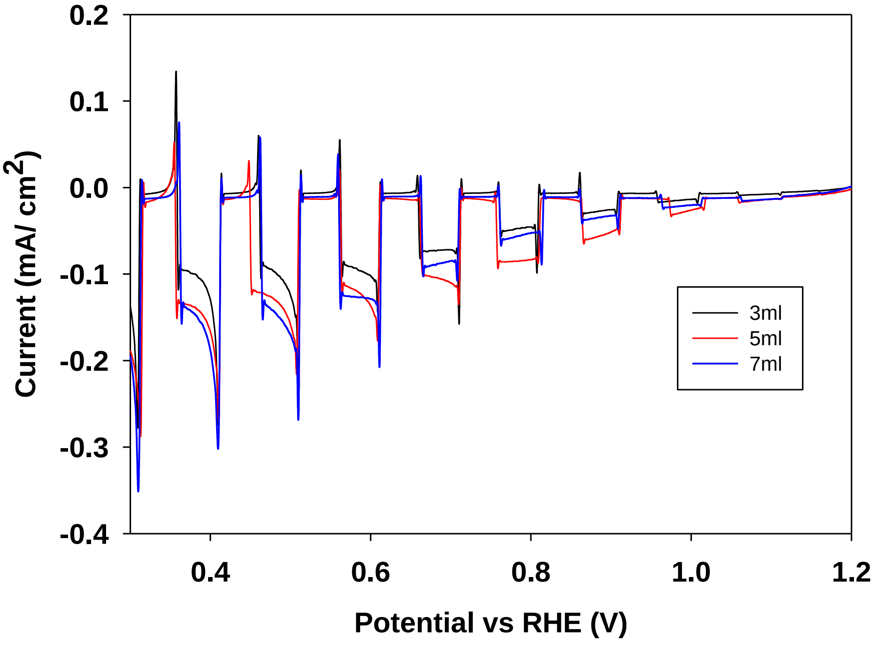

Figure 47: *J-V* characteristics of different film thickness by varying spray amount under chopped illumination in a 0.1M NaOH (pH 13) electrolyte.

A chronoamperometric test of the LFO photoelectrode was conducted to determine its stability. Figure 48 shows the results from the test where it was carried out in an aqueous 0.1 M (pH 13) electrolyte solution at a constant potential of -0.3 V over a period of 21 hours under chopped illumination, where the film was illuminated for 45 minutes and in dark for 15 minutes every hour for 21 hours. A small gas bubble accumulation (H_2) on the surface of the electrode was also observed during the test. From the graph it is observed that over the 21 hour period the photoelectrode remains photoactive giving a very stable response. However, a very slight gradual decrease in current density is observed which could be due to gas bubble accumulation. As the gas bubbles form it causes a shading effect on the photoelectrode as they tend to stick on the electrode surface, decreasing the effective area, increasing the interfacial electric resistance,[38] hence we see the slight gradual decrease in current density. The slight decrease in photocurrent starts after an hour which is in agreement with H_2 evolution. One possible way to remove the gas bubbles from the surface of the film is by putting the reaction vessel under agitation to release the bubbles from the film surface. Another reason for the decrease of the photocurrent could be due to the space charge accumulation on the surface of the film.[39] As the reaction is taking place the build-up of surface charge will create a barrier which will prevent the charges being taken up by the electrolyte, as seen in the slight drop in photocurrent. These effects can have an adverse effect on the hydrogen evolution efficiency as less electrolyte is able to penetrate the film to be available for effective charge separation. This can therefore cause a reduction in hydrogen evolution efficiency over time.

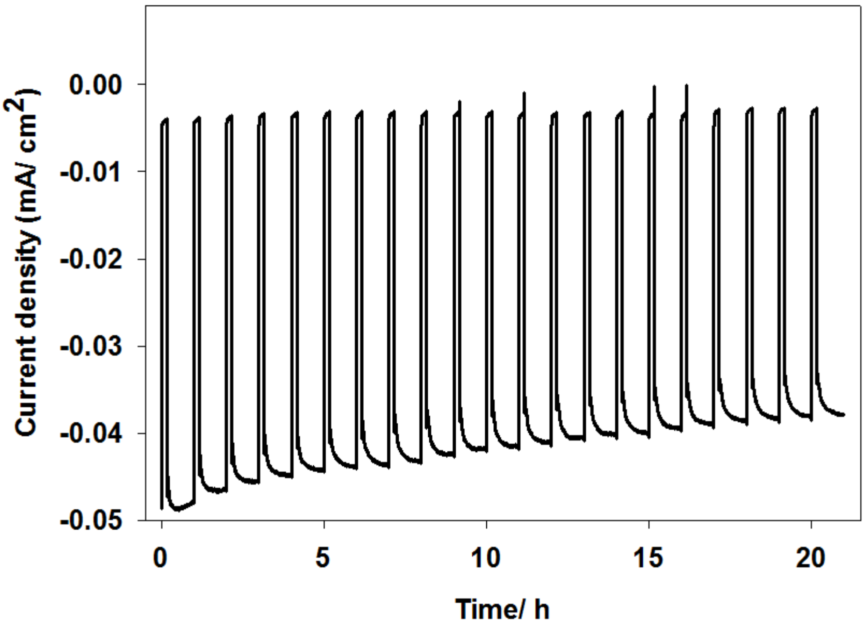

Figure 48: Chronoamperometry test of LFO under chopped illumination in a 0.1M (pH 13) electrolyte at -0.3 V vs Ag/ AgCl.

6.1.6.1.3 Optical and Electrochemical Measurements

Optical and electrochemical measurements of the optimised LFO film were taken to help determine its band gap and band edge positions. A potential factor for causing the low photocurrent may be due to the incident photons hitting the film not being sufficiently absorbed. This may be due to the film being very thin. An incident photon to electron conversion efficiency (IPCE) measurement was recorded at 0.26 V vs RHE for the LFO photoelectrode using an aqueous solution of 0.1 M NaOH. This measurement helps to determine how efficiently the photons were being converted to current, shown in figure 49. The IPCE threshold exists at about 520 nm, where the maximum efficiency of 3.2% is obtained at 350 nm. The relatively low IPCE exhibited by the LFO electrode may be due to the combined factors of weak light absorption, hole-electron recombination rate[40] and very thin film. The IPCE increased substantially from 400 nm indicating that absorbed photons of different energies have been successfully converted to photocurrents. However, the IPCE value is higher for short wavelength and decrease rapidly over 400–600 nm region compared to absorption spectrum. The IPCE near bandgap at long wavelengths is lower, which is a common characteristic of iron based photoelectrode.[27] An analysis of IPCE and absorption data allows us to calculate the absorbed photon to electron conversion efficiency (APCE). The APCE is determined from the IPCE and light harvesting efficiency (LHE) using the following equations (11) and (12)[41]:

$$LHE = 1 - 10^{-A} \qquad \textbf{(eq. 11)}$$

$$APCE = \frac{IPCE}{LHE} \qquad \textbf{(eq. 12)}$$

Where *A* is the absorbance at certain wavelengths and IPCE is determined experimentally. The APCE spectra overlaps with the IPCE spectra over the entire spectral range. The APCE shows a maximum efficiency of 3.5% which is in good correlation to the IPCE, suggesting that the quality of the film is good however it has very weak light absorption capabilities which may account for the low photocurrent (seen in figure 44) and low faradaic efficiency. In principle, it is possible to increase the thickness of active layer to absorb more photons, thus achieving a higher photocurrent. However, increasing the thickness will increase the internal resistance of the device,[42] and from figure 47 increasing the thickness beyond 5 ml spray deposition did not improve the films photocurrent.

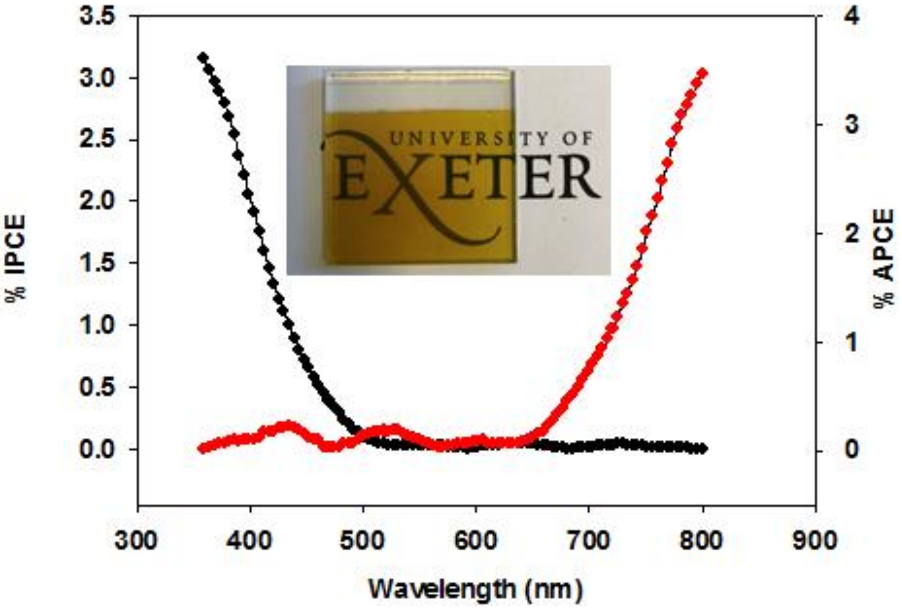

Figure 49: IPCE and APCE spectra for the nanostructured LFO thin film.

Optical absorbance measurements were taken for LFO to help determine the materials band gap. The inset of figure 50 presents the material's absorbance measurement for the LFO photoelectrode between the ranges of 350 – 800 nm. The low absorption and IPCE is attributed to very thin and semi-transparent nature of film (shown as an interest in figure 49). By using this data the band gap energy (E_g) of the LFO film can be determined using Tauc plot[43], by plotting $(\alpha hv)^{1/n}$ vs. hv and the band gap is determined by the x-axis intersect, where α is the absorption coefficient and hv is determined by 1240/ wavelength. n is 1/2 for direct allowed transitions or 2 for indirect allowed transition. In our case n value of 1/2 was selected. α is defined by Beer-Lambert's law and can be determined by the following equation (13)[44]:

$$\alpha = \frac{2.303 \; x \; A}{\mathrm{d}} \qquad \textbf{(eq. 13)}$$

Where *A* is absorbance at wavelength (λ) and d is film thickness. Figure 50 shows that LFO photoelectrode has a direct band gap of 2.4 eV, shown where the red line intersects the x-axis. This band gap value for LFO falls in line with other works conducted.[45] The narrow band gap illustrates that the material is capable of absorbing visible light.

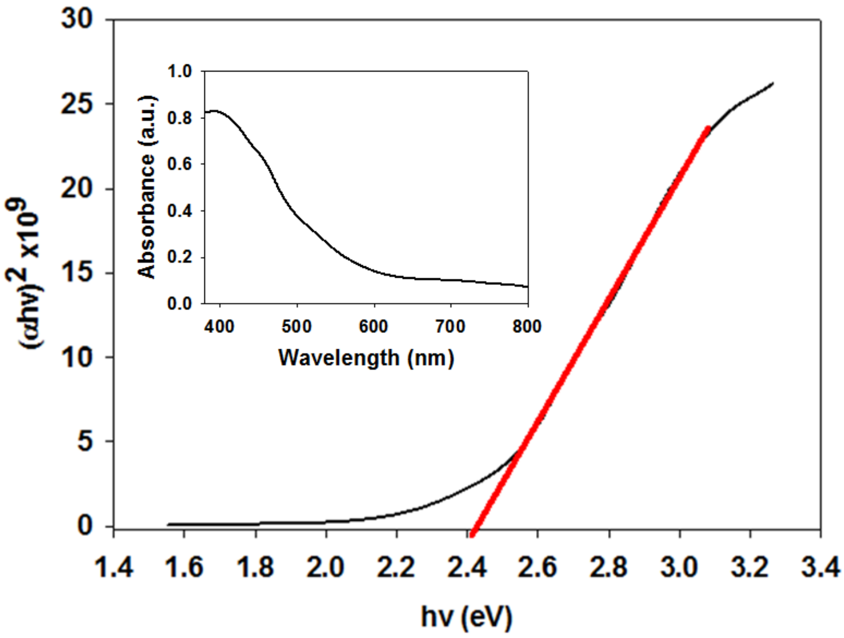

Figure 50: Tauc plot of LFO showing the band gap energy (E_g) while inset shows absorbance spectra of LFO.

Electrochemical impedance spectroscopy measurement (EIS) was conducted in order to determine the semiconductors flatband potential. Impedance data were fitted in ZView to a Randles circuit to extract the capacitance. The Mott-Schottky plot showed p-type characteristics of our LFO film. Flat band potential was extracted using the Mott-Schottky equation for p-type semiconductors (equation 14):

$$(\frac{1}{C})^2 = \frac{2}{\varepsilon\varepsilon_0 A^2 e N_D}(V - V_{\text{fb}} - \frac{k_B T}{e}) \quad \textbf{(eq. 14)}$$

where C is capacitance, e is the electronic charge, ε_r is the relative permittivity of materials, ε_0 is the permittivity of vacuum, N_A is the carrier concentration, k is the Boltzman constant, T is the absolute temperature, A is the area of electrode, V is the applied potential and V_{fb} is the flat band potential.[46] V_{fb} of LFO was determined through a linear fit in the linear region of the Mott-Schottky plot and were calculated to be 0.328 V vs Ag/ AgCl (figure 51). The measured flat band can be converted to the RHE scale using the Nernst equation (15)[47]:

$$E_{\mathrm{RHE}} = E_{\mathrm{Ag/AgCl}} + 0.059\mathrm{pH} + E^{o}_{Ag/AgCl} \quad \textbf{(eq. 15)}$$

Where E_{RHE} is the converted potential vs. RHE, $E^{o}_{Ag/AgCl} = 0.197$ V at 25°C and $E_{\mathrm{Ag/AgCl}}$ is the experimentally measured potential against Ag/ AgCl. The flat band was determined to be 1.29 V vs. RHE. The flat band potential is in good agreement with the photocurrent onset potential measured from J-V curve. Using a varied Mott-Schottky equation[48] (equation 16) the carrier density can be calculated.

$$C_{\mathrm{SC}}^{-2} = (2/e\, \varepsilon_0\, \varepsilon\, N_{\mathrm{D}})\,(V_{\mathrm{m}} - V_{\mathrm{FB}} - kT) \quad \textbf{(eq. 16)}$$

Where e is the electronic charge, ε_0 is the permittivity of vacuum, ε is the dielectric constant, N_{D} is the carrier density, V_{m} is the measured potential and V_{fb} is the flat band potential. 6 x 10^3 value is used as the dielectric constant.[49]

The carrier (hole) density was calculated to be 15.27 x 10^{18} cm^{-3}. With the flatband and band gap values determined, we can construct a relative band alignment of the LFO material to the waters redox potentials, as shown in figure 52. The valance band and the conduction band is shown to be straddling the redox potential of water with a narrow band gap. This suggests that the material is able to generate hydrogen using the visible part of the spectrum, as the conduction band is well above the reduction potential of hydrogen. This data shows that the LFO photoelectrode should be able to produce hydrogen from water splitting.

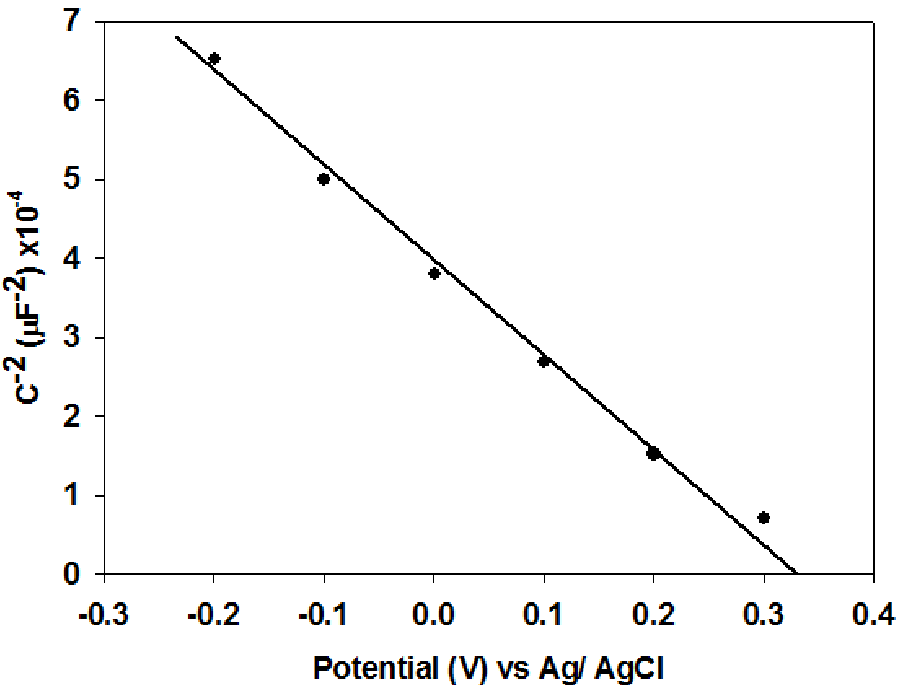

Figure 51: Mott-Schottky plot of LFO thin film obtained from impedance measurement in the dark in pH 13.

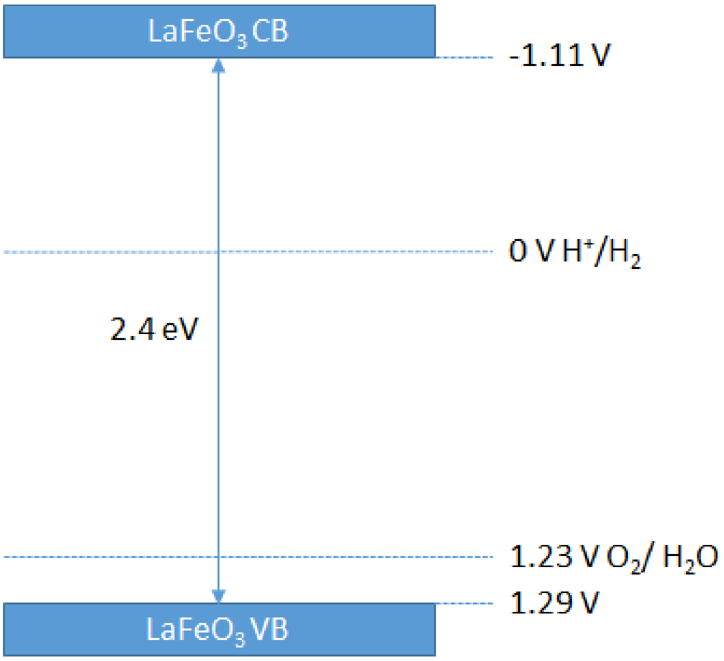

Figure 52: Band diagram of LFO.

6.1.6.1.4 Hydrogen Evolution Measurement

Figure 53 shows the hydrogen production performance of the LFO photoelectrode in an aqueous 0.1 M NaOH solution under a constant illumination. The water splitting test was conducted in a custom made glass reactor vessel with an attached fused silica viewport. The LFO working electrode and Pt mesh counter electrode were connected by a single looped wire, without any external bias being applied. Hydrogen was being produced spontaneously during the water splitting test during the first 6 hour cycle where the photoelectrode generated 0.18 μmol/ cm^2 of hydrogen after 6 hours, with a faradaic efficiency of 30%. It then underwent a second cycle of water splitting test to determine if the electrode was re-usable and how much the performance varied. After a further 6 hours illumination, the LFO thin film generated 0.08 μmol/ cm^2 of hydrogen. This provides additional evidence that the film is re-useable, although the amount of hydrogen produced is more than halved. In addition, it should be noted that the low amount of hydrogen produced and low faradaic efficiency can be attributed to the low photocurrent generated. The low photocurrent correlates with low hydrogen produced as an insufficient amount of electrons are being generated to produce a high amount of hydrogen, as seen in the *J-V* curve. Also, the electrons which are being generated are not all being converted to hydrogen as we see a low faradaic efficiency. This can be due to the electrolyte not effectively penetrating the film due to its compact morphology and/ or gas bubbles forming on the photoelectrode where they tend to stick on the electrode surface, decreasing the effective area, increasing the interfacial electric resistance and thus increasing the losses.[38] After the second cycle of water splitting test, the amount of hydrogen produced further decreases. Again this can be because of the gas bubbles accumulating onto the film surface preventing causing a shading effect, inhibition of effective charge separation and/ or space charge layer accumulated onto the film surface. This in turn hinders charge separation, lowering efficiency.

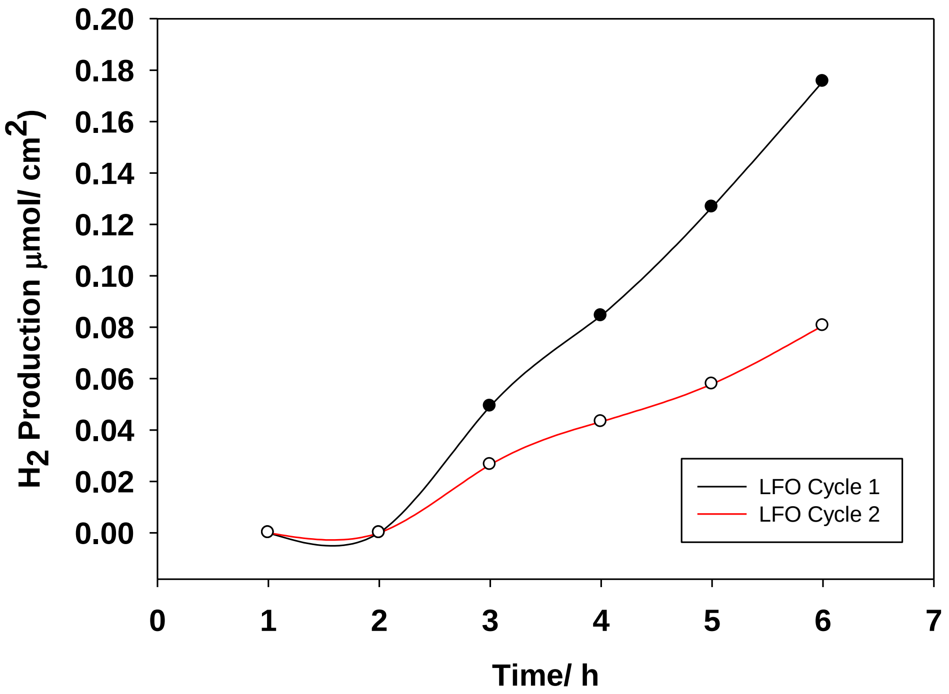

Figure 53: Hydrogen evolution test of LFO in an aqueous 0.1 M NaOH electrolyte solution, over 2 cycles.

6.1.7 Conclusion

In summary, we have developed and optimised a stable p-type $LaFeO_3$ photoelectrode with a coral like nanostructure by a novel and inexpensive spray pyrolysis technique with a post annealing step, which yields a photocurrent density of 0.16 mA/ cm^2 at 0.26 V vs. RHE. Chronoamperometric studies showed that the LFO film provides a stable p-type response over a 21 hour period. Optical and impedance data showed that the material is able to straddle the redox potential of water, with the valance band at 1.29 V and conduction band at -1.11 V, and a bandgap of 2.4 eV. IPCE studies revealed that the photoelectrode had an APCE of 3.5%. Water splitting test was conducted in a custom made reactor vessel, where the working electrode and

Pt counter electrode was connected by a single looped wire, without any external bias being applied. This in turn yielded 0.18 μmol/ cm^2 hydrogen after six hours during the first cycle with faradaic efficiency of 30%. To the best of our knowledge this is the first time hydrogen has been produced spontaneously during a water splitting test without any external bias being applied using LFO photoelectrode as a single material. These findings demonstrate that LFO is a potential candidate to act as a photoelectrode for unassisted PEC water splitting to generate solar fuel (hydrogen) cost effectively. However further work is required to investigate and improve slow charge carrier dynamics and low light absorption challenges of LFO photoelectrodes. This can be done by incorporating plasmonic nanoparticles onto the film structure to trap/ absorb more visible light for enhancing photocurrent, hence enhancing the materials hydrogen evolution capability.

Reference

(1) Abe, R. Recent Progress on Photocatalytic and Photoelectrochemical Water Splitting under Visible Light Irradiation. *J. Photochem. Photobiol. C Photochem. Rev.* **2010**, *11* (4), 179–209.

(2) Tachibana, Y.; Vayssieres, L.; Durrant, J. R. Artificial Photosynthesis for Solar Water-Splitting. *Nat. Photonics* **2012**, *6* (8), 511–518.

(3) Huang, Q.; Ye, Z.; Xiao, X. Recent Progress in Photocathodes for Hydrogen Evolution. *J. Mater. Chem. A* **2015**, *3*, 15824–15837.

(4) Zhao, Y.; Hoivik, N.; Wang, K. Recent Advance on Engineering Titanium Dioxide Nanotubes for Photochemical and Photoelectrochemical Water Splitting. *Nano Energy* **2016**, *30*, 728–744.

(5) Fujishima, a; Honda, K. Electrochemical Photolysis of Water at a Semiconductor Electrode. *Nature* **1972**, *238* (5358), 37–38.

(6) Luo, J.; Steier, L.; Son, M. K.; Schreier, M.; Mayer, M. T.; Gratzel, M. Cu2O Nanowire Photocathodes for Efficient and Durable Solar Water Splitting. *Nano Lett.* **2016**, *16* (3), 1848–1857.

(7) Yu, Q.; Meng, X.; Wang, T.; Li, P.; Liu, L.; Chang, K.; Liu, G.; Ye, J. Highly Durable P-LaFeO3/n-Fe2O3 Photocell for Effective Water Splitting under Visible Light. *Chem. Commun.* **2015**, *51*.

(8) Hu, S.; Wang, B.; Zhu, M.; Ma, Y.; Lv, Z.; Wang, H. High-Performance 1D Type-II TiO2@ZnO Core-Shell Nanorods Arrays Photoanodes for Photoelectrochemical Solar Fuel Production. *Appl. Surf. Sci.* **2017**, *403*, 126–132.

(9) Suzuki, T. M.; Saeki, S.; Sekizawa, K.; Kitazumi, K.; Takahashi, N.; Morikawa, T. Photoelectrochemical Hydrogen Production by Water

Splitting over Dual-Functionally Modified Oxide: P-Type N-Doped Ta2O5 Photocathode Active under Visible Light Irradiation. *Appl. Catal. B Environ.* **2017**, *202*, 597–604.

(10) Basu, M.; Zhang, Z. W.; Chen, C. J.; Lu, T. H.; Hu, S. F.; Liu, R. S. CoSe2 Embedded in C3N4: An Efficient Photocathode for Photoelectrochemical Water Splitting. *ACS Appl. Mater. Interfaces* **2016**, *8* (40), 26690–26696.

(11) Septina, W.; Gunawan; Ikeda, S.; Harada, T.; Higashi, M.; Abe, R.; Matsumura, M. Photosplitting of Water from Wide-Gap Cu(in,Ga)S<inf>2</Inf> Thin Films Modified with a CdS Layer and Pt Nanoparticles for a High-Onset-Potential Photocathode. *J. Phys. Chem. C* **2015**, *119* (16), 8576–8583.

(12) Li, J.; Pan, X.; Xu, Y.; Jia, L.; Yi, X.; Fang, W. Synergetic Effect of Copper Species as Cocatalyst on LaFeO3 for Enhanced Visible-Light Photocatalytic Hydrogen Evolution. *Int. J. Hydrogen Energy* **2015**, *40* (40), 13918–13925.

(13) Hoang, S.; Berglund, S. P.; Hahn, N. T.; Bard, A. J.; Mullins, C. B. Enhancing Visible Light Photo-Oxidation of Water with TiO 2 Nanowire Arrays via Cotreatment with H 2 and NH 3: Synergistic Effects between Ti 3+ and N. *J. Am. Chem. Soc.* **2012**, *134* (8), 3659–3662.

(14) Chen, H. M.; Chen, C. K.; Chang, Y.-C.; Tsai, C.-W.; Liu, R.-S.; Hu, S.-F.; Chang, W.-S.; Chen, K.-H. Quantum Dot Monolayer-Sensitized ZnO Nanowire-Array Photoelectrodes: True Efficiency for Water Splitting. *Angew. Chemie Int. Ed.* **2010**, No. 122, 6102–6105.

(15) Wang, G.; Ling, Y.; Wang, H.; Yang, X.; Wang, C.; Zhang, J. Z.; Li, Y.

Hydrogen-Treated WO3 Nanoflakes Show Enhanced Photostability. *Energy Environ. Sci.* **2012**, *5* (3), 6180.

(16) Tahir, A. A.; Upul Wijayantha, K. G.; Saremi-Yarahmadi, S.; Maznar, M.; McKee, V. Nanostructured ??-Fe2O3 Thin Films for Photoelectrochemical Hydrogen Generation. *Chem. Mater.* **2009**, *21* (16), 3763–3772.

(17) Hisatomi, T.; Dotan, H.; Stefik, M.; Sivula, K.; Rothschild, A.; Grätzel, M.; Mathews, N. Enhancement in the Performance of Ultrathin Hematite Photoanode for Water Splitting by an Oxide Underlayer. *Adv. Mater.* **2012**, *24* (20), 2699–2702.

(18) Zhong, D. K.; Choi, S.; Gamelin, D. R. Near-Complete Suppression of Surface Recombination in Solar Photoelectrolysis by “Co-Pi” Catalyst-Modified W:BiVO4. *J. Am. Chem. Soc.* **2011**, *133* (45), 18370–18377.

(19) Sun, J.; Liu, C.; Yang, P. Surfactant-Free, Large-Scale, Solution-Liquid-Solid Growth of Gallium Phosphide Nanowires and Their Use for Visible-Light-Driven Hydrogen Production from Water Reduction. *J. Am. Chem. Soc.* **2011**, *133* (48), 19306–19309.

(20) Li, Y.; Takata, T.; Cha, D.; Takanabe, K.; Minegishi, T.; Kubota, J.; Domen, K. Vertically Aligned Ta3N5 Nanorod Arrays for Solar-Driven Photoelectrochemical Water Splitting. *Adv. Mater.* **2013**, *25* (1), 125–131.

(21) Higashi, M.; Domen, K.; Abe, R. Highly Stable Water Splitting on Oxynitride TaON Photoanode System under Visible Light Irradiation. *J. Am. Chem. Soc.* **2012**, *134* (16), 6968–6971.

(22) Nail, B. A.; Fields, J. M.; Zhao, J.; Wang, J.; Greaney, M. J.; Brutchey,

R. L.; Osterloh, F. E. Nickel Oxide Particles Catalyze Photochemical Hydrogen Evolution from Water；Nanoscaling Promotes P‑Type Character and Minority Carrier Extraction. *ACS Nano* **2015**, *9* (5), 5135–5142.

(23) Ida, S.; Yamada, K.; Matsunaga, T.; Hagiwara, H.; Matsumoto, Y.; Ishihara, T. Preparation of P-Type CaFe2O4 Photocathodes for Producing Hydrogen from Water. *J. Am. Chem. Soc.* **2010**, *132* (49), 17343–17345.

(24) Paracchino, A.; Laporte, V.; Sivula, K.; Grätzel, M.; Thimsen, E. Highly Active Oxide Photocathode for Photoelectrochemical Water Reduction. *Nat. Mater.* **2011**, *10* (6), 456–461.

(25) Peerakiatkhajohn, P.; Yun, J.-H.; Wang, S.; Wang, L. Review of Recent Progress in Unassisted Photoelectrochemical Water Splitting: From Material Modification to Configuration Design. *J. Photonics Energy* **2016**, *7* (1), 012006.

(26) Pihosh, Y.; Turkevych, I.; Mawatari, K.; Uemura, J.; Kazoe, Y.; Kosar, S.; Makita, K.; Sugaya, T.; Matsui, T.; Fujita, D.; Tosa, M.; Kondo, M.; Kitamori, T. Photocatalytic Generation of Hydrogen by Core-Shell WO3/BiVO4 Nanorods with Ultimate Water Splitting Efficiency. *Sci. Rep.* **2015**, *5* (February), 1–10.

(27) Kim, J. Y.; Magesh, G.; Youn, D. H.; Jang, J. W.; Kubota, J.; Domen, K.; Lee, J. S. Single-Crystalline, Wormlike Hematite Photoanodes for Efficient Solar Water Splitting. *Sci. Rep.* **2013**, *3*, 1–8.

(28) Li, F. tang; Liu, Y.; Liu, R. hong; Sun, Z. min; Zhao, D. shun; Kou, C. guang. Preparation of Ca-Doped LaFeO3 Nanopowders in a Reverse

Microemulsion and Their Visible Light Photocatalytic Activity. *Mater. Lett.* **2010**, *64* (2), 223–225.

(29) Li, S.; Jing, L.; Fu, W.; Yang, L.; Xin, B.; Fu, H. Photoinduced Charge Property of Nanosized Perovskite-Type LaFeO3 and Its Relationships with Photocatalytic Activity under Visible Irradiation. *Mater. Res. Bull.* **2007**, *42* (2), 203–212.

(30) Tijare, S. N.; Joshi, M. V.; Padole, P. S.; Mangrulkar, P. A.; Rayalu, S. S.; Labhsetwar, N. K. Photocatalytic Hydrogen Generation through Water Splitting on Nano-Crystalline LaFeO3 Perovskite. *Int. J. Hydrogen Energy* **2012**, *37* (13), 10451–10456.

(31) Dhinesh Kumar, R.; Thangappan, R.; Jayavel, R. Synthesis and Characterization of LaFeO3/TiO2 Nanocomposites for Visible Light Photocatalytic Activity. *J. Phys. Chem. Solids* **2017**, *101* (September 2016), 25–33.

(32) Perednis, D.; Gauckler, L. J. Thin Film Deposition Using Spray Pyrolysis. *J. Electroceramics* **2005**, *14*, 103–111.

(33) Sebastian, T.; Jayakrishnan, R.; Kartha, C. S.; Vijayakumar, K. P. Characterization of Spray Pyrolysed CuInS2 Thin Films. *Surf. Sci.* **2009**, *1*, 1–6.

(34) Popa, M.; Frantti, J.; Kakihana, M. Lanthanum Ferrite LaFeO3+d Nanopowders Obtained by the Polymerizable Complex Method. *Solid State Ionics* **2002**, *154–155*, 437–445.

(35) Romero, M.; Gómez, R. W.; Marquina, V.; Pérez-Mazariego, J. L.; Escamilla, R. Synthesis by Molten Salt Method of the AFeO3 System (A=La, Gd) and Its Structural, Vibrational and Internal Hyperfine

Magnetic Field Characterization. *Phys. B Condens. Matter* **2014**, *443*, 90–94.

(36) Kamimura, J.; Bogdanoff, P.; Abdi, F. F.; Lähnemann, J.; Van De Krol, R.; Riechert, H.; Geelhaar, L. Photoelectrochemical Properties of GaN Photoanodes with Cobalt Phosphate Catalyst for Solar Water Splitting in Neutral Electrolyte. *J. Phys. Chem. C* **2017**, *121* (23), 12540–12545.

(37) Peter, L. M.; Wijayantha, K. G. U. Electron Transport and Back Reaction in Dye Sensitised Nanocrystalline Photovoltaic Cells. *Electrochim. Acta* **2000**, *45* (28), 4543–4551.

(38) Hernández, S.; Barbero, G.; Saracco, G.; Alexe-Ionescu, A. L. Considerations on Oxygen Bubble Formation and Evolution on BiVO<inf>4</Inf> Porous Anodes Used in Water Splitting Photoelectrochemical Cells. *J. Phys. Chem. C* **2015**, *119* (18), 9916–9925.

(39) Lopes, T.; Andrade, L.; Le Formal, F.; Gratzel, M.; Sivula, K.; Mendes, A. Hematite Photoelectrodes for Water Splitting: Evaluation of the Role of Film Thickness by Impedance Spectroscopy. *Phys. Chem. Chem. Phys.* **2014**, *16* (31), 16515.

(40) Tahir, A. A.; Wijayantha, K. G. U. Photoelectrochemical Water Splitting at Nanostructured ZnFe2O4 Electrodes. *J. Photochem. Photobiol. A Chem.* **2010**, *216* (2–3), 119–125.

(41) Kumar, M. H.; Mathews, N.; Boix, P. P.; Nonomura, K.; Powar, S.; Ming, L. Y.; Graetzel, M.; Mhaisalkar, S. G. Decoupling Light Absorption and Charge Transport Properties in near IR-Sensitized Fe2O3 Regenerative Cells. *Energy Environ. Sci.* **2013**, *6* (11), 3280.

(42) Cho, S.; Coates, N.; Moon, J. S.; Park, S. H.; Roy, A.; Beaupre, S.; Moses, D.; Leclerc, M.; Lee, K.; Heeger, A. J. Bulk Heterojunction Solar Cells with Internal Quantum Efficiency Approaching 100. *Nat. Photonics* **2009**, *3* (5), 297–302.

(43) Viezbicke, B. D.; Patel, S.; Davis, B. E.; Birnie, D. P. Evaluation of the Tauc Method for Optical Absorption Edge Determination: ZnO Thin Films as a Model System. *Phys. Status Solidi* **2015**, *252* (8), 1700–1710.

(44) Ghobadi, N. Band Gap Determination Using Absorption Spectrum Fitting Procedure. *Int. Nano Lett.* **2013**, *3* (1), 2.

(45) Phokha, S.; Pinitsoontorn, S.; Maensiri, S.; Rujirawat, S. Structure, Optical and Magnetic Properties of LaFeO3 Nanoparticles Prepared by Polymerized Complex Method. *J. Sol-Gel Sci. Technol.* **2014**, *71* (2), 333–341.

(46) Gelderman, K.; Lee, L.; Donne, S. W. Flat-Band Potential of a Semiconductor: Using the Mott–Schottky Equation. *J. Chem. Educ.* **2007**, *84* (4), 685.

(47) Gómez-Solís, C.; Ballesteros, J. C.; Torres-Martínez, L. M.; Juárez-Ramírez, I. RuO2-NaTaO3 Heterostructure for Its Application in Photoelectrochemical Water Splitting under Simulated Sunlight Illumination. *Fuel* **2016**, *166*, 36–41.

(48) Azumi, K.; Ohtsuka, T.; Sato, N. Mott-Schottky Plot of the Passive Film Formed on Iron in Neutral Borate and Phosphate Solutions. *J. Electrochem. Soc.* **1987**, *134* (6), 1352–1357.

(49) Qiu, Y.; Luo, Y. S.; Zou, Z. J.; Tian, Z. M.; Yuan, S. L.; Xi, Y.; Huang, L.

Z. Size Effect on Magnetic and Dielectric Properties in Nanocrystalline LaFeO3. *J. Mater. Sci. Mater. Electron.* **2014**, *25* (2), 760–764.

6.2 Synthesis of $LaFeO_3$ – Ag Photoelectrodes for Plasmonically Enhanced Solar Hydrogen Generation

The work done in this section is done with our collaborators. The aim was to incorporate plasmonic silver nanoparticles on to our LFO electrodes to make LFO-Ag, for enhanced current and hydrogen performance. Our collaborators provided FDTD simulations to find out the best particle size range for best performance. My contribution to this work was to prepare and fabricate LFO-Ag, characterise and test them.

6.2.1 Introduction

Hydrogen is a promising alternative fuel capable of replacing fossil fuels as a primary source of energy as it has high energy density (140 MJ kg^{-1}), far exceeding that of fossil fuels, zero carbon emission and the only by-product from combustion is water.[1] Current methods of hydrogen production in industry are as follows: hydrocarbon reforming, hydrogen from biomass and electrolysis. These methods however have some disadvantages. In hydrocarbon reforming process; carbon monoxide is released as a by-product. Biomass gasification suffers from low thermal efficiency and any addition of steam or oxygen results in steam reforming leading to the production of carbon monoxide. Electrolysis of water requires an electric current, which is provided by fossil fuels from the electrical grid, to break down water into its constituents (O_2 and H_2).[2] Photoelectrochemical (PEC) water splitting is widely recognized as one of the most promising approach for large scale solar energy conversion to storable fuels (hydrogen).[3–6]

$LaFeO_3$ (LFO) photocathode has been fabricated by a novel, cost effective and scalable spray pyrolysis method and has demonstrated hydrogen generation, from solar water splitting, without any applied external bias[7]. However, its photocurrent is relatively low when compared to other metal oxide semiconductors, for example Cu_2O,[8] due to its low light absorption properties.

Surface Plasmon Resonance (SPR) has been considered as one of the best strategies to improve light harvesting capabilities of semiconductor materials.[9,10] Noble metals (e.g. gold[11–14] and silver[10,15]) have the potential of enhancing optical absorption and scattering by excitation of SPR, thus improving light harvesting capabilities. Light-driven oscillations of conduction electrons cause oscillating dipoles and the right wavelengths excite strong SPR in metallic nanoparticles.[16] SPR in smaller nanoparticles results in higher surface electro-magnetic fields and hence higher scattering cross-section, much larger than geometric cross-section[17]. The enhanced electromagnetic field is dependent upon the wavelength of incident light, shape, size and aggregation state of the nanoparticles.[18] There are three mechanisms of plasmon-enhanced solar energy conversion: 1) light scattering/ trapping, 2) hot electron injection and 3) plasmon-induced resonance energy transfer (PIRET).[19,20] When plasmonic metal nanoparticles are integrated with a semiconductor material, the incident light can be effectively scattered by the metal nanoparticles. Due to this scattering effect, enhanced light absorption and charge separation occur in the active semiconductor material. In hot electron injection, non-radiative dissipation of plasmon energy is capable of generating hot carriers via Landau damping. The hot electrons, which have energy higher than the Schottky barrier at the metal/ semiconductor interface, can be directly injected into the conduction band of the semiconductor. To maximise the hot electron injection effect, it is essential to keep close contact between metal and semiconductor. In the PIRET mechanism, the excited plasmon in a metal is able to generate a strong dipole. The plasmonic energy in the metal can be non-radiatively transferred to the semiconductor via the dipole-dipole interaction in the near field, generating electron/ hole pairs in the semiconductor material. PIRET is strongly dependent on two factors: 1) distance between the energy donor (metal) and energy acceptor (semiconductor), and 2) the spectral overlap between plasmonic resonance band and the semiconductor's absorption band. Therefore, plasmonic nanoparticles can be used as photosensitizers for semiconductors to significantly extend the light absorption spectral range. Silver (Ag) is of particular interest of the noble metals due to its lower cost (compared to gold) and controllable size. Enhanced optical absorption and enhanced photocurrent by applying silver nanoparticles (Ag nanoparticles), giving rise to surface plasmons, have been applied to silicon solar cells[21–24],dye-sensitized solar cells[9,18,25–28] and for hydrogen production from water splitting.[10,15] Along with plasmonic nanoparticles, quantum dots can also help improve charge carrier dynamics.[29]

Here, we report an approach towards enhanced photocurrent and hydrogen evolution capabilities of LFO photocathode, by incorporating Ag nanoparticles to provide a plasmonic enhanced LFO-Ag photocathode nanocomposite. To the best of our knowledge, this is the first time LFO-Ag photocathode has been fabricated to show enhanced photoactivity and hydrogen yield. Finite

Difference Time Domain (FDTD) simulations are employed to simulate the SPR resonances of Ag nano particles. The FDTD simulations show that the Ag nanoparticles with diameters in the range of 50 - 80 nm demonstrate strong SPR effect suitable for incorporation with LFO photocathodes. Experimentally, these nanoparticles show enhanced light extraction capabilities. This in turn gives rise to an increased photocurrent and hydrogen yield, where it more than doubles when Ag nanoparticles are incorporated in to the LFO films.

6.2.2 Experimental

The full experimental details for LFO-Ag is given in chapter 5.

6.2.3 Results and Discussion

Optimised nanostructured LFO films were synthesised by spray pyrolysis (SP) as discussed in section 5.1. FDTD simulations were conducted by our collaborators to determine the best Ag particle size for best performance. Once they provided the data for best Ag particle size, we optimised the concentration of Ag nanoparticles to incorporate into the LFO photoelectrode by spin coating method to create LFO-Ag photoelectrodes. A comparative study between varying LFO-Ag nanoparticle concentration and plain LFO on PEC performance is studied.

6.2.3.1 Finite Difference Time Domain Simulation

As mentioned the FDTD simulations were conducted by our collaborators where they used this technique to study the spectral response of Ag nanoparticles with varying particle size, to determine the optimal particle size for optimal performance.

Figure 54 (a) to 54 (f) show the extinction, absorption and scattering cross-sections of Ag nanoparticles with increasing diameter. The results show that both absorption and scattering cross-section increases with increase in diameter of Ag nanoparticles and the nanoparticles of diameters greater than 50 nm show a greater scattering component compared to absorption. This trend can be explained by noting that the absorption and scattering cross-sections are proportional to the cube and sixth power of diameter of nanoparticle respectively[30] and hence scattering dominates in larger nanoparticles. As the diameter of nanoparticles increase, the SPR peak broadens and experiences a red shift[31]. Red shift of the SPR peak is due to the weakening of the restoring force with increasing size of the nanoparticle[32]. A secondary peak becomes visible at lower wavelengths in addition to the primary peak for diameters greater than 80 nm (figure 54 (d)). Quadrupole resonances cause these secondary peaks which has a different electron oscillation pattern.[33–35] Though scattering increases with size, for our application, it is not recommended to use nanoparticles of sizes > 90 nm as these will have lower surface area to volume ratio and they tend to form larger aggregates. Hence, normalized scattering cross-section (scattering cross-section normalized to nanoparticle geometric cross-sectional area[17]) is calculated for Ag nanoparticles of diameter 40 nm to 80 nm with a step of 10 nm. Figure 54 (f) shows that initially, as the size of the Ag NP increases the normalized scattering cross-section increases, reaches a maximum value and then slightly decreases. Results show that for nanoparticle of size 70 nm, the best performing nanoparticle for light scattering, normalized scattering cross-section reaches 6.4 and in the diameter range of 50 – 80 nm its greater than 5.

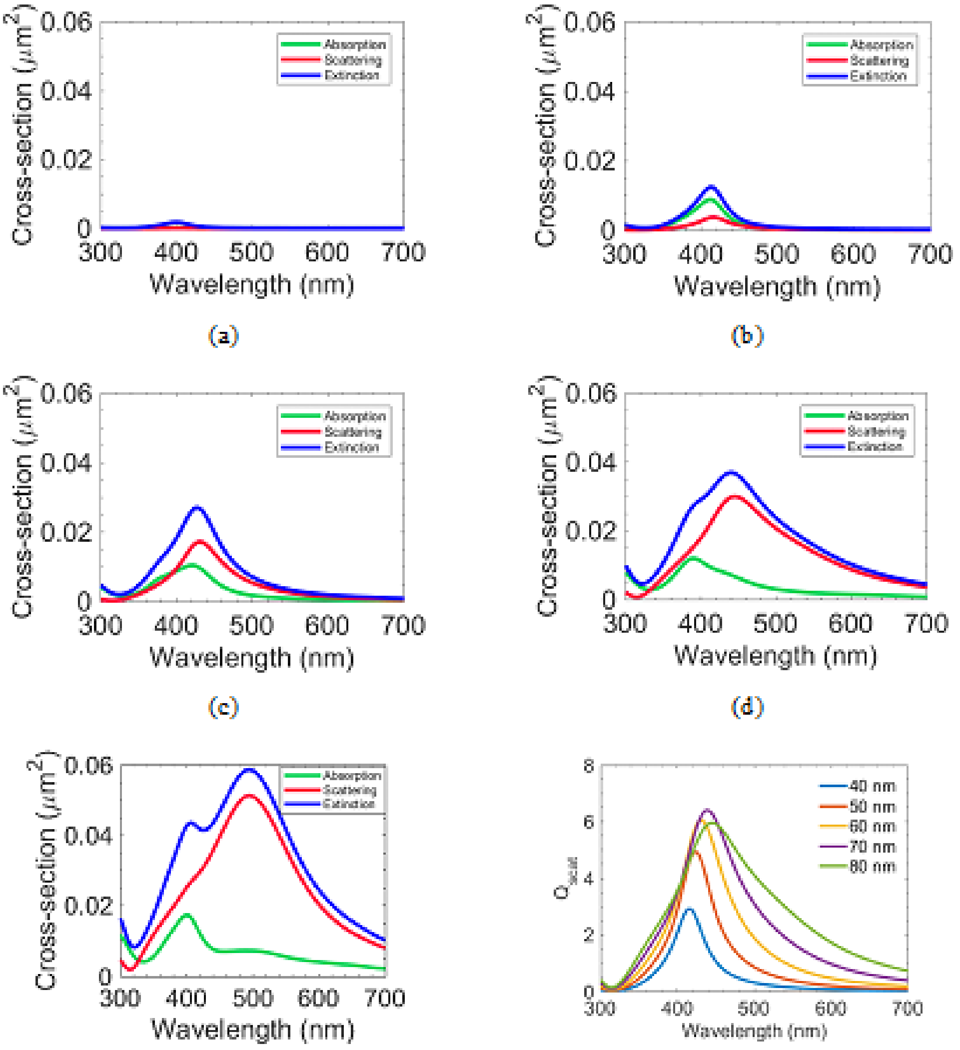

(a) (b) (c) (d) (e) (f)

Figure 54: Extinction, absorption and scattering cross-sections of Ag nanoparticles of diameters (a) 20 nm (b) 40 nm (c) 60 nm (d) 80 nm (e) 100 nm (f) normalized scattering cross-sections of Ag nanoparticles for diameters of 40-80 nm.

6.2.3.2 PEC Performance and Characterisation of LFO-Ag Photoelectrode

The LFO films were prepared by using the optimised spraying parameters discussed in section 5.1, where the precursor solution is sprayed at 150ºC and then post-annealed at 550ºC to obtain single phase crystalline material. The optimized size range from theoretical modelling is 50-80 nm and the same range is used in fabrication of the LFO-Ag photoelectrode. Ag nanoparticles at varying concentration (1.5 mmol, 0.77 mmol, 0.37 mmol, 0.19 mmol and 0.1 mmol) were first prepared as described in section 4.1.4.1 by suspending the particles in acetone. LFO-Ag (1.5 mmol), LFO-Ag (0.77 mmol), LFO-Ag (0.37 mmol), LFO-Ag (0.19 mmol) and LFO-Ag (0.1 mmol) were fabricated by simple and inexpensive spin coating method described in section 4.1.4.3. The different LFO-Ag photoelectrodes were fabricated to determine the optimum concentration of Ag nanoparticles needed to give the best performance. The PEC performance of the LFO-Ag films were performed in 0.1 M aqueous NaOH (pH 13) solution by illuminating the photocathode from the electrolyte side (represented in figure 55) to evaluate the current density, compared to plain LFO photocathode. The photocurrent density (J) is plotted against bias potential (V) as shown in figure 56. The untreated LFO photocathode exhibited a current density of 0.036 mA/cm^2 at 0.6 V vs RHE. Upon incorporating the 0.77 mmol Ag nanoparticles there is a distinct improvement in the current density reaching 0.061 mA/cm^2 at 0.6 V vs RHE due to the plasmonic enhancement. On increasing the concentration of Ag nanoparticles, there is a slight decrease in current density to a value of 0.059 mA/cm^2 as at 0.6 V vs RHE is observed. This will be due to the higher content of Ag nanoparticles on the film surface reducing the electrode/electrolyte interface inhibiting effective charge separation, thus decreasing the amount of current density. As the concentration of the Ag nanoparticles is reduced up to 0.19 mmol, the current density is increased significantly to 0.074 mA/cm^2, an improvement of >2x, compared to the current achieved in a bare $LaFeO_3$ photocathode. At this concentration, a near optimum amount of Ag nanoparticles are incorporated into the film as an optimal current density is achieved, with minimal amount of Ag nanoparticles blocking the electrode/electrolyte interface and achieving the optimum plasmonic effect. Furthermore, dilution to 0.1 mmol sees a drop in current density where it reaches 0.056 mA/cm^2 at 0.6 V vs RHE. As the Ag nanoparticles content decreases further, lower amount of light is trapped for plasmonic resonance, hence there is a drop in current density compared to 0.19 mmol Ag NP concentration.

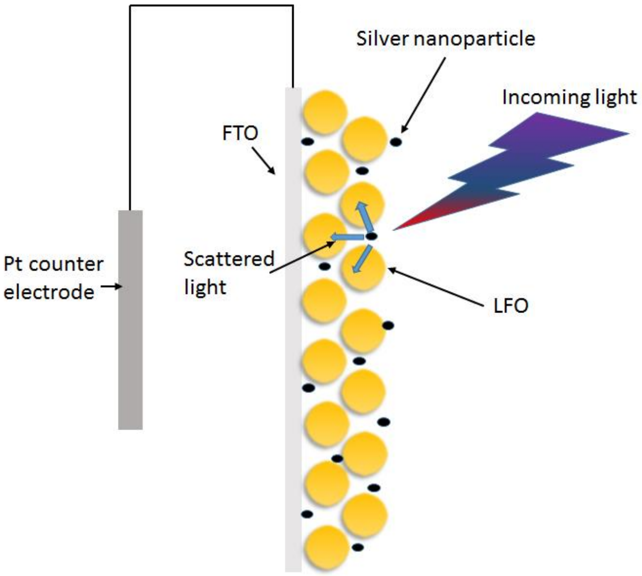

Figure 55: Image depicting the LFO-Ag working electrode being illuminated where the Ag nanoparticles scatter the light.

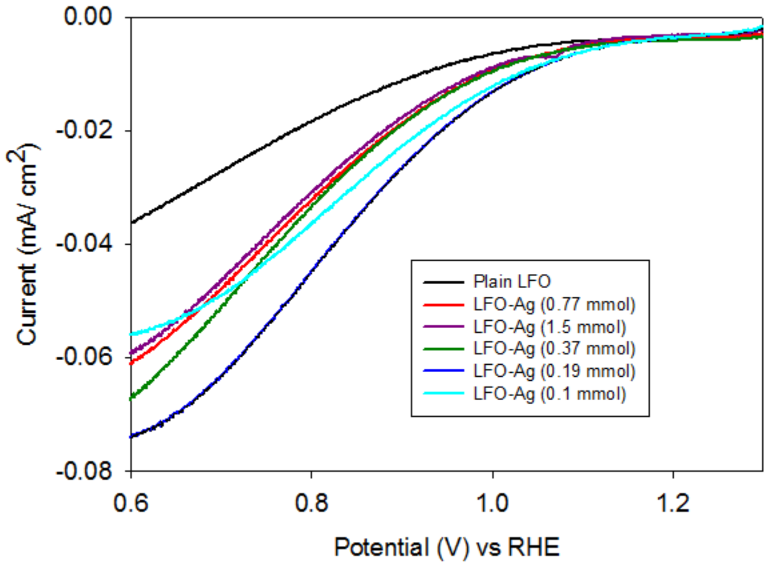

Figure 56: J-V characteristics of plain LFO and various LFO-Ag concentrations in a 0.1 M NaOH electrolyte vs RHE.

A chronoamperometry test was conducted for the best performing LFO-Ag (0.19 mmol) photocathode to determine its stability. Figure 57 shows the stability of LFO-Ag (0.19 mmol) over a 24 hour period under a continuous 1 sun illumination in 0.1 M NaOH electrolyte solution. The material shows excellent stability over the 24 hour period, reaching a maximum current density of 0.15 mA after 10 hours. At 24 hours there was a slight drop in current density of 5 %. The slight decrease in current density will be due to gas bubble accumulation on the films surface. This will decrease the effective area, increasing the interfacial electrical resistance which causes the slight current drop.[7,36]

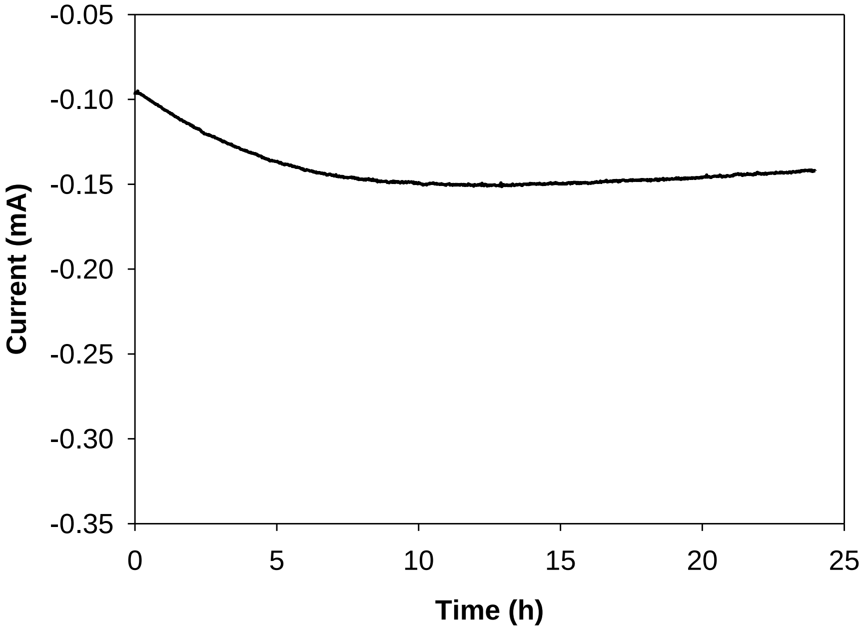

Figure 57: Chronoamperometry test of LFO-Ag (0.19 mmol) under continuous illumination in a 0.1 M NaOH electrolyte at 0 V vs Ag/ AgCl.

As the best performing photoelectrode has been determined as LFO-Ag (0.19 mmol), it is used to identify its crystal phase compared to plain LFO. The XRD peak pattern for both photocathodes are shown in figure 58. The XRD patterns display that the plain LFO films are crystalline with the LFO particles orientated in the (121) plane, which is in good agreement with previous works[7]. All the peaks correspond to LFO are indexed to orthorhombic system (JCPDS 00-037-1493). No Ag diffraction peaks could be clearly identified, which can be attributed to the small particle size, dispersity and low loaded content of Ag nanoparticles. Peaks marked with asterisks correspond to the FTO peaks, distinguishing it from the LFO peaks.

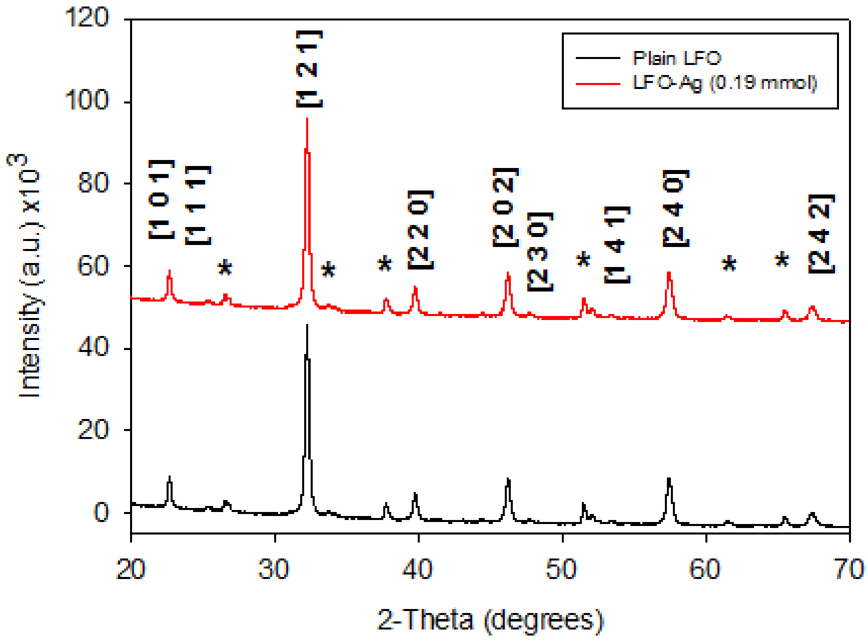

Figure 58: XRD pattern of LFO and LFO-Ag (0.19 mmol) on FTO glass substrate, where the peaks marked with an asterisk represent FTO.

A top view SEM for plain LFO and LFO-Ag (0.19 mmol) was taken to look at its morphology and to compare the two. The plain LFO nanostructured film (figure 59 (a)), and its respective EDS (figure 59 (c)), have well connected crystal grains in a coral like structure, post annealing 550ºC, which is in good agreement with previous study. Its EDX confirms that there is no Ag nanoparticles present in the film. Figure 59 (b) shows the SEM of LFO-Ag (0.19 mmol) and it can be observed that bright spherical nanoparticles are uniformly distributed across the film. These bright spherical particles can be attributed to the Ag nanoparticles as the EDX (figure 59 (d)) confirms the presence of Ag. By comparing the two images, it can be clearly seen that the Ag nanoparticles have been incorporated into the LFO film after spin coating and the current improvement must be due to incorporation of Ag nanoparticles giving rise to SPR effect.

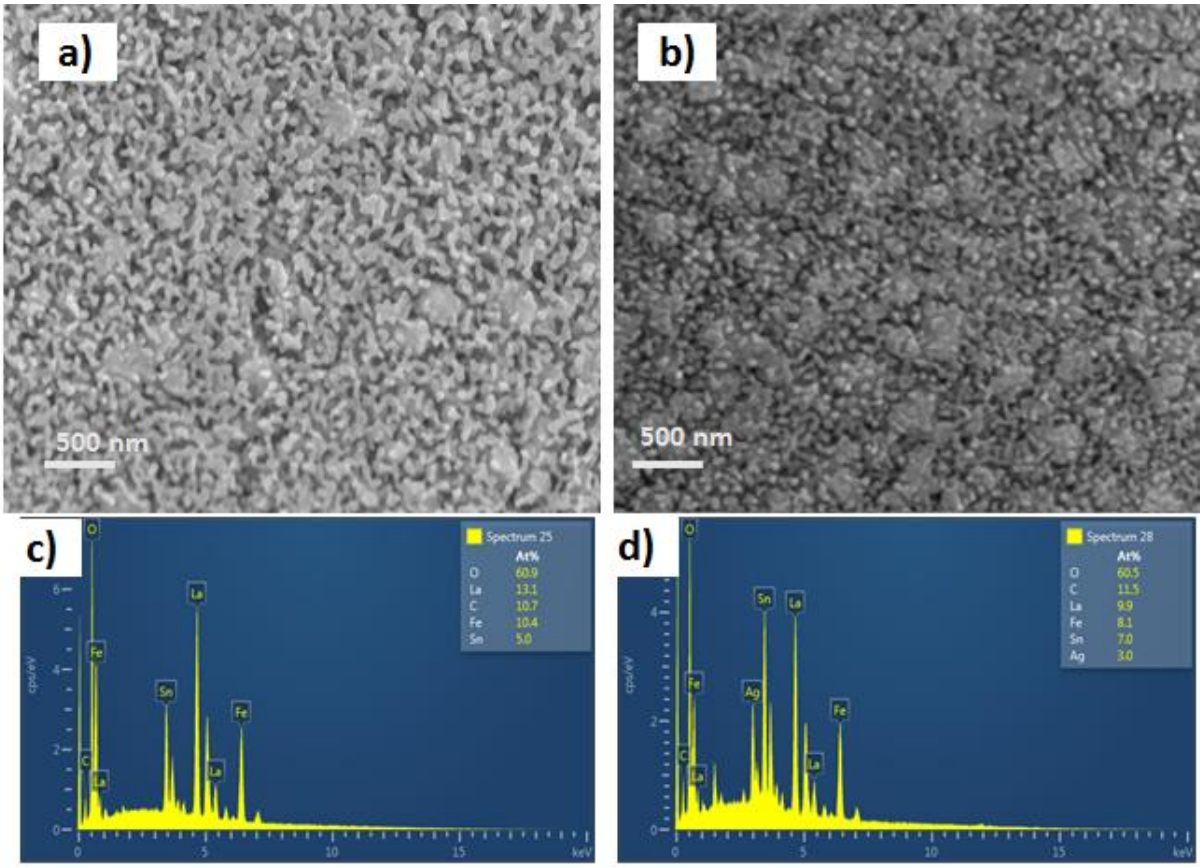

Figure 59: (a) Top view SEM of plain LFO film, (b) top view SEM of LFO-Ag (0.19 mmol), (c) EDS for plain LFO and (d) EDS for LFO-Ag (0.19 mmol).

To understand the effect of Ag nanoparticles on light absorption, its optical properties were measured with UV-Vis spectroscopy. Figure 60 shows the UV-Vis absorption spectra of both plain LFO and LFO-Ag (0.19 mmol) at wavelengths from 360 – 800 nm, and the inset of figure 61 shows all the LFO-Ag UV-Vis absorption. Higher absorption of light in the short wavelength region (400 – 600 nm) and a slight increase in the long wavelength region (600 – 800 nm) was observed for all the LFO-Ag photocathodes, which can be related to the increased scattering of Ag nanoparticles in this frequency range due to SPR effect. It can be noted that the highest Ag concentration provides the lowest increased absorption of light, where when decreasing the Ag concentration more light is absorbed. This can be because there will be more number of Ag nanoparticles within a specific area when concentration is highest compared to lower concentration. Therefore, it will reflect some scattered light away from LFO film as higher Ag concentration is blocking the film due to agglomeration of Ag particles on LFO film surface. When concentration of Ag nanoparticles decreases, the scattered light is directed more towards the LFO film as more of the film is exposed. The optimum concentration for optimum absorbance is 0.19 mmol of Ag nanoparticles. The broad absorption peak observed in the short wavelength region (450 - 500 nm) is due to inhomogeneous size distribution of Ag nanoparticles (50-80 nm) and the peak is slightly blue shifted compared to simulations, which can be due to measurements conducted in air.

The increased absorption shows that the incorporation of Ag nanoparticles effectively enhances the light harvesting when compared to the plain LFO, which is seconded by the increase in current generated in the case of PEC performance (figure 56). Therefore, a higher yield of hydrogen is expected from the solar water splitting experiment as the photocathode potentially absorb more light and generating more current for water splitting.

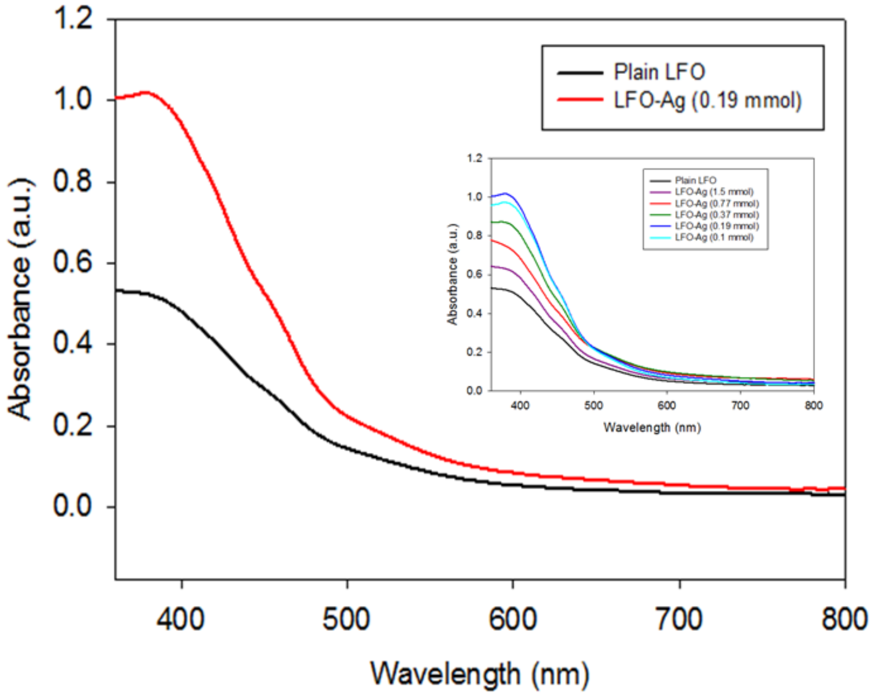

Figure 60: Absorbance spectra of plain LFO and LFO-Ag (0.19 mmol). Inset shows all the absorbance spectra for all the varying concentrations of LFO-Ag photoelectrodes.

6.2.3.3 Hydrogen Evolution Measurement

Figure 61 shows the hydrogen evolution measurement of the plain LFO film and LFO films with various Ag NP concentrations performed in an aqueous 0.1 M NaOH solution under a constant illumination. The water splitting test was conducted in a custom made glass reactor vessel with an attached fused silica viewport. The working electrode and Pt counter electrode were connected by a single looped wire, without any external bias being applied. After three hours, the plain LFO photocathode was spontaneously generating hydrogen, where after six hours it has generated 0.12 μmol/cm^2. All LFO-Ag photocathodes began spontaneously generating hydrogen after one hour.

This is a vast improvement compared to the untreated LFO photocathode. This is due to the enhanced light harvesting from the plasmonic effect from the Ag nanoparticles, leading to higher current density being generated, which is in good agreement with the *J-V* curves. As more light is being absorbed by the film, it generates more electrons which are being converted to hydrogen. The hydrogen generated by the different LFO-Ag photocathode concentrations correlates well with the *J-V* curves. As seen in figure 56, when decreasing the Ag concentration from 0.77 mmol to 0.19 mmol there is an increase in current. As the current increases there is a clear increase in volume of hydrogen generated; where after 6 hours 0.77 mmol Ag generates 0.21 μmol/cm^2, 0.37 mmol Ag generates 0.22 μmol/ cm^2 and 0.19 mmol Ag generates 0.32 μmol/ cm^2. When the Ag nanoparticles concentration was diluted further to 0.1 mmol the current decreased which also led to a decrease in hydrogen to 0.23 μmol/cm^2. Furthermore, an increase in Ag nanoparticles concentration to 1.5 mmol also led to a decrease in hydrogen generation, where after 6 hours 0.17 μmol/cm^2 of hydrogen is produced, though still more than plain LFO. Due to higher content of Ag nanoparticles on the film surface this will reduce the electrode/electrolyte interface lowering effective charge separation.

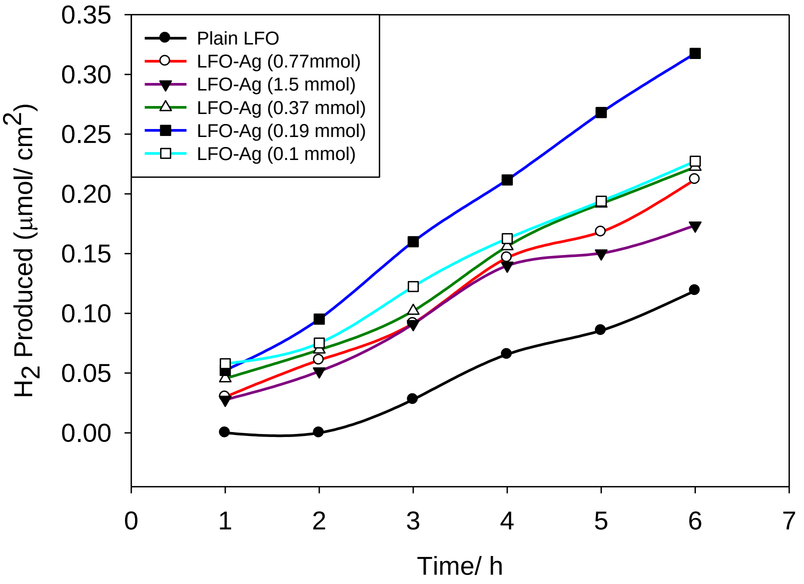

Figure 61: Hydrogen evolution test of plain LFO and LFO-Ag with varying Ag concentrations, in an aqueous 0.1 M NaOH solution.

6.2.4 Conclusion

In summary, we have incorporated optimized Ag nanoparticles (of diameters ranging from 50-80 nm) on to the nanostructured LFO film. The photocathodes show an increase of light absorption upon incorporation of the Ag nanoparticles compared to its untreated counterpart. This agrees well with the FDTD studies (conducted by our collaborators) showing better light harvesting for Ag nanoparticles of sizes ranging from 50 nm to 80 nm. Incorporation of Ag nanoparticles has enhanced the current density, where the best performing LFO-Ag (0.19 mmol) photocathode generated twice the amount of current than the plain LFO photocathode generating a current of 0.074 mA/ cm^2 at 0.6 V vs RHE; due to the plasmonic effect from Ag Nanoparticles. Subsequently, the LFO-Ag (0.19 mmol) photocathode generated over twice the amount of hydrogen than the untreated LFO counterpart, where after six hours it spontaneously produced 0.32 μmol/cm^2 of hydrogen without the need for an external bias. Furthermore, the LFO-Ag photocathodes were able to produce hydrogen after 1 hour of illumination compared to the untreated LFO photocathode, which began forming hydrogen after three hours of illumination. This finding shows that Ag nanoparticles are able to enhance the performance of LFO photocathodes generating a higher volume of hydrogen. Further, studies are required to enhance the performance using nanoparticles of specific diameter and to replace Ag nanoparticles with a lower cost non-precious metal. Ni nanoparticles are a potential candidate as they have shown to have plasmonic effects like that of Ag, but the main advantage of Ni is that it is much more cheaper than Ag.

Reference

(1) Xie, G.; Zhang, K.; Guo, B.; Liu, Q.; Fang, L.; Gong, J. R. Graphene-Based Materials for Hydrogen Generation from Light-Driven Water Splitting. *Adv. Mater.* **2013**, *25* (28), 3820–3839.

(2) Holladay, J. D.; Hu, J.; King, D. L.; Wang, Y. An Overview of Hydrogen Production Technologies. *Catal. Today* **2009**, *139* (4), 244–260.

(3) Alfaifi, B. Y.; Ullah, H.; Alfaifi, S.; Tahir, A. A.; Mallick, T. K. Photoelectrochemical Solar Water Splitting: From Basic Principles to Advanced Devices. *Veruscript Funct. Nanomater.* **2018**, 1–26.

(4) Chen, X.; Shen, S.; Guo, L.; Mao, S. S. Semiconductor-Based Photocatalytic Hydrogen Generation. *Therm. Eng.* **2010**, *110*, 6503–6570.

(5) Tachibana, Y.; Vayssieres, L.; Durrant, J. R. Artificial Photosynthesis for Solar Water-Splitting. *Nat. Photonics* **2012**, *6* (8), 511–518.

(6) Osterloh, F. E. Inorganic Nanostructures for Photoelectrochemical and Photocatalytic Water Splitting. *Chem. Soc. Rev.* **2013**, *42* (6), 2294–2320.

(7) Pawar, G. S.; Tahir, A. A. Unbiased Spontaneous Solar Fuel Production Using Stable LaFeO3 Photoelectrode. *Sci. Rep.* **2018**, *8* (1), 3501.

(8) Luo, J.; Steier, L.; Son, M. K.; Schreier, M.; Mayer, M. T.; Gratzel, M. Cu2O Nanowire Photocathodes for Efficient and Durable Solar Water Splitting. *Nano Lett.* **2016**, *16* (3), 1848–1857.

(9) Jeong, N. C.; Prasittichai, C.; Hupp, J. T. Photocurrent Enhancement by Surface Plasmon Resonance of Silver Nanoparticles in Highly Porous Dye-Sensitized Solar Cells. *Langmuir* **2011**, *27* (23), 14609–14614.

(10) Lian, Z.; Wang, W.; Xiao, S.; Li, X.; Cui, Y.; Zhang, D.; Li, G.; Li, H. Plasmonic Silver Quantum Dots Coupled with Hierarchical TiO<inf>2</Inf> Nanotube Arrays Photoelectrodes for Efficient Visible-Light Photoelectrocatalytic Hydrogen Evolution. *Sci. Rep.* **2015**, *5* (April), 1–10.

(11) Zhang, Z.; Zhang, L.; Hedhili, M. N.; Zhang, H.; Wang, P. Plasmonic Gold Nanocrystals Coupled with Photonic Crystal Seamlessly on TiO $_2$ Nanotube Photoelectrodes for Efficient Visible Light Photoelectrochemical Water Splitting. *Nano Lett.* **2013**, *13* (1), 14–20.

(12) Chen, J.-J.; Wu, J. C. S.; Wu, P. C.; Tsai, D. P. Plasmonic Photocatalyst for H 2 Evolution in Photocatalytic Water Splitting. *J. Phys. Chem. C* **2011**, *115* (1), 210–216.

(13) Hu, K.; Chen, H.; Jiang, M.; Teng, F.; Zheng, L.; Fang, X. Broadband Photoresponse Enhancement of a High-Performance t-Se Microtube Photodetector by Plasmonic Metallic Nanoparticles. *Adv. Funct. Mater.* **2016**, *26* (36), 6641–6648.

(14) Chen, H.; Su, L.; Jiang, M.; Fang, X. Highly Desirable Photodetectors Derived from Versatile Plasmonic Nanostructures. *Adv. Funct. Mater.* **2017**, *27* (45), 1–17.

(15) Hu, X.; Xiao, L.; Jian, X.; Zhou, W. Synthesis of Mesoporous Silica-Embedded TiO2 Loaded with Ag Nanoparticles for Photocatalytic Hydrogen Evolution from Water Splitting. *J. Wuhan Univ. Technol. Sci. Ed.* **2017**, *32* (1), 67–75.

(16) Si, Lifang; Qiu, Teng; Zhang, Wenjun; K. Chu, P. Recent Progress in Design of Plasmonic Thin-Film Solar Cells with Enhanced Efficiency.

Recent Patents Mater. Sci. **2012**, *5* (2), 166–172.

(17) Paul, H.; Fischer, R. How Can a Particle Absorb More than the Light Incident on It? *Am. J. Phys.* **1983**, *51* (4), 323–327.

(18) Luan, X.; Wang, Y. Plasmon-Enhanced Performance of Dye-Sensitized Solar Cells Based on Electrodeposited Ag Nanoparticles. *J. Mater. Sci. Technol.* **2014**, *30* (1), 1–7.

(19) Wu, N. Plasmonic Metal-Semiconductor Photocatalysts and Photoelectrochemical Cells: A Review. *Nanoscale* **2018**, *10* (6), 2679–2696.

(20) Cushing, S. K.; Wu, N. Progress and Perspectives of Plasmon-Enhanced Solar Energy Conversion. *J. Phys. Chem. Lett.* **2016**, *7* (4), 666–675.

(21) Schaadt, D. M.; Feng, B.; Yu, E. T. Enhanced Semiconductor Optical Absorption via Surface Plasmon Excitation in Metal Nanoparticles. *Appl. Phys. Lett.* **2005**, *86* (6), 1–3.

(22) Stuart, H. R.; Hall, D. G. Island Size Effects in Nanoparticle Enhanced Photodetectors. *Appl Phys Lett* **1998**, *73* (26), 3815–3817.

(23) Pillai, S.; Catchpole, K. R.; Trupke, T.; Green, M. A. Surface Plasmon Enhanced Silicon Solar Cells. *J. Appl. Phys.* **2007**, *101* (9).

(24) Basch, A.; Beck, F. J.; Söderström, T.; Varlamov, S.; Catchpole, K. R. Combined Plasmonic and Dielectric Rear Reflectors for Enhanced Photocurrent in Solar Cells. *Appl. Phys. Lett.* **2012**, *100* (24).

(25) Qi, J.; Dang, X.; Hammond, P. T.; Belcher, A. M. Highly Efficient Plasmon-Enhanced Dye-Sensitized Solar Cells through Metal@oxide Core-Shell Nanostructure. *ACS Nano* **2011**, *5* (9), 7108–7116.

(26) Guo, K.; Li, M.; Fang, X.; Liu, X.; Sebo, B.; Zhu, Y.; Hu, Z.; Zhao, X. Preparation and Enhanced Properties of Dye-Sensitized Solar Cells by Surface Plasmon Resonance of Ag Nanoparticles in Nanocomposite Photoanode. *J. Power Sources* **2013**, *230*, 155–160.

(27) Gangishetty, M. K.; Lee, K. E.; Scott, R. W.; Kelly, T. L. Plasmonic Enhancement of Dye Sensitized Solar Cells in the Red-to-near-Infrared Region Using Triangular Core-Shell Ag@SiO2 Nanoparticles. *ACS Appl Mater Interfaces* **2013**, *5* (21), 11044–11051.

(28) Ihara, M.; Kanno, M.; Inoue, S. Photoabsorption-Enhanced Dye-Sensitized Solar Cell by Using Localized Surface Plasmon of Silver Nanoparticles Modified with Polymer. *Phys. E Low-Dimensional Syst. Nanostructures* **2010**, *42* (10), 2867–2871.

(29) Han, S. C.; Pu, Y. C.; Zheng, L. X.; Hu, L. F.; Zhang, J. Z.; Fang, X. S. Uniform Carbon-Coated CdS Core-Shell Nanostructures: Synthesis, Ultrafast Charge Carrier Dynamics, and Photoelectrochemical Water Splitting. *J. Mater. Chem. A* **2016**, *4* (3), 1078–1086.

(30) Hlaing, M.; Gebear-Eigzabher, B.; Roa, A.; Marcano, A.; Radu, D.; Lai, C. Y. Absorption and Scattering Cross-Section Extinction Values of Silver Nanoparticles. *Opt. Mater. (Amst).* **2016**, *58*, 439–444.

(31) Göeken, K. L.; Subramaniam, V.; Gill, R. Enhancing Spectral Shifts of Plasmon-Coupled Noble Metal Nanoparticles for Sensing Applications. *Phys. Chem. Chem. Phys.* **2015**, *17* (1), 422–427.

(32) Fan, X.; Zheng, W.; Singh, D. J. Light Scattering and Surface Plasmons on Small Spherical Particles. *Light Sci. Appl.* **2014**, *3* (March), 1–14.

(33) Steven J. Oldenburg. Silver Nanoparticle Dispersions from Aldrich

Materials Science. *Silver Nanoparticles Prop. Appl.* **2014**, No. 730793, 2–5.

(34) Jain, P.; Aggarwal, V. Synthesis, Characterization and Antimicrobial Effects of Silver Nanoparticles from Microorganisms-A Review. *Int. J. Nano Mater. Sci.* **2012**, *1* (12), 108–120.

(35) Vidhu, V. K.; Philip, D. Catalytic Degradation of Organic Dyes Using Biosynthesized Silver Nanoparticles. *Micron* **2014**, *56*, 54–62.

(36) Hernández, S.; Barbero, G.; Saracco, G.; Alexe-Ionescu, A. L. Considerations on Oxygen Bubble Formation and Evolution on BiVO<inf>4</Inf> Porous Anodes Used in Water Splitting Photoelectrochemical Cells. *J. Phys. Chem. C* **2015**, *119* (18), 9916–9925.

6.3 Synthesis of $LaFeO_3$ – Ni Photoelectrodes for Low Cost Plasmonic Enhancement for Solar Hydrogen Generation

The work done in this section is done with our collaborators. The aim was to replace plasmonic silver nanoparticles with low cost plasmonic nanoparticles. Our collaborators provided FDTD simulations to find out the best particle size range for best performance. My contribution to this work was to prepare and fabricate LFO-Ni, characterise and test them.

6.3.1 Introduction

With climate change and global warming ever becoming the focus of concern for millions of people globally, there is a critical need to develop scalable and sustainable energy source assets in a cost effective manner. The conversion of incoming photons from the sun light into storable chemical fuel (hydrogen), also known as solar fuel, is a highly attractive clean and sustainable energy storage solution. The semiconductor materials require favourable band alignments for water reduction/oxidation, optimal bandgaps and high stability under reaction conditions.[1] However, due to availability, cost, stability and synthesis procedures there are limitations to their use.

$LaFeO_3$ (LFO) has shown promise as a potential semiconductor material for water splitting due to its high stability and ability to generate hydrogen spontaneously without the need of an external bias.[2] However, due to its low absorption coefficient, the current density is low, thus yielding lower amounts of hydrogen. Metallic nanoparticles based on gold (Au) and silver (Ag), have the ability for enhancing optical extinction (scattering and absorption) by excitation of Surface Plasmon Resonance (SPR). LFO photoelectrodes light absorption has been improved by incorporation of plasmonic Ag nanoparticles via SPR effect, where current densities of more than two times improvement occurred when Ag nanoparticles were incorporated onto LFO films leading to over twice the amount of hydrogen generated compared to its untreated counterpart.[3] Other researches have shown when incorporating these metallic nanoparticles it leads to improved performances due to SPR effect. [4,5] Therefore, SPR is a potential method of improving a semiconductors light harvesting ability to improve its hydrogen production yield. However, both Au and Ag are costly and would drive up the cost of fabricating a photoelectrode, especially on an industrial scale.

Nickel (Ni), one of the earth’s most abundant elements, has been receiving a lot of attention due to its lower cost, electrochemical stability and availability. It has shown the ability to enhance hydrogen evolution when deposited on to graphene sheets,[6,7] crystalline silicon electrodes[8] and metal oxides.[1] Nickel nanoparticles have managed to improve the current density and hydrogen yield of these materials. Compared to strong SPR effect in Au and Ag nanoparticles, relatively weak SPR effect in Ni nanoparticles is less explored.[9,10] Amekura *et al.*[11] conducted an experiment where they embedded Ni nanoparticles into silica glass and identified the absorption peaks due to SPR effect from the Ni nanoparticles. This shows that Ni nanoparticles have the potential to improve a semiconductor’s light harvesting ability by SPR, thus improving the current density and hydrogen generation performance in a low cost manner. Therefore, Ni nanoparticle based LFO photocathode is prepared and performance evaluation is carried out to determine the enhancement in its photocurrent and hydrogen yield.

Herein, we report the design and fabrication of LFO-Ni photocathode and its performance. Finite Difference Time Domain (FDTD) simulations are employed to simulate the SPR resonances of Ni nanoparticles. The FDTD simulations show that the Ni nanoparticles with diameters in the range of 70 – 100 nm demonstrate good SPR effect suitable for incorporation with LFO photocathodes. Experimentally, these nanoparticles show enhanced light harvesting capabilities leading to higher photocurrent densities and greater hydrogen yield. To the best of our knowledge, this is the first time LFO-Ni photocathode has been synthesised leading to increased hydrogen production, due to SPR, when compared to its untreated counterpart.

6.3.2 Experimental

The full experimental details for LFO-Ni are given in chapter 5.

6.3.3 Results and Discussion

Optimised nanostructured LFO films were synthesised by spray pyrolysis (SP) as discussed in section 5.1. FDTD simulations were conducted by our collaborators to determine the best Ni particle size for best performance. Once they provided the data for best Ni particle size, we optimised the concentration of Ni nanoparticles to incorporate into the LFO photoelectrode by spin coating method to create LFO-Ni photoelectrodes. A comparative study between varying LFO-Ni nanoparticle concentration and plain LFO on PEC performance is studied. For this study Ni nanoparticle is used as a replacement for Ag nanoparticle as it is more readily available and in hopes to provide good performance enhancement, whilst bringing down the overall fabrication cost.

6.3.3.1 Finite Difference Time Domain Simulation

As mentioned the FDTD simulations were conducted by our collaborators where they used this technique to study the spectral response of Ni nanoparticles with varying particle size, to determine the optimal particle size for optimal performance.

Extinction, absorption and scattering cross-sections of Ni nanoparticle of varying diameter is shown in figures 62 (a) to 62 (i). The results show broad peaks in extinction and scattering, which red shift with the increase in size of the nanoparticle. For particle diameters greater than 110 nm, the scattering cross-section dominate over the absorption cross-section. The extinction cross-section is more than 3.5 times than the geometrical cross-section for Ni nanoparticle of diameter greater than 90 nm. It should be noted that the polarizability of Ni is weak compared to conventional noble metals such as Au and Ag, hence this results in weaker surface plasmon resonances[12,13]. Polarizability depends on the number of free electrons, nickel has less electrons compared to gold.[14] In general, the extinction cross-section increases with increase in particle diameter (figure 62 (g)). However, the normalized absorption cross-section (figure 62 (h)) decreases with increasing size of the nanoparticle while the normalized scattering cross-section increases (figure 62 (i)) with increasing size of the nanoparticle. However, larger particle sizes (>100 nm) tend to agglomerate which results in decreased SPR performance[15] and hence it is recommendable to use lower size nanoparticles. Particle size ranging between 70 – 100 nm provide optimal performance and is suggested to use sizes in this range.

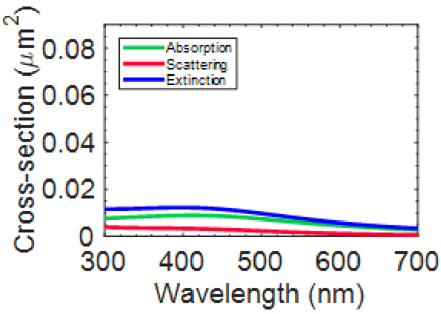
Cross-section (μm^2)
0.08
0.06
0.04
0.02
0
300
400
500
600
700
Wavelength (nm)
Absorption
Scattering
Extinction

(a)

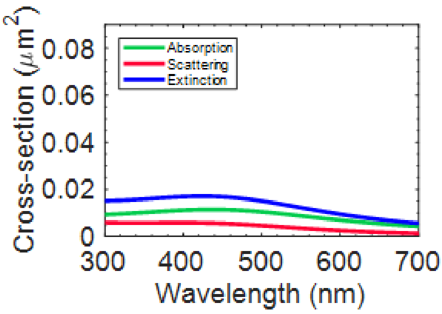
Cross-section (μm^2)
0.08
0.06
0.04
0.02
0
300
400
500
600
700
Wavelength (nm)
Absorption
Scattering
Extinction

(b)

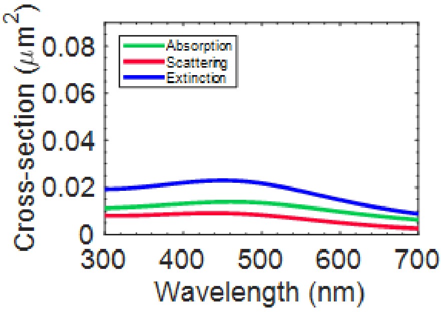
Cross-section (μm^2)
0.08
0.06
0.04
0.02
0
300
400
500
600
700
Wavelength (nm)
Absorption
Scattering
Extinction

(c)

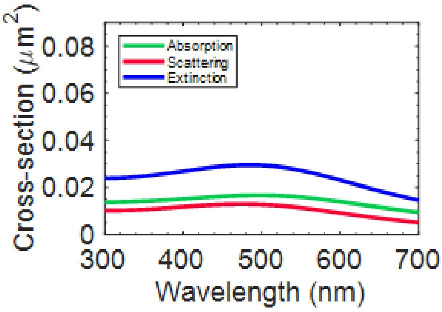
Cross-section (μm^2)
0.08
0.06
0.04
0.02
0
300
400
500
600
700
Wavelength (nm)
Absorption
Scattering
Extinction

(d)

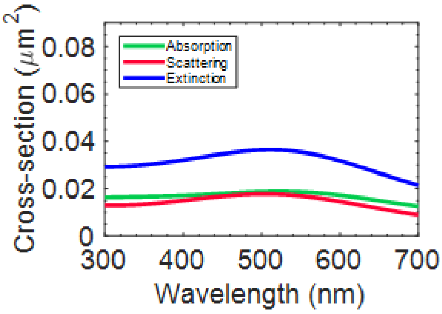
Cross-section (μm^2)
0.08
0.06
0.04
0.02
0
300
400
500
600
700
Wavelength (nm)
Absorption
Scattering
Extinction

(e)

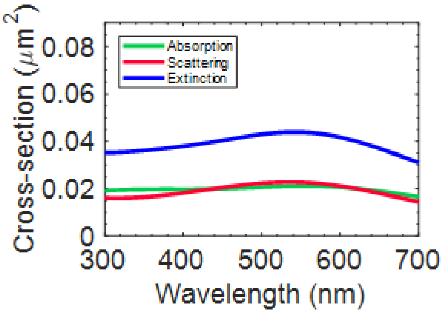
Cross-section (μm^2)
0.08
0.06
0.04
0.02
0
300
400
500
600
700
Wavelength (nm)
Absorption
Scattering
Extinction

(f)

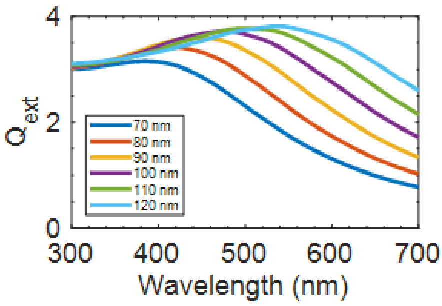
Q_{ext}
4
2
0
300
400
500
600
700
Wavelength (nm)
70 nm
80 nm
90 nm
100 nm
110 nm
120 nm

(g)

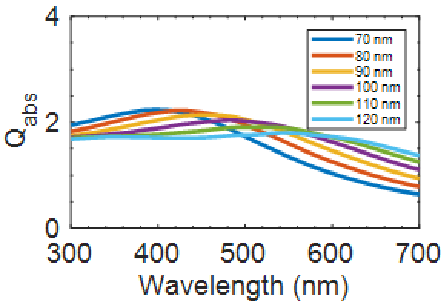
Q_{abs}
4
2
0
300
400
500
600
700
Wavelength (nm)
70 nm
80 nm
90 nm
100 nm
110 nm
120 nm

(h)

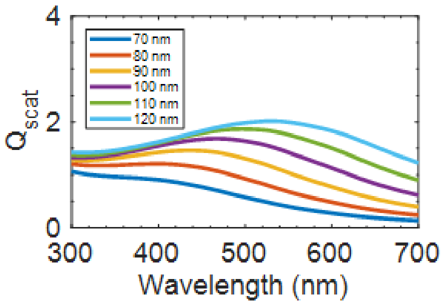
Q_{scat}
4
2
0
300
400
500
600
700
Wavelength (nm)
70 nm
80 nm
90 nm
100 nm
110 nm
120 nm

(i)

Figure 62: Extinction, Absorption and Scattering cross sections of Ni nanoparticles of diameters (a) 70 nm (b) 80 nm (c) 90 nm (d) 100 nm (e) 110 nm (f) 120 nm (g) normalized extinction cross-section (h) normalized absorption cross-section (i) normalized scattering cross-section.

6.3.3.2 PEC Performance and Characterisation of LFO-Ni Photoelectrode

The LFO films were prepared by using the optimised spraying parameters discussed in section 5.1, where the precursor solution is sprayed at 150^{o}C and then post-annealed at 550^{o}C to obtain single phase crystalline material. The optimized size range from theoretical modelling is 70-100 nm and the same range is used in fabrication of the LFO-Ni photoelectrode. The various concentrated solution of Ni nanoparticles (5.68 mmol, 2.84 mmol and 1.42 mmol) were first prepared as described in section 4.1.4.2 by suspending the particles in acetone. These Ni solutions were then spin coated on to separate pre-prepared LFO films described in section 4.1.4.3 to determine the optimum concentration of Ni nanoparticles required to give the best performance. The PEC performance of the LFO-Ni films were performed in 0.1 M aqueous NaOH (pH 13) solution by illuminating the photocathode from the electrolyte side to evaluate the current density, compared to plain LFO photocathode and their respective dark currents were also measured. The photocurrent density (*J*) is plotted against bias potential (*V*) as shown in figure 63. The untreated LFO film exhibited a maximum photocurrent of 0.036 mA/cm^2 at 0.6 V vs RHE. Upon incorporating 2.84 mmol Ni nanoparticles, there is a distinct improvement of the photocurrent density where it reaches a maximum of 0.066 mA/cm^2 at 0.6 V vs RHE due to the SPR effect. When increasing the concentration of Ni nanoparticles, a decrease in current density is observed in between the range of 0.7-1 V vs RHE by 10%. This decrease can be due to the higher content of Ni nanoparticles on the film surface reducing the electrode/electrolyte interface inhibiting effective charge separation, thus decreasing the amount of current density. As the Ni nanoparticle concentration is reduced to 1.42 mmol, there is also a decrease in photocurrent between the ranges of 0.7-1 V vs RHE by 7%. This can be due to lower amount Ni nanoparticle on the film available for SPR enhancement. Although the maximum current density for 1.42 mmol is higher than for the 2.84 mmol film, it is lower overall through the range. Therefore, from the entire three measured concentrations, 2.84 mmol Ni nanoparticle could result in the maximum overall yield.

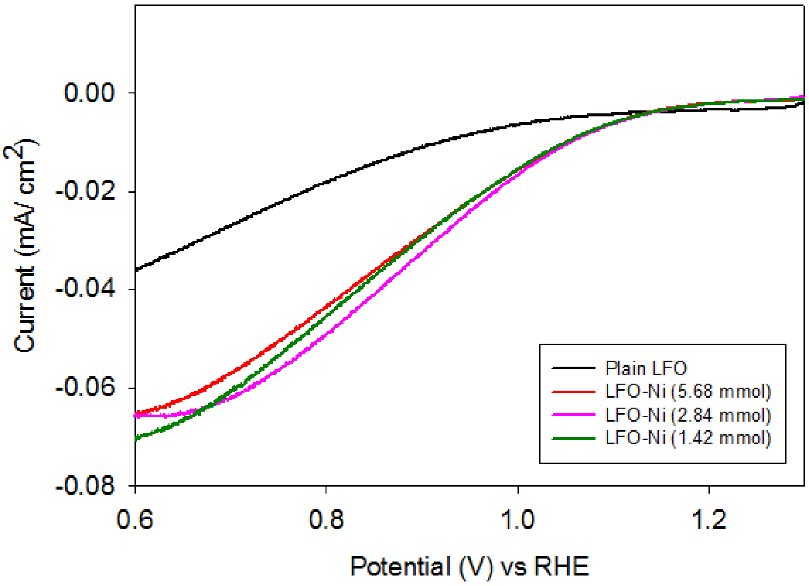

Figure 63: J-V characteristics of plain LFO and various LFO-Ni concentrations in a 0.1 M NaOH electrolyte vs RHE.

Chronoamperometric (CA) measurements of both LFO and best performing LFO-Ni (2.84 mmol) photocathodes were conducted in a 0.1 M NaOH aqueous electrolyte solution over a period of 20 hours with continuous illumination. A constant potential of 0 V was maintained during the course of the experiment. Figure 64 shows the stability performances of both photocathodes. As observed, both the photocathodes are very stable for the duration of the experiment, showing very little signs of current degradation. Most importantly, the current density of LFO-Ni (2.84 mmol) is over six times than that of plain LFO. This shows that with the incorporation of Ni nanoparticles on to the film, it greatly improves the current generated without losing stability. Therefore, we would expect an increase in hydrogen yield compared to that of plain LFO.

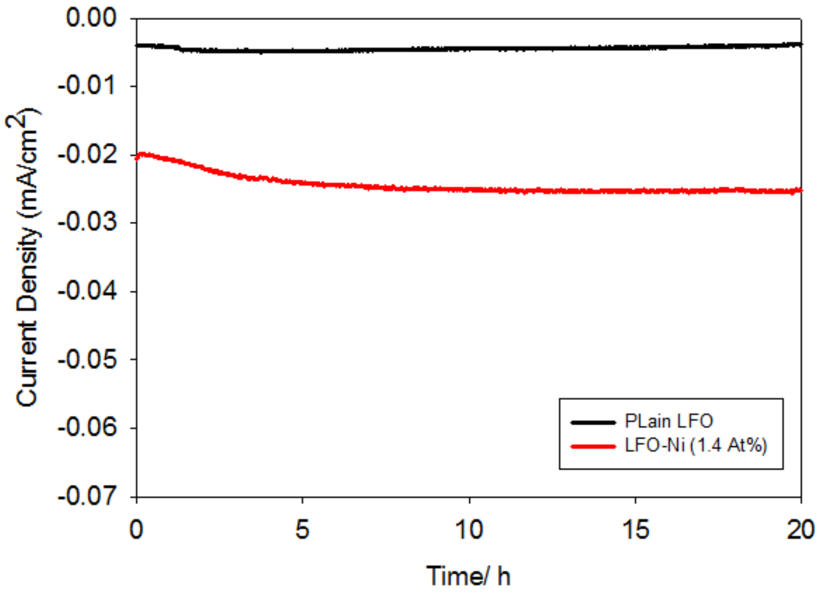

Figure 64: Chronoamperometric measurement of LFO and LFO-Ni (2.84 mmol) photocathodes in an aqueous 0.1 M NaOH electrolyte solution at 0 V vs Ag/AgCl.

LFO-Ni (2.84 mmol), the best performing photocathode, is taken to identify its crystal phase compared to its untreated counterpart. The XRD pattern for both photocathodes are shown in figure 65. The XRD patterns exhibits crystalline single phase peaks for plain LFO film with the LFO particles orientated in the (121) plane, which is in good agreement with previous works.[2] All the peaks correspond to correspond to LFO are indexed to orthorhombic system (JCPDS 00-037-1439). No Ni diffraction peaks were detected in the LFO-Ni film, which can be due to small particle size, dispersity or low Ni nanoparticle loading content. We would expect there to be three characteristic Ni peaks at 44.5, 51.8 and 76.4 considering bulk material.[16,17] Peaks marked with an asterisk correspond to the FTO peaks, distinguishing it from the LFO peaks.

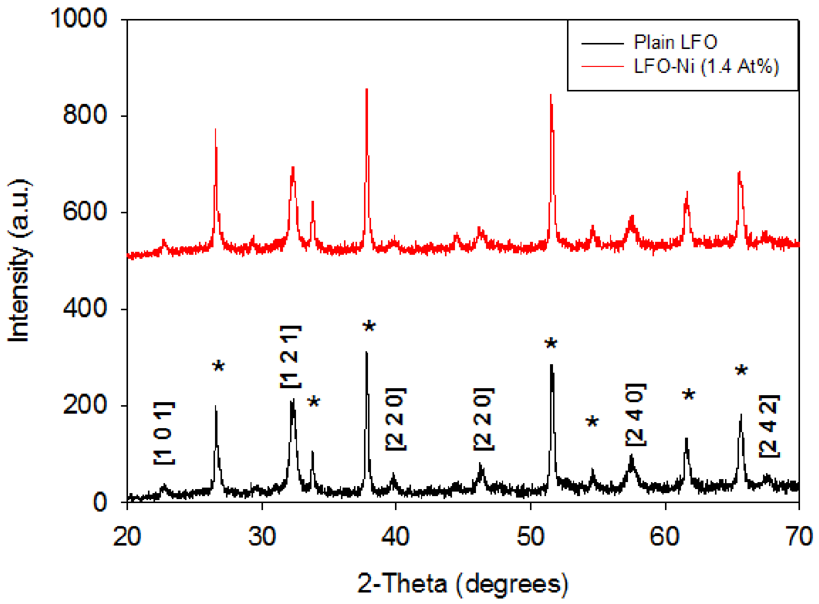

Figure 65: XRD pattern of plain LFO and LFO-Ni (2.84 mmol) on FTO glass substrate. The peaks marked with asterisk represent FTO.

A top view SEM for plain LFO and LFO-Ni (2.84 mmol) was taken to look at its morphology and to compare the two. The plain LFO nanostructured film (figure 66 (a)) shows well connected crystal grain structure, post annealing at 550^{o}C. Its EDX (figure 66 (c)) confirms that there is no Ni nanoparticle present on the film. Figure 66 (b) shows bright spherical nanoparticles distributed across the film which can be attributed to the Ni nanoparticles confirmed by its EDX (figure 66 (d)). Comparing images 66 (a) and (b), it can been seen that Ni nanoparticle have been incorporated into the LFO film after spin coating, which is further confirmed by their respective EDX analysis.

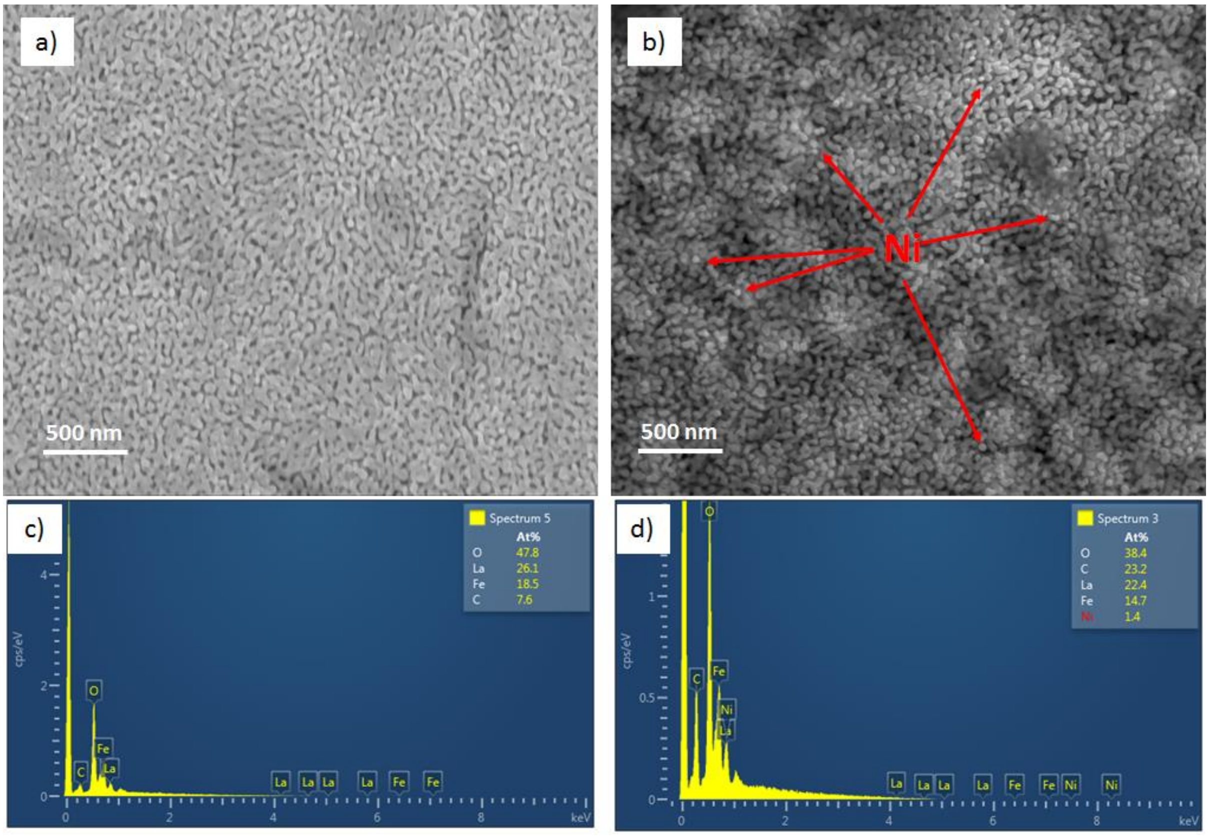

Figure 66: (a) Top view SEM of plain LFO film, **(b)** top view SEM of LFO-Ni (2.84 mmol), **(c)** EDX for plain LFO, **(d)** EDX for LFO-Ni (2.84 mmol).

To understand the effect of Ni nanoparticles on light absorption, its optical properties were measured using UV-Vis spectroscopy. Figure 67 shows the absorption spectra of both plain LFO and LFO-Ni (2.84 mmol) at wavelengths from 360 – 800 nm, and the inset of fig. 6 shows all LFO-Ni UV-Vis absorption. There was a higher absorption of light in the short wavelength

(400 – 600 nm) and a slight increase in the long wavelength region (600 – 800 nm), which can be attributed to increased light extinction from the Ni nanoparticle in this frequency range due to SPR effect. We can observe that the highest Ni concentration provides lowest increased absorption of light, and decreasing the Ni concentration more light is absorbed. This can be because there will be more number of Ni nanoparticles within a specific area when concentration is highest compared to lower concentration. Therefore, it will reflect some scattered light away from LFO film as higher Ag concentration is blocking the film due to agglomeration of Ni particles on LFO film surface. When concentration of Ni nanoparticles decreases, the scattered light is directed more towards the LFO film as more of the film is exposed. It should also be noted that as Ni loading content falls to 1.42 mmol, the absorbance decreases compared to 2.84 mmol. This will be because there is less Ni available for SPR effect. The optimum concentration for optimum absorbance is 2.84 mmol of Ni nanoparticles. The SPR effect results in higher effective absorption of light in the semiconductor due to light concentration which increases the electron-hole generation in the semiconductor,[18] PIRET (Plasmon induced Resonance Energy Transfer) through dipole-dipole interaction and light scattering which results in increased effective optical path length. In addition, nanoparticles at the semiconductor-electrolyte can also increase the catalytic effects. The relative contribution of each of these effects in our Ni incorporated LFO films requires further detailed study.

By incorporating Ni nanoparticles on to the LFO film, we observe an enhancement of light harvesting capability compared to plain LFO. This is seconded by the increase in current density in case of PEC performance (figure 63). Therefore, a higher volume of hydrogen is expected to be obtained from the solar water splitting experiment. As the photocathode absorbs more light, it generates more current for water splitting, thus yielding a greater volume of hydrogen.

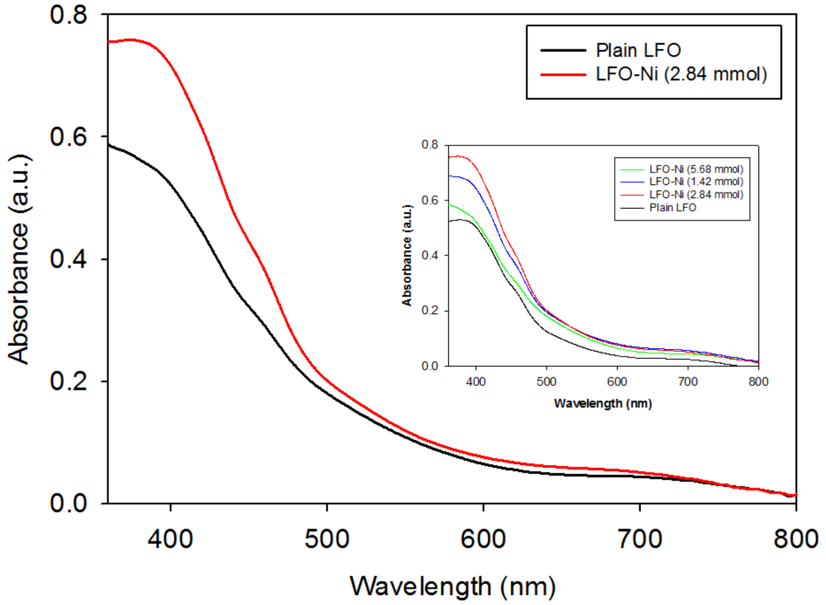

Figure 67: Absorbance spectra of plain LFO and LFO-Ni (2.84 mmol). Inset shows absorbance spectra for all LFO-Ni.

6.3.3.3 Hydrogen evolution Measurement

Hydrogen evolution measurements were conducted in an aqueous 0.1 M NaOH solution under constant illumination, for the plain LFO film and for various LFO-Ni films (figure 68). The water splitting test was conducted in a custom made glass reactor vessel with an attached fused silica viewport. The working electrode and Pt mesh counter electrode were connected by a single looped wire, without any external bias being applied. After three hours, the plain LFO photocathode begins spontaneously producing hydrogen via solar water splitting. After six hours of reaction time, it has generated 0.11 μmol/cm^2 of hydrogen. On the other hand, all of the LFO-Ni photocathodes begun spontaneously generating hydrogen after two hours of reaction time. This is a marked improvement compared to the untreated LFO. This improvement can be ascribed due to the SPR effect of Ni nanoparticles resulting in enhanced light harvesting capability of the photoelectrode, where it produces more electrons available for conversion to hydrogen. This is in good agreement with the *J-V* curves seen in figure 63. As 2.84 mmol of Ni nanoparticle is incorporated into the film, there is an increase in current, which subsequently leads to an increase in hydrogen yield; after six hours 0.29 μmol/cm^2 is produced. This is an improvement of more than two times. As the Ni concentration is reduced to 1.42 mmol, there is a decrease in current leading to a drop in hydrogen yield where at 6 hours it generates 0.22 μmol/cm^2. Due to lower Ni content there is less light being trapped due to plasmonic effect so less electrons are generated thus leading to the drop in hydrogen yield compare to LFO-Ni (2.84 mmol) respectively. When the concentration of Ni is increased to 5.68 mmol as expected there is a decrease in hydrogen yield, after 6 hours it has only generated 0.14 μmol/cm^2. This will be due to the higher content of Ni nanoparticles on the film surface reducing the electrode/electrolyte interface inhibiting effective charge separation, or the Ni nanoparticles agglomerating lowering its effective surface area. Therefore, the optimal concentration of Ni nanoparticle for improved current and hydrogen yield is 2.84 mmol.

By comparing the hydrogen evolution performance of LFO-Ni compared to LFO-Ag in section 6.2.3.3 figure 61, we can see that the best performing LFO-Ni (2.84 mmol) yields 0.29 μmol/cm^2 hydrogen, slightly less than the best performing LFO-Ag (0.19 mmol) yielding 0.32 μmol/ cm^2. Also LFO-Ni starts spontaneously producing hydrogen after two hours whereas LFO-Ag starts to spontaneously produce hydrogen after one hour. Although the performance of LFO-Ni is less than that of LFO-Ag this is only marginal as the best performing LFO-Ni almost produces the same amount of hydrogen as the best performing LFO-Ag after six hours, and the delay in production is only one hour. Therefore, the lower costing Ni nanoparticles is a viable option to replacing Ag nanoparticles to bring down the overall cost without affecting hydrogen production performance by much.

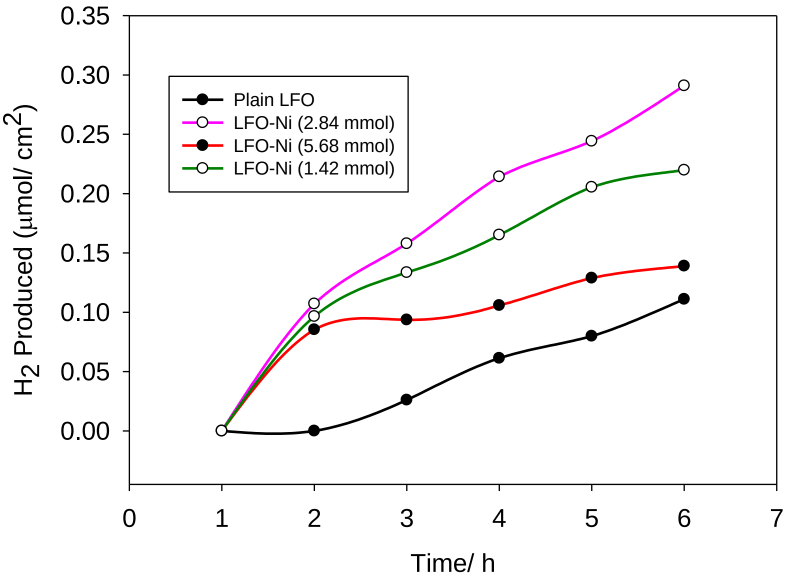

Figure 68: Hydrogen evolution test of plain LFO and LFO-Ni with varying Ni concentrations, in an aqueous 0.1 M NaOH solution.

6.3.4 Conclusion

In summary, we have incorporated optimized Ni nanoparticles (of diameters ranging from 70 – 100 nm) on to the nanostructured LFO photocathode. The photocathode shows an increase of light absorption upon incorporating Ni nanoparticles compared to its untreated counterpart. This agrees well with FDTD studies, which shows good light harvesting ability of Ni nanoparticles of small sizes ranging from 70 – 100 nm, where there will be lower chances of aggregation. Incorporation of Ni nanoparticle has increased the current density, where the best performing LFO-Ni (2.84 mmol) photocathode generated more than twice the current density compared to plain LFO, due to the SPR effect from Ni nanoparticles. This subsequently led to the LFO-Ni (2.84 mmol) photocathode producing more than double (2.64 times) the amount of hydrogen compared to the plain LFO. The optimized photocathode generated 0.29 μmol/cm^2 hydrogen after six hours of operation whereas the plain LFO only generated 0.11 μmol/cm^2. Furthermore, the LFO-Ni photocathodes were able to produce hydrogen after two hours of illumination compared to the untreated LFO photocathode, which began forming hydrogen only after three hours of illumination. Additionally, LFO-Ni compared to LFO-Ag yields 0.29 μmol/cm^2 hydrogen, slightly less than the best performing LFO-Ag (0.19 mmol) yielding 0.32 μmol/ cm^2. Although the performance of LFO-Ni is less than that of LFO-Ag this is only marginal as the best performing LFO-Ni almost produces the same amount of hydrogen as the best performing LFO-Ag after six hours, and the delay in production is only one hour. Therefore, the lower costing Ni nanoparticles is a viable option to replacing Ag nanoparticles to bring down the overall cost without affecting hydrogen production performance by much.

Reference

(1) Dubale, A. A.; Pan, C.-J.; Tamirat, A. G.; Chen, H.-M.; Su, W.-N.; Chen, C.-H.; Rick, J.; Ayele, D. W.; Aragaw, B. A.; Lee, J.-F.; Yang, Y.-W.; Hwang, B.-J. Heterostructured Cu_2O/CuO Decorated with Nickel as a Highly Efficient Photocathode for Photoelectrochemical Water Reduction. *J. Mater. Chem. A* **2015**, *3* (23), 12482–12499.

(2) Pawar, G. S.; Tahir, A. A. Unbiased Spontaneous Solar Fuel Production Using Stable LaFeO3 Photoelectrode. *Sci. Rep.* **2018**, *8* (1), 3501.

(3) Pawar, G. S.; Elikkottil, A.; Seetha, S.; Reddy, S.; Pesala, B.; Tahir, A. A.; Mallick, T. K. Enhanced Photoactivity and Hydrogen Generation of LaFeO 3 Photocathode by Plasmonic Silver Nanoparticle Incorporation. *ACS Appl. Energy Mater.* **2018**, *1* (7), 3449–3456.

(4) Zhang, Z.; Zhang, L.; Hedhili, M. N.; Zhang, H.; Wang, P. Plasmonic Gold Nanocrystals Coupled with Photonic Crystal Seamlessly on TiO_2 Nanotube Photoelectrodes for Efficient Visible Light Photoelectrochemical Water Splitting. *Nano Lett.* **2013**, *13* (1), 14–20.

(5) Lian, Z.; Wang, W.; Xiao, S.; Li, X.; Cui, Y.; Zhang, D.; Li, G.; Li, H. Plasmonic Silver Quantum Dots Coupled with Hierarchical TiO<inf>2</Inf> Nanotube Arrays Photoelectrodes for Efficient Visible-Light Photoelectrocatalytic Hydrogen Evolution. *Sci. Rep.* **2015**, *5* (April), 1–10.

(6) Indra, A.; Menezes, P. W.; Kailasam, K.; Hollmann, D.; Schröder, M.; Thomas, A.; Brückner, A.; Driess, M. Nickel as a Co-Catalyst for Photocatalytic Hydrogen Evolution on Graphitic-Carbon Nitride (Sg-CN): What Is the Nature of the Active Species? *Chem. Commun.* **2016**, *52*

(1), 104–107.

(7) Zhang, W.; Li, Y.; Zeng, X.; Peng, S. Synergetic Effect of Metal Nickel and Graphene as a Cocatalyst for Enhanced Photocatalytic Hydrogen Evolution via Dye Sensitization. *Sci. Rep.* **2015**, *5* (May), 1–12.

(8) McKone, J. R.; Warren, E. L.; Bierman, M. J.; Boettcher, S. W.; Brunschwig, B. S.; Lewis, N. S.; Gray, H. B. Evaluation of Pt, Ni, and Ni–Mo Electrocatalysts for Hydrogen Evolution on Crystalline Si Electrodes. *Energy Environ. Sci.* **2011**, *4* (9), 3573.

(9) Picciotto, A.; Pucker, G.; Torrisi, L.; Bellutti, P.; Caridi, F.; Bagolini, A. Evidence of Plasmon Resonances of Nickel Particles Deposited by Pulsed Laser Ablation. *Radiat. Eff. Defects Solids* **2008**, *163* (4–6), 513–518.

(10) Dalouji, V.; Elahi, S. M.; Naderi, S. Surface Plasmon Resonance and Electrical Properties of RF: Magnetron Sputtered Carbon–nickel Composite Films at Different Annealing Temperatures. *Rare Met.* **2016**, *35* (11), 863–869.

(11) Amekura, H.; Takeda, Y.; Kitazawa, H.; Kishimoto, N. Resonance Energy of Surface Plasmon of Nickel Nanoparticles in Silica Glasses. *Phot. Process. Microelectron. Photonics Ii* **2003**, *4977* (October 2015), 639–647.

(12) Attaran, A.; Emami, S. D.; Soltanian, M. R. K.; Penny, R.; behbahani, F.; Harun, S. W.; Ahmad, H.; Abdul-Rashid, H. A.; Moghavvemi, M. Circuit Model of Fano Resonance on Tetramers, Pentamers, and Broken Symmetry Pentamers. *Plasmonics* **2014**, *9* (6), 1303–1313.

(13) Cuadrado, A.; López-Alonso, J. M.; González, F. J.; Alda, J. Spectral

Response of Metallic Optical Antennas Driven by Temperature. *Plasmonics* **2017**, *12* (3), 553–561.

(14) Chen, J.; Albella, P.; Pirzadeh, Z.; Alonso-González, P.; Huth, F.; Bonetti, S.; Bonanni, V.; Åkerman, J.; Nogués, J.; Vavassori, P.; Dmitriev, A.; Aizpurua, J.; Hillenbrand, R. Plasmonic Nickel Nanoantennas. *Small* **2011**, *7* (16), 2341–2347.

(15) Du, M.; Tang, G. H. Optical Property of Nanofluids with Particle Agglomeration. *Sol. Energy* **2015**, *122*, 864–872.

(16) Sapkal, S. B.; Shelke, K. F.; Shingate, B. B.; Shingare, M. S. Nickel Nanoparticle-Catalyzed Facile and Efficient One-Pot Synthesis of Polyhydroquinoline Derivatives via Hantzsch Condensation under Solvent-Free Conditions. *Tetrahedron Lett.* **2009**, *50* (15), 1754–1756.

(17) Cheng, J.; Zhang, X.; Ye, Y. Synthesis of Nickel Nanoparticles and Carbon Encapsulated Nickel Nanoparticles Supported on Carbon Nanotubes. *J. Solid State Chem.* **2006**, *179* (1), 91–95.

(18) Valenti, M.; Jonsson, M. P.; Biskos, G.; Schmidt-Ott, A.; Smith, W. A. Plasmonic Nanoparticle-Semiconductor Composites for Efficient Solar Water Splitting. *J. Mater. Chem. A* **2016**, *4* (46), 17891–17912.

6.4 Synthesis of $TaFeO_4$ by Sol-Gel Method for Solar Hydrogen Evolution

6.4.1 Introduction

Hydrogen has long been identified as one of the most promising energy carriers. The largest challenge is to produce hydrogen at a large scale by economically and environmentally sustainable process via renewable source with zero carbon emission. Tremendous efforts have been made over the past decade to find and synthesise semiconductor materials for solar hydrogen evolution.[1–8] Suitable material for artificial photosynthesis should be able to absorb maximum photon from sunlight, accessing visible light region for efficient solar to chemical conversion, and act as an effective catalyst. Therefore, the semiconductor electrode must have low electron affinity, good charge separation, good stability against photocorrosion and a band gap of 1.8-2.4 eV for maximum solar to chemical conversion.

There are a number of tantalum based semiconductor materials showing good activity for solar water splitting such as tantalum oxide,[9] alkaline tantalate,[10] tantalum nitride[11] and tantalum oxynitride.[12] These materials are able to do the water splitting reaction, hence tantalum based semiconductors show good photoactivity. $TaFeO_4$ (TFO) is an unexplored tantalum based semiconductor material. There has been only two mentions of fabricating this material,[13,14] where they were synthesised at high temperatures of 700 – 1100°C to achieve single phase TFO. This shows that it is possible to synthesis this material, however there has not been any reports on to any possible applications for TFO and is completely unexplored.

Herein, we fabricate nanostructured $TaFeO_4$ by sol-gel method and find the optimal annealing temperature for fabricating the material. The performance of the nanostructured TFO was examined and tested to see if any hydrogen is evolved from the water splitting reaction.

6.4.2 Experimental

The full experimental details for TFO fabrication is given in chapter 5.1.5.

6.4.3 Results and Discussion

6.4.3.1 Optimisation and Characterisation

After tantalum (V) chloride and iron (III) chloride had been converted to iron and tantalum hydroxide precipitates with ammonium hydroxide, it was dissolved in 2 M citric acid where the metals are in a 1:1 ratio. Once fully dissolved, it was then annealed at 800^{o}C for 3 hours in air to see if single phase crystalline TFO was synthesised as suggested by Pourroy *et.al.*[13] Figure 69 shows the XRD pattern for TFO synthesised at 800^{o}C. We can observe that there are mixed phases of $TaFeO_4$ (marked with green dots and are indexed to a tetragonal system, JCPDS 01-071-0932), tantalum oxide (marked with blue dots and are indexed to an orthorhombic system, JCPDS 01-089-2843) and iron oxide (marked with red dots and are indexed to a cubic system, JCDPS 00-026-1136). Hence, 800^{o}C is not enough energy required to bind all the iron and tantalum metal centres together without forming mixed oxide phases. Therefore, the temperature was taken up to 1100^{o}C to attempt to form single phase crystalline TFO as shown by Pourroy *et.al.*[13] Figure 70 shows the XRD pattern of TFO synthesised at 1100^{o}C for 3 hours in air. Here all the peaks are correlate to single phase TFO and are indexed to tetragonal system (JCPDS 01-071-0932) with the TFO particles orientated in the (1 1 0) plane. Comparing figure 69 and figure 70 we can see that once annealed at 1100ºC we get single phase TFO. This shows that very high temperatures are required for synthesising TFO, which is not very energy efficient. Although one thing to note is that the TFO annealed at 1100ºC produces very crystalline TFO particles compared to the one annealed at 800ºC which is more amorphous in comparison.

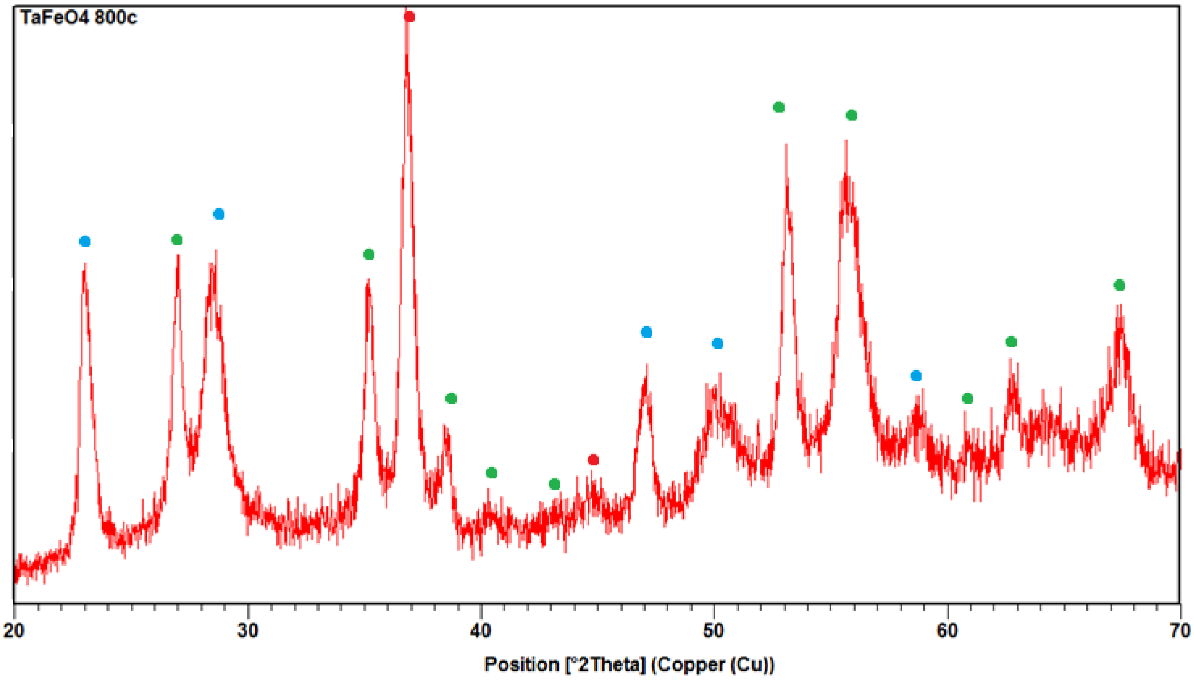

Figure 69: XRD pattern of TFO annealed at 800ºC where green dots represent TFO, blue dots represent tantalum oxide and red dots represent iron oxide.

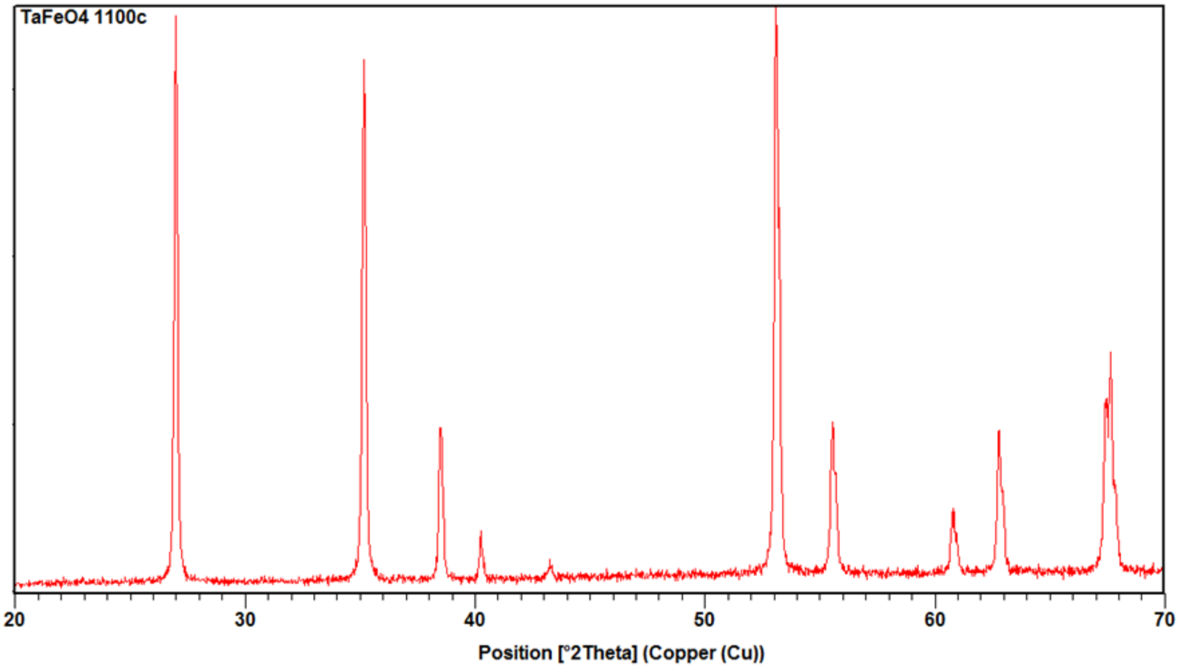

Figure 70: XRD pattern of TFO annealed at 1100ºC.

An SEM image of the TFO synthesised at 1100ºC is taken in order to determine its morphological structure (figure 71). The SEM image reveals well connected crystal grain structure with the largest grain size at around 500 nm. It can also be observed that the material looks porous indicating a good surface area for increased material/ electrolyte interface, which could potentially lead to good hydrogen yield. EDX in figure 72 shows that only iron and tantalum are present in a 1:1 ratio (Fe 22.44 At % and Ta 22.33 At %) with no other contaminates. Figure 73 shows the elemental mapping of TFO, it shows that the iron and tantalum are homogeneously mixed in the nanopowder emphasising its uniformity.

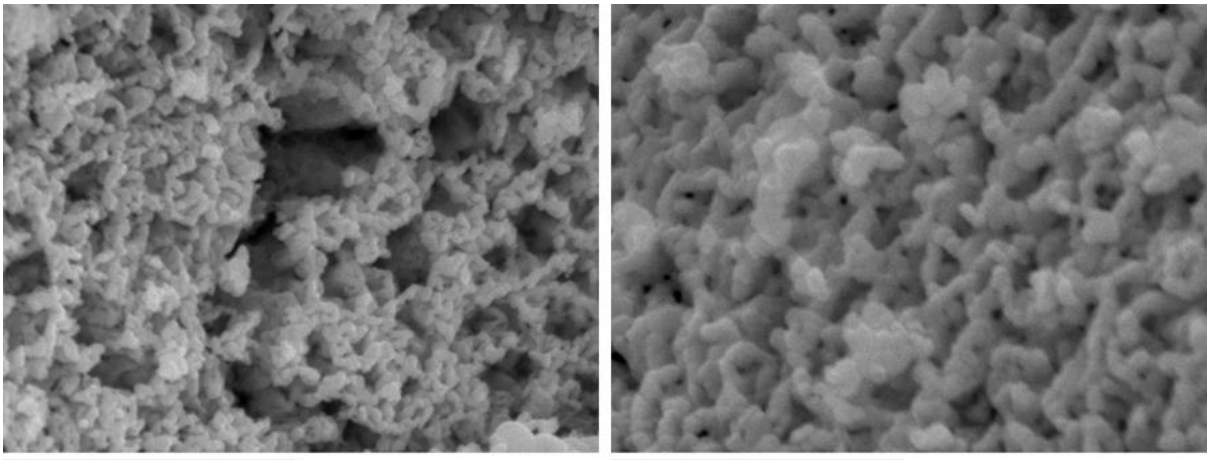

Figure 71: SEM images of TFO.

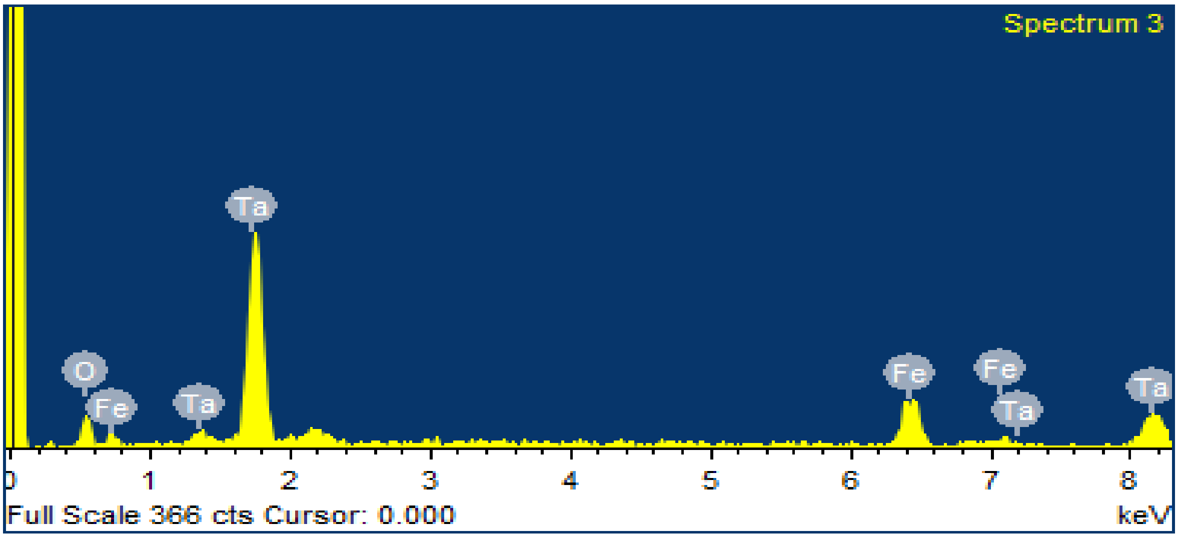

Figure 72: EDX of $TaFeO_4$ showing peaks of tantalum, iron and oxygen.

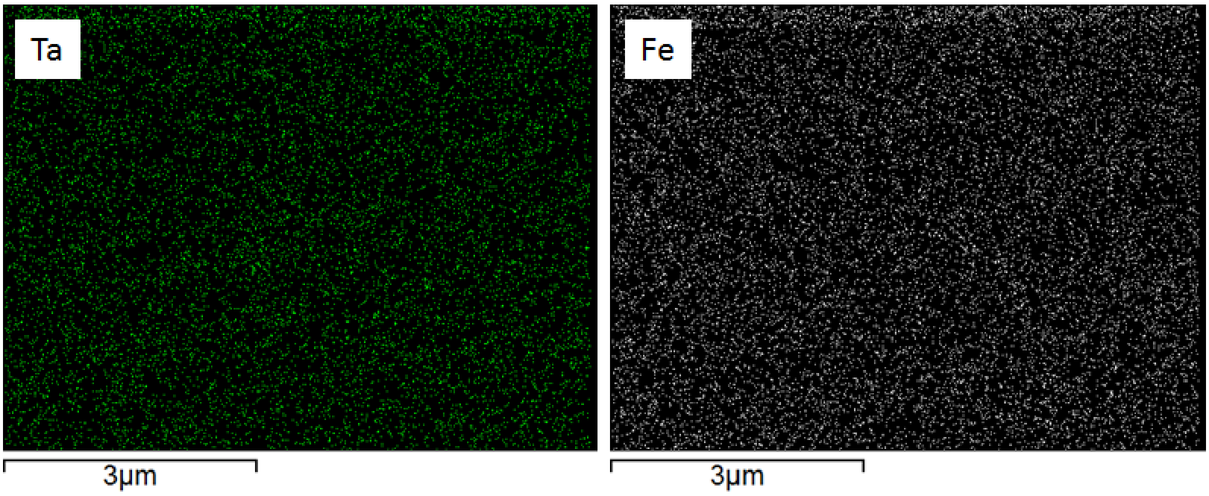

Figure 73: Elemental mapping showing the distribution of tantalum and iron in the nanopowder.

6.4.3.2 Optical Measurement

Optical measurements (reflectance) for the TFO powder were taken to help determine its band gap. This was measured using the UV-Vis spectroscopy. Figure 74 shows the reflectance measurement of TFO at wavelengths between ranges of 350 – 800 nm. On this graph we see a peak at 450 nm, indicating that TFO has access to the visible region of the light spectrum. Using this data we can calculate the band gap of this material by using the Kubelka – Munk equation (equation 17).[15] Where by plotting this equation as a function of the energy in eV, the band gap of the semiconductor particle can be found be extrapolating it to the x-axis.

$[F(R) \times hv]^n$ **(eq. 17)**

Where F(R) is proportional to the excitation coefficient, *hv* is the energy in eV and *n* is ½ for an indirect allowed transition or 2 for direct allowed transition. Figure 75 shows the Kubelka – Munk plot for determining TFO band gap.

Here we have a direct band gap of 2.65 eV, shown where the red line intersects the x-axis. By using equation 18 the wavelength (λ) of the material can be calculated from the band gap.[16]

λ = 1240/ Energy of band gap **(eq. 18)**

From this the wavelength is calculated to be 468 nm which is in good agreement with the reflectance data of 450 nm. This band gap is relatively large compared to some of the best performing semiconductor materials e.g. copper oxide (2 eV).[17] Due to band gap size of TFO, it has access to the lower end of the visible light spectrum hence we will expect it to have lower hydrogen generating efficiency compared to materials such as copper oxide.

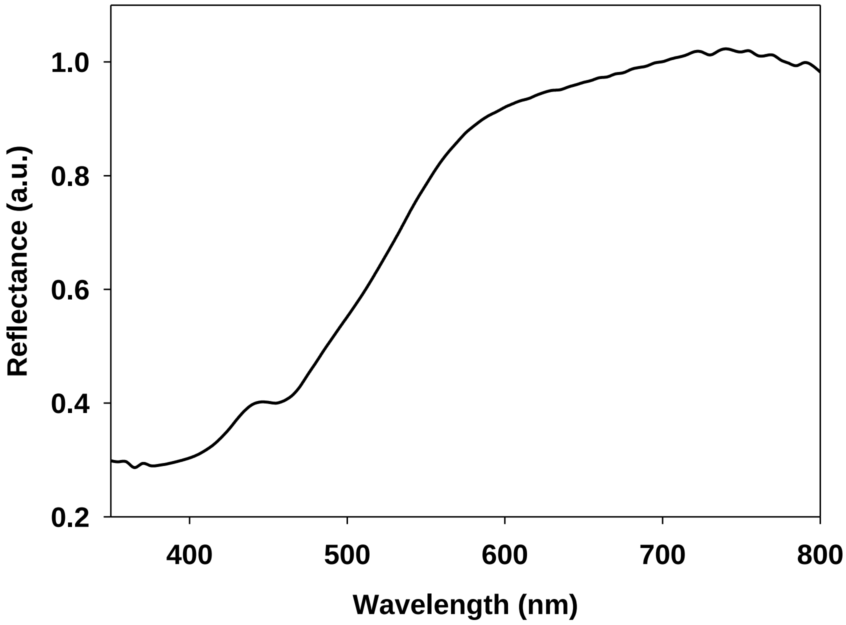

Figure 74: Reflectance spectra of TFO.

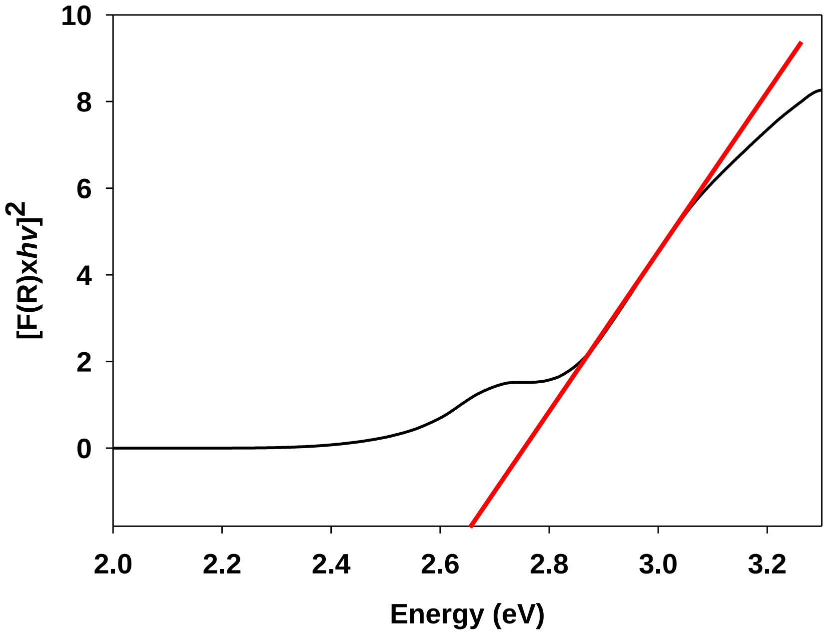

Figure 75: Kubelka-Munk plot showing TFO bang gap energy.

6.4.3.3 Hydrogen Evolution Measurement

Hydrogen evolution measurements were conducted in an aqueous 0.1 M NaOH solution under constant illumination. The water splitting test was conducted in a sealed glass vial containing the 0.1 g TFO photocatalyst under constant stirring. For the first six hours there was no hydrogen evolution activity (figure 76). From seven hours hydrogen was being detected up to nine hours. After nine hours 0.091 µmol/ g of hydrogen was generated. This results show that TFO is able to generate hydrogen, although its efficiency is poor as it takes seven hours to generate and accumulate enough hydrogen for detection. This poor efficiency can be attributed to the larger band gap size giving it access to only the lower region of visible light spectrum, which is in good agreement with the optical measurements.

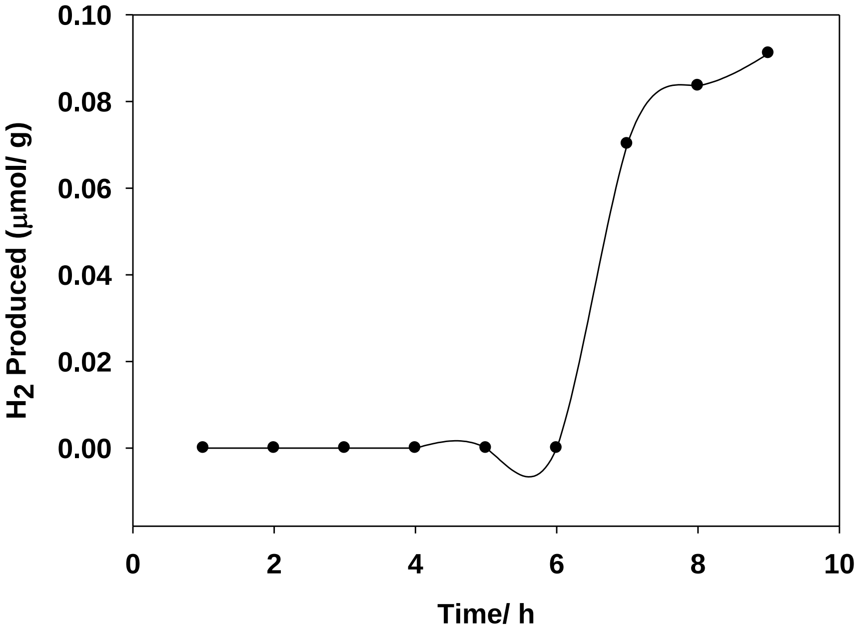

Figure 76: Hydrogen evolution test of TFO in aqueous 0.1 M NaOH electrolyte solution.

6.4.3.4 $TaFeO_4$ Photoelectrode Fabrication

Attempts were made to try and fabricate a photoelectrode form of TFO so it can help us to determine the materials photocurrent density, which would tell us if it is an n-type or p-type material, and to help us determine its flat band by EIS measurements so we can determine the position of the materials band edges to help construct its band diagram.

Initially, the prepared TFO gel was pasted on to FTO glass substrate and annealed at 1100^oC for 3 hours to try and fabricate the TFO photoelectrode. However, at temperatures beyond 700^oC the glass substrate begins to melt and the substrate is destroyed.

Once it was decided that regular FTO glass substrate is unsuitable for TFO photoelectrode fabrication, quartz FTO glass substrate was used as its substitute. Quartz glass has a softening point of 1600°C which is more than suitable for our purpose. The pre-prepared TFO gel was pasted onto the quartz FTO and annealed at 1100°C for 3 hours. Once cooled the quartz glass was still intact and a LSV was taken to determine its current density, however there was no response. It was discovered that at the high temperatures of 1100°C the conductive FTO layer evaporated off. Therefore, although the substrate did not get destroyed there was no conductive contact for the electrons to transfer to hence no measurements can be taken.

An alternative to FTO glass substrate is conductive carbon fibre material. Carbon fibre is a conductive material and under inert atmosphere (e.g. under Ar or N_2 gas) it will not evaporate to graphene oxide. This makes it an attractive substitute to the FTO glass substrate. The pre-prepared TFO gel is pasted on to a 3 x 2 cm carbon fibre fabric material. This is then annealed at 1100°C under Ar atmosphere for 1 hour as to not run out of gas. An XRD of carbon fibre TFO (c-TFO) is taken to make sure single phase TFO is still made under the Ar atmosphere and to make sure it has not reacted with the carbon fibre material (figure 77). Also, an XRD of carbon fibre is taken for comparison. The XRD pattern shows crystalline single phase peaks of $FeTa_2O_6$ where the peaks correspond to a tetragonal system (JCPDS 01-088-1718). Under these reaction conditions we obtain a different TFO phase. This maybe because of the inert atmosphere the annealing occurs under, because when the same TFO gel is annealed under air we obtain $TaFeO_4$. The broad hump between 20 – 30 2θ angles is due to the carbon fibre as we can see when comparing the c-TFO and carbon fibre XRDs. LSV of the c-TFO is taken, however we observe no current density response. This may be due to the different phase we obtained or may be due to the fact that after annealing the carbon fibre material becomes very brittle so its connection is not very good as it breaks apart.

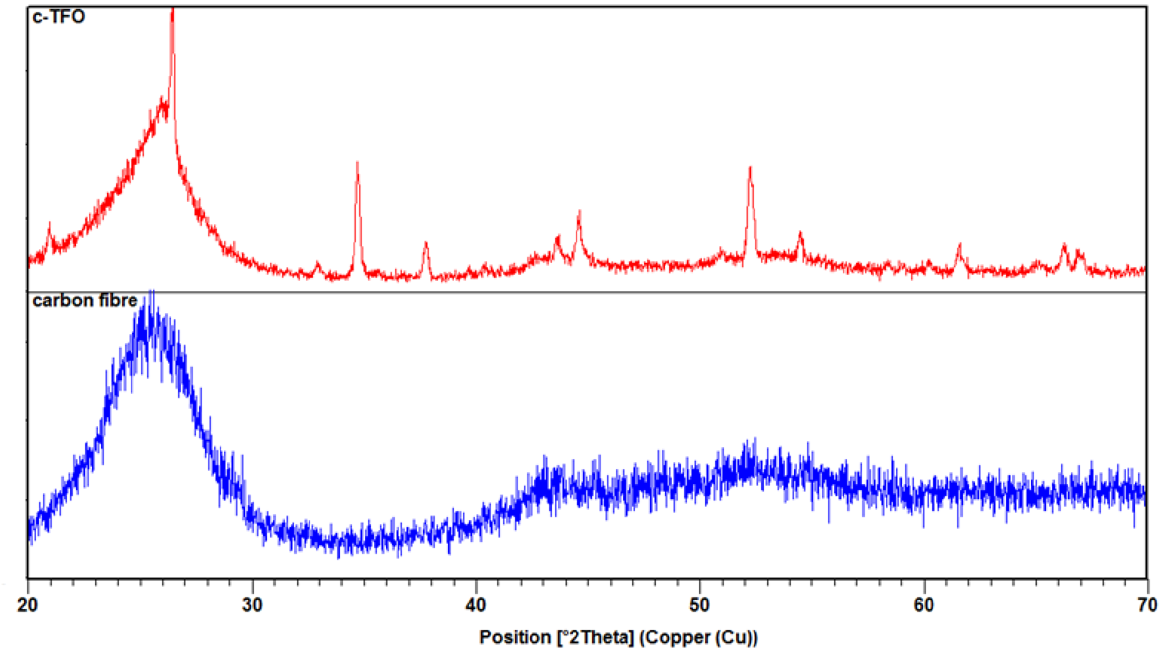

Figure 77: XRD pattern for c-TFO and carbon fibre.

6.4.4 Conclusion

In summary, we have optimised the synthesis of $TaFeO_4$ nanopowder photocatalyst. The band gap of TFO was determined to be 2.65 eV which was calculated using the Kubelka-Munk plot vs energy. The relatively large band gap of TFO meant that it has access to the lower end of the visible light spectrum which lead to low efficiency of hydrogen generation. TFO started producing hydrogen gas after seven hours and at nine hours generated 0.091 μmol/ g of hydrogen. Attempts were made to synthesise photoelectrode form of TFO, however this proved difficult as FTO glass substrate were not suitable at high temperatures as wither the glass melted or the conductive FTO layer evaporated off. Carbon fibre substitute was used to synthesise c-TFO, but a different phase of TFO ($FeTa_2O_6$) was formed under inert atmosphere. Furthermore, it was not active under LSV experiment as the material was too brittle after annealing. More work is required to improve TFOs efficiency and to try and find a suitable way of synthesising an electrode form of TFO.

Reference

(1) Ida, S.; Yamada, K.; Matsunaga, T.; Hagiwara, H.; Matsumoto, Y.; Ishihara, T. Preparation of P-Type CaFe2O4 Photocathodes for Producing Hydrogen from Water. *J. Am. Chem. Soc.* **2010**, *132* (49), 17343–17345.

(2) Jia, Q.; Iwashina, K.; Kudo, A. Facile Fabrication of an Efficient BiVO 4 Thin Film Electrode for Water Splitting under Visible Light Irradiation. *Pnas* **2012**, *109*, 11564–11569.

(3) Pihosh, Y.; Turkevych, I.; Mawatari, K.; Uemura, J.; Kazoe, Y.; Kosar, S.; Makita, K.; Sugaya, T.; Matsui, T.; Fujita, D.; Tosa, M.; Kondo, M.; Kitamori, T. Photocatalytic Generation of Hydrogen by Core-Shell WO3/BiVO4 Nanorods with Ultimate Water Splitting Efficiency. *Sci. Rep.* **2015**, *5* (February), 1–10.

(4) Paracchino, A.; Laporte, V.; Sivula, K.; Grätzel, M.; Thimsen, E. Highly Active Oxide Photocathode for Photoelectrochemical Water Reduction. *Nat. Mater.* **2011**, *10* (6), 456–461.

(5) Yang, Y.; Xu, D.; Wu, Q.; Diao, P. Cu2O/CuO Bilayered Composite as a High-Efficiency Photocathode for Photoelectrochemical Hydrogen Evolution Reaction. *Sci. Rep.* **2016**, *6* (1), 35158.

(6) Hussain, S.; Hussain, S.; Waleed, A.; Tavakoli, M. M.; Wang, Z.; Yang, S.; Fan, Z.; Nadeem, M. A. Fabrication of CuFe2O4/α-Fe2O3Composite Thin Films on FTO Coated Glass and 3-D Nanospike Structures for Efficient Photoelectrochemical Water Splitting. *ACS Appl. Mater. Interfaces* **2016**, *8* (51), 35315–35322.

(7) Higashi, M.; Domen, K.; Abe, R. Highly Stable Water Splitting on

Oxynitride TaON Photoanode System under Visible Light Irradiation. *J. Am. Chem. Soc.* **2012**, *134* (16), 6968–6971.

(8) Chen, H. M.; Chen, C. K.; Chang, Y.-C.; Tsai, C.-W.; Liu, R.-S.; Hu, S.-F.; Chang, W.-S.; Chen, K.-H. Quantum Dot Monolayer-Sensitized ZnO Nanowire-Array Photoelectrodes: True Efficiency for Water Splitting. *Angew. Chemie Int. Ed.* **2010**, No. 122, 6102–6105.

(9) Dabirian, A.; Van De Krol, R. High-Temperature Ammonolysis of Thin Film Ta2O5 Photoanodes: Evolution of Structural, Optical, and Photoelectrochemical Properties. *Chem. Mater.* **2015**, *27* (3), 708–715.

(10) Kato, H.; Kudo, A. Water Splitting into H2 and O2 on Alkali Tantalate Photocatalysts ATaO3 (A = Li, Na, and K). *J. Phys. Chem. B* **2001**, *105* (19), 4285–4292.

(11) Nurlaela, E.; Ziani, A.; Takanabe, K. Tantalum Nitride for Photocatalytic Water Splitting: Concept and Applications. *Mater. Renew. Sustain. Energy* **2016**, *5* (4), 18.

(12) Abe, R.; Higashi, M.; Domen, K. Facile Fabrication of an Efficient Oxynitride TaON Photoanode for Overall Water Splitting into H2 and O2 under Visible Light Irradiation. *J. Am. Chem. Soc.* **2010**, *132* (34), 11828–11829.

(13) Pourroy, G.; Malats, A.; Riera, I.; Poix, P.; Poinsot, R. Low Temperature Syntheses of NbFeO4 and TaFeO4: Influence of Recrystallization on the Magnetic Properties. *J. Solid State Chem.* **1990**, *88* (2), 476–484.

(14) Pourroy, G.; Poix, P.; Marin, S. Phase Transition Orthorhombic Rutile in Solid Solutions between TaFeO4 or TaVO4 and MnF2. *J. Solid State Chem.* **1989**, *81* (1), 121–120.

(15) Lopez, R.; Gomez, R. Band-Gap Energy Estimation from Diffuse Reflectance Measurements on Sol-Gel and Commercial TiO 2: A Comparative Study. *J. Sol-Gel Sci. Technol.* **2012**, *61* (1), 1–7.

(16) Zhang, P.; Zhang, J.; Gong, J. Tantalum-Based Semiconductors for Solar Water Splitting. *Chem. Soc. Rev.* **2014**, *43*, 4395–4422.

(17) Luo, J.; Steier, L.; Son, M. K.; Schreier, M.; Mayer, M. T.; Gratzel, M. Cu2O Nanowire Photocathodes for Efficient and Durable Solar Water Splitting. *Nano Lett.* **2016**, *16* (3), 1848–1857.

Chapter 7: Conclusion and Future Work

7.1 Conclusion

The work outlined in this thesis has covered a detailed study on the design and fabrication of nanomaterials for solar energy conversion into hydrogen. The main contribution of this work is the fabrication of new materials in a simple way for the production of hydrogen from solar water splitting application.

A comprehensive literature review on various materials used in the photoelectrochemical water splitting reaction was done. The principles of water splitting and the general approaches to water splitting was also investigated. This enabled us to understand the requirements of a new material for efficient solar water splitting. The material needs to satisfy three conditions for high efficiency solar water splitting: (i) it must have appropriate band edges, (ii) appropriate band gap and (iii) and have high chemical stability. In addition, the material needs to be environmentally friendly as to not harm the environment.

P-type $LaFeO_3$ photocathode was fabricated by a novel and inexpensive spray pyrolysis technique giving a coral like nanostructured thin film. This yielded a current density of 0.16 mA cm^{-2} at 0.26 V vs RHE. The material showed to be very stable in an alkaline electrolyte solution (pH 13) where it provided a stable p-type response over 21 hours. The optical and impedance data showed that it has a band gap of 2.4 eV with valance band at 1.29 V and a conduction band at -1.11 V. Furthermore, $LaFeO_3$ yielded 0.18 μmol cm^{-2} of hydrogen over a six hour period under constant illumination without any external bias. These findings demonstrate that $LaFeO_3$ is a potential candidate to act as a photoelectrode for unassisted PEC water splitting to generate hydrogen cost effectively

$LaFeO_3$-Ag was successfully synthesised by incorporating silver nanoparticles into the $LaFeO_3$ films by simple spin coating method. The optimised $LaFeO_3$-Ag (0.19 mmol) photocathode generated more than double the amount of hydrogen compared to untreated $LaFeO_3$ in a 6 hour period under constant illumination with no external bias being applied. Moreover, the $LaFeO_3$-Ag electrodes were able to generate hydrogen after one hour of illumination compared to untreated $LaFeO_3$, which required three hours to produce measureable hydrogen. This is because the $LaFeO_3$-Ag semiconductor material is able to absorb more light due to the plasmonic resonance from Ag. This led to the increased hydrogen generation.

$LaFeO_3$-Ni was successfully synthesised by incorporating low-cost nickel nanoparticles into the $LaFeO_3$ films by simple spin coating method. The optimised $LaFeO_3$-Ni (2.84 mmol) generated more than double the amount of hydrogen compared to untreated $LaFeO_3$. Moreover, the $LaFeO_3$-Ni photocathodes were able to generate hydrogen after 2 hours of reaction under constant illumination without any external bias being applied. Whereas the untreated $LaFeO_3$ photocathode began generating hydrogen unassisted after 3 hours. This is because the $LaFeO_3$-Ni semiconductor material was able to absorb more light due to plasmonic resonance from Ni, in the same manner as Ag (though its resonance effect is weaker than Ag). This led to the increased hydrogen generation.

$TaFeO_4$ photocatalytic powder was successfully synthesised using sol-gel method. To achieve a single phase form of $TaFeO_4$ it was found that a high reaction temperature of 1100°C is required. The photocatalyst was subjected to water splitting test to see if any hydrogen is produced. It showed that at 7 hours of constant illumination it began to generate hydrogen though the amount is very little. Attempts were made to try and fabricate an electrode form of $TaFeO_4$, however this proved to be very difficult and was not successful.

7.2 Future Work

To the best of my knowledge, the spontaneous hydrogen production of $LaFeO_3$, $LaFeO_3$-Ag and $LaFeO_3$-Ni (without any external bias) has been shown for the first time. This shows that $LaFeO_3$ is a promising candidate for future water splitting technologies for solar hydrogen production. However, further work is require to increase the materials efficiency.

Future work on $LaFeO_3$ photocathode should be on the understanding and improving the efficiency of $LaFeO_3$. Different morphological structure such as nanotube or nanowires could be one such was for improving its efficiency, as well as doping with various other metals and cocatalysts. Furthermore, whilst conducting the hydrogen evolution measurement the gas bubbles on the film surface reduces the photocurrent due to shading effect. This can be eliminated by having the reaction vessel under agitation to remove the bubbles from the film surface, allowing full surface area for the reaction.

$TaFeO_4$ has the potential to generate hydrogen from solar water splitting. However, ways to create an electrode form of the material should be the focus for $TaFeO_4$ fabrication. A potential method for synthesising $TaFeO_4$ can be by using microwave assisted annealing. This could help overcome the high fabrication temperatures of 1100^oC required for synthesising $TaFeO_4$, by synthesising the $TaFeO_4$ phase at a much lower temperature. An electrode form will allow us to determine its electrical properties and weather it is a p-type or n-type material. Also, it will allow us to easily determine the materials band structure through electrochemical impedance spectroscopy.

Appendix 1: Publication 1

Unbiased Spontaneous Solar Fuel Production using Stable $LaFeO_3$ Photoelectrode

DOI:10.1038/s41598-018-21821-z

Appendix 2: Publication 2

Enhanced Photoactivity and Hydrogen Generation of $LaFeO_3$ Photocathode by Plasmonic Silver Nanoparticle Incorporation

https://doi.org/10.1021/acsaem.8b00628

Appendix 3: Publication 3

Plasmonic nickel nanoparticles decorated on to $LaFeO_3$ photocathode for enhanced solar hydrogen generation

https://doi.org/10.1016/j.ijhydene.2018.10.240

Appendix 4: Publication 4

Porous ZnO/Carbon nanocomposites derived from metal organic frameworks for highly efficient photocatalytic applications - A correlational study

https://doi.org/10.1016/j.carbon.2019.02.013